DOTTORATO DI RICERCA IN
FISICA

CICLO XXXII

COORDINATRICE Prof. Luppi Eleonora

Fabrication of crystals for investigation of orientational effects in high energy physics

Settore Scientifico Disciplinare FIS/01

Dottorando
Dott. Romagnoni Marco

Tutore
Prof. Guidi Vincenzo

Anni 2016-2019

Contents

List of publications

The work presented in this thesis is based on the following articles and conference proceedings:

A1: R. Camattari, G. Paternò, M. Romagnoni, V. Bellucci, A. Mazzolari and V. Guidi, J. Appl. Cryst. **50** (2017) 042903, *Homogeneous self-standing curved monocrystals, obtained using sandblasting, to be used as manipulators of hard X-rays and charged particle beams*

A2: G. Germogli, A. Mazzolari, V. Guidi, M. Romagnoni, Nucl. Instr. Meth. B **402** (2017), *Bent silicon strip crystals for high-energy charged particle beam collimation*

A3: Bandiera, L., Tikhomirov, V.V., Romagnoni, M., Argiolas, N., Bagli, E., Ballerini, G., Berra, A., Brizzolari, C., Camattari, R., De Salvador, D., Haurylavets, V., Mascagna, V., Mazzolari, A., Prest, M., Soldani, M., Sytov, A., Vallazza, E., Phys. Rev. Lett. **121** (2018), *Strong Reduction of the Effective Radiation Length in an Axially Oriented Scintillator Crystal*

A4: Mazzolari, A., Romagnoni, M., Camattari, R., Bagli, E., Bandiera, L., Germogli, G., Guidi, V., Cavoto, G., Eur. Phys. J. C **78** (2018), *Bent crystals for efficient beam steering of multi TeV-particle beams*

Articles and proceeding not included in this thesis published during the PhD:

N1: Sytov, A.I., Bandiera, L., De Salvador, D., Mazzolari, A., Bagli, E., Berra, A., Carturan, S., Durighello, C., Germogli, G., Guidi, V., Klag, P., Lauth, W., Maggioni, G., Prest, M., Romagnoni, M., Tikhomirov, V.V., Vallazza, E., The European Physical Journal C **77** (2017), *Steering of Sub-GeV electrons by ultrashort Si and Ge bent crystals*

N2: W. Scandale *et al*, Nucl. Instr. Meth. B **414** (2018), *Focusing of a particle beam by a crystal device with a short focal length*

N3: W. Scandale *et al*, Physical Review Accelerators and Beams **21** (2018), *Comprehensive study of beam focusing by crystal devices*

N4: Salvador, D.D., Carturan, S., Mazzolari, A., Bagli, E., Bandiera, L., Durighello, C., Germogli, G., Guidi, V., Klag, P., Lauth, W., Maggioni, G., Romagnoni, M., Sytov, A., Journal of Instrumentation **13** (2018), *Innovative remotely-controlled bending device for thin silicon and germanium crystals*

N5: Sytov, A.I., Guidi, V., Tikhomirov, V.V., Bandiera, L., Bagli, E., Germogli, G., Mazzolari, A., Romagnoni, M., Journal of Instrumentation **13** (2018), *A method to align a bent crystal for channeling experiments by using quasichanneling oscillations*

N6: Camattari, R., Romagnoni, M., Mazzolari, A., Paternò, G., Guidi, V., Buslaps, T. Experimental Astronomy **46** (2018), *Thick self-standing bent crystals as optical elements for a Laue lens for applications in astrophysics*

N7: W. Scandale *et al*,Nucl. Instr. Meth. B **438** (2019), *Dechanneling of high energy particles in a long bent crystal*

N8: Camattari, R., Bandiera, L., Tikhomirov, V., Romagnoni, M., Bagli, E., Germogli, G., Sytov, A., Maiolino, T., Tamisari, M., Mazzolari, A., Guidi, V., Cavoto, G.,Physical Review Accelerators and Beams **22** (2019), *Silicon crystalline undulator prototypes: Manufacturing and X-ray characterization*

N9: W. Scandale *et al*,Nucl. Instr. Meth. B **446** (2019), *Focusing of 180 GeV/c pions from a point-like source into a parallel beam by a bent silicon crystal*

N10: W. Scandale *et al*,Eur. Phys. J. C **79** (2019), *Beam steering performance of bent silicon crystals irradiated with high-intensity and high-energy protons*

Chapter 1

Introduction

Interaction of a particle beam in a solid is dominated by stochastic behaviour: trajectories are not deterministic but are result of random scattering with atoms of the medium. Nevertheless, contrary to amorphous materials, single crystals feature a precise and ordered atomic nanostructure replicating up to macroscopic size. Especially along main crystallographic direction, atoms are placed not into the irregular scheme like amorphous but built planes and axes. Thus, interaction of impinging particles is better understood with a *continuous potential*. Such potential is characterized by extremely intense fields, heavily influencing charged particles trajectories into behaviour otherwise unattainable. A plethora of orientational coherent phenomena exists, which leads to novel approaches for high energy physics experiments. *Channeling* is the principal effect investigated in this thesis. Particle intercepting crystal lattice structure within a small critic angle are bounded to its planes or axes continuous potential.[1] Positive charged particles in planar channeling are repelled away from atomic nuclei and forced to propagate in oscillatory motion between two adjacent atomic planes, thus experiencing strongly suppressed energy loss while crossing the medium. This interaction between beam and crystal enables the possibility to manipulate the latter by acting on the first. In particular, particles channeled in a bent crystal follow its curvature. The steering power of the technique largely overcome electromagnetic optics: a few mm long bent silicon can as a several hundred Tesla magnetic dipole. This can be exploited to substitute an artificial magnet to deflect beams [2] or to induce spin precession of a particle[3], in a much reduce space and with no energy consumption. In this thesis most of the work is focused on the fabrication of bent crystal suited for steering LHC proton beam for several different applications. The upgrade of the collimation system: substituting amorphous target with a crystal-based system to gently separate the beam halo from the primary beam. The extraction of halo into an extracted beam line for simulation of cosmic ray shower or other fixed target experiments. The precession of spin in strange and charmed baryons in order to investigate electric and magnetic dipole moments. The sample required for these applications requires development of bending techniques with nanometric precision over macroscopic sizes (millimetres and centimetres) and equally sensitive measurement methods to control the production process. Interferometry, x-ray diffraction and autocollimation were combined and pushed to state of art limit in order to achieve such goals. The preparation works carried out mainly in Ferrara was completed with beam test at CERN North Area, on SPS extracted beam lines. In collaboration with CERN UA9 experiment and Crysbeam and SELDOM ERC projects, channeling features of the prototypes were directly investigated with 180 GeV pions beams.

Another type of orientational coherent phenomenon was investigated as well. The internal fields of a crystal grow in intensity as the density and atoms' atomic number increase. In axially aligned heavy inorganic scintillator such as lead tungstate, ultrarelativistic particles such as electrons (and positrons) with momentum $\geq$26 GeV perceive in their rest frame a Lorentz boosted field which overcomes Schwinger critical fields. This condition, reached in nature only in extreme environments such as pulsar atmosphere, enables non-linear QED mechanism and strongly enhance the emission of hard photons. Thus, electromagnetic shower is significantly accelerated, and the material acts with an effective radiation length. Electromagnetic calorimeters exploiting this effect would outperform regular one and allows compact solution for beam dump or airborne experiments. A deep investigation of the crystal quality of the crystalline sample was carried out with x-ray diffraction techniques, both in Ferrara laboratories and external facilities such as ESRF in Grenoble, before the actual experiment with 120 GeV electron (and positron) beam.

In order to produce an auto-consistent work, in the thesis the first chapters are dedicated to the description of physical phenomena exploited in the applications of the crystalline samples. Indeed, many production parameters are directly linked to the features of the coherent phenomena occurring in the crystal. Following chapters will be dedicated to the description of the applications and the relative research carried out in the University of Ferrara Laboratories and external facilities such as CERN and ESRF.

Chapter 2

Coherent interactions of charged particle beams with crystalline media

2.1 Crystal lattice

As the very first x-rays diffraction experiments by Laue and Bragg confirmed the existence of crystal lattice, in 1912 Stark [4] had the first idea that such ordered structure may be relevant for the process of interaction of charged particles with matter as well. Forty year later Ferretti [5], Ter-Mikaelian [6], Dyson and Uberall [7] studied the interference of relativistic electron bremsstrahlung radiation with crystal atomic planes (coherent bremsstrahlung, CB), and anticipated remarkably different features than the case of amorphous target described by the Bethe and Heitler formulation (BH) [8]. Experimental confirmation followed soon thanks to Diambrini-Palazzi et al. at Frascati in 1960 [9]. Finally, in 1963 the channeling effect was discovered in computer simulations [10] and experiments [11], which observed anomalous long penetration depth of positive ion in crystal when trajectory was closely aligned with crystallographic axes.

In 1964 Lindhard [1] developed the theoretical bases of the phenomenon, introducing the concept of continuous potential. Indeed, particles impinging into a lattice at low angle with its planes or axes undergo a series of correlated small scattering events with atoms. Thus, analytical calculation of the total effect can be carried out by summing each single scattering, obtaining for positive charged particles a potential well with maxima on planes/axes and minimum between them (whereas the opposite take place for negative charged ones). Channeling consists in the trapping of a charged particle within the planar/axial potential well.

Early investigations on channeling focused on low energy particles (1÷100 KeV), and still nowadays great deal of studies in solid state physics exploits the phenomenon. The idea of exploit channeling for ultrarelativistic beam manipulation was first proposed by Tsyganov in 1976 [12]. The basic principle being that in a bent crystal, particles bound by channeling to plane or axes would be induced to follow the curvature. The first experimental attempt to exploit channeling in bent crystal was to extract a circulating beam from an accelerator by means of a bent crystal was performed at Dubna Synchrophasotron [13], where an 11 mm long crystal operating in parasitic mode diverted a 8.4 GeV proton beam at an angle of 35 mrad with an efficiency of $\sim 10^{-4}$. Later, an intensive experimental campaign was carried out at U-70 (IHEP, Protvino, Moscow), where 50 and 70 GeV proton beams [14, 15] were extracted with an efficiency of about 1%. The low extraction efficiencies were ascribed to sub-optimal geometries of the crystals [16] or to a non-optimized experiment set-up [13]. Although the obtained results showed low efficiency, they demonstrated for the first time the channeling phenomenon. Afterwards, an experimental campaign was started in the late 1990s at CERN (proton beams of energies of 14, 120 and 270 GeV [17–19]) and Tevatron (proton beam of energy 900 GeV [20, 21]). Extraction efficiencies increased ($\sim$10% and $\sim$25% respectively), but still remained at values consistently lower than the ones reached with slow extraction approaches ($\sim$98%). Such low values were ascribed to the presence of an imperfect layer on the crystal surface [18, 22, 23], unwanted parasitic effects in the deformation of the crystal [17, 23], and to an inappropriate choice of the length of the crystal [22, 24–26]. In particular, simulations demonstrated [22, 23] that the length of the crystals used at SPS and Tevatron (30 and 40 mm respectively) was optimized for operations in single-pass mode, not in multi-pass. As a result, crystals about 5 times shorter would have provided extraction efficiencies about 3 times higher. Moreover, recent simulations predict the possibility to reach an efficiency of 99% for 270 GeV proton extraction from the SPS [27]. Simulation models proved to be invaluable tools in the design of crystalline deflectors and drove the design and manufacturing of a subsequent generation of crystals [28] and bending schemes [29, 30]. This progress resulted in a considerable increase of extraction efficiency, which reached the value of 85% [29]. Further developments, carried out in the last 20 years in crystal manufacturing and characterization, allowed to manufacture crystals free from lattice damage, surface roughness lower than 0.1 nm, and miscut angle (i.e. *reference plane deviation* in SEMI notation[31]) lower than 5 μrad, satisfying the requirements to aim at the collimation or the extraction of the LHC circulating beam. Driven by those results, an intense experimental campaign [32] investigating the possibility to collimate or extract the proton beam circulating in the LHC was started in the late 1990 at H8 and H4 extracted lines of the SPS. New coherent interaction effects of ultra-relativistic proton beams with crystals were observed, among which were the phenomena of volume reflection [33, 34], beam steering by means of crystal axes [35–37], multiple volume reflection [38–41] and mirroring [42]. For the first time, efficient beam steering was also recorded for both positively [43–45] and negatively charged particle beams [46, 47]. The success of this campaign led to the use of the SPS as a platform for developing the technology needed to attempt the collimation of the LHC circulating beam [38, 48, 49]. Successively, two bent crystals were installed in the LHC [50], where coherent interactions even at 6.5 TeV were observed [51]. This result opened the possibility to achieve crystal-assisted collimation of the LHC circulating beam. Two more crystal were installed in 2017 and a total of 92h of Machine Development from 2015 until long shutdown 2 in 2018 were dedicated to study and refine crystal use in LHC. Crystal collimation was tested for both protons and ion beam during injection, energy ramp up and flat top operation. Positive results led to a first employment of crystal collimation not in dedicated test but assisting experiments during collisions. LHC high luminosity upgrade consider employment of crystal for ion beam collimation. Further studies were developed investigating new exploitation of bent crystal in LHC machine. In 2014 Crysbeam ERC project proposed the employment of a long bent crystal to steer beam halo into an external beamline for fixed target experiments. Afterwards other suggestions were made based on the separation of beam halo from primary beam and its consequent use in a dedicated experiment, but exploiting existing detector inside LHC and thus avoiding extraction to an external line [52, 53]. Recently interest in study of magnetic dipole moment (MDM) and electric dipole moment (EDM) by use of planar channeling in bent crystal has been reignited. As early proposed by Baryshevsky back in 1979[3] and experimentally observed at Fermilab in 1992 [54], spin precession takes place for channeled particles travelling along bent planes. Such effect could be the unique tool currently available for investigation of MDM and EDM in extremely short-lived particles such as charmed baryons. Λ_c^+ and Ξ_c^+ even when boosted at TeV momentum can only travel few cm before decaying. Indeed, to efficiently induce precession of these quantities in such compact manner a bent crystal is the only feasible solution (an artificial magnetic dipole would require magnetic field ¿ 10^3 Tesla). In SELDOM ERC project, an 80 mm silicon (or 50 mm germanium) bent crystal imposes a 16 mrad deflection on charmed baryons produced in a tungsten target by proton extracted upstream from beam halo using another bent crystal. In this chapter, a brief description of coherent interactions in straight and bent crystals is presented. Although a plethora of phenomena correlated to coherent orientational effects in flat and bent crystal, focus is pointed to channeling and axial strong field as they are mainly exploited during this work.

2.2 Channeling and related phenomena in straight crystals

2.2.1 Directional effects

An amorphous material is characterized by homogeneity and isotropy, much like in a gas medium a charged particle would undergo series of random and uncorrelated scattering events with each atom. Energy loss and trajectory changes are statistical results deriving from the total sum of such interactions. A single crystal instead is made of a continuous repetition of the same precise arrangement of atoms (unit cell), neighbour atoms positions are precisely defined and replicated over the total volume of the solid. This lattice structure appears different wrt the point of observation, along specific orientations in particular, atoms are aligned in string and planes. Incoming charged particles impinging at large angle wrt such direction undergo larger deflection in each scattering event and quickly loose the original trajectory (governed motion). But, when a particle impacts the medium at small angle wrt lattice planes/ axes, one atom induce only small perturbation on the trajectory (ungoverned motion). In 1964-5 Lindhart addressed the issue [1] and calculated how subsequent interaction with single atomic potential are correlated, an effective physics description would thus consider the whole lattice interact with the projectile particles. Indeed, a continuous potential was calculated summing the single atomic potential of each orderly placed atoms on the planes.

In the next sections, the concepts of continuous potential and of channeling are described following the book [16]. Most attention is given to planar effects, since they are the most investigated within this work of thesis.

2.2.2 Planar motion of charged particles in a straight crystal

Continuous Planar Potential

When the motion of a charged particle is aligned (or nearly aligned) with a string (or plane), subsequent perturbations of trajectory caused by single atoms may coherently built up, leading to a collective effect on particle motion. Indeed, in such *low-angle approximation* one can replace the potentials of single atoms with an averaged **continuous potential** supported by the whole lattice planes (or axes). As atoms position in lattice is well defined, thus it is possible to calculate a one-dimension potential by integrating single atom-particle potentials V over the planes:

$$U_{pl}(x) = N d_p \int_{-\infty}^{\infty} \int_{-\infty}^{\infty} V(x, y, z)\, dy\, dz \tag{2.1}$$

N being the density of atoms and d_p the interplanar spacing. Fig. 2.1(a) shows a scheme for a positive particle interacting with a crystal plane composed by individual atoms. Given the

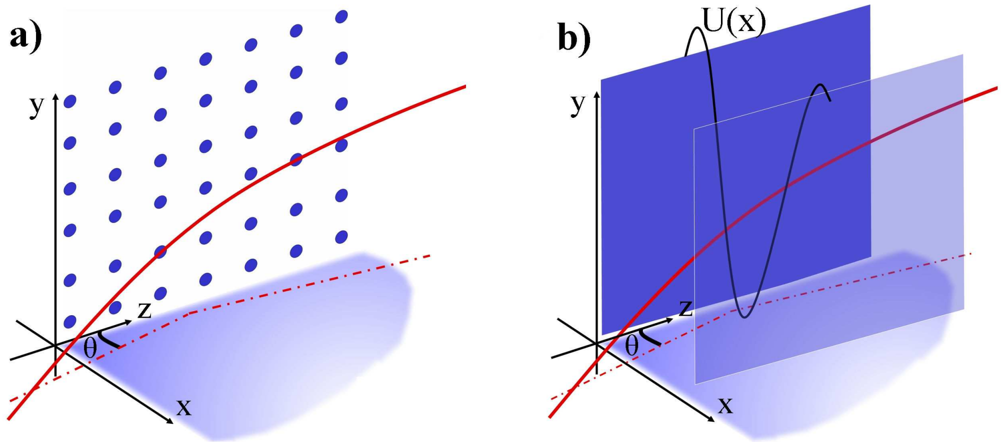

Figure 2.1: a) A positive particle moving in a crystal misaligned with respect to the axis but nearly aligned wrt crystallographic plane. b) particle feeling an averaged planar continuous potential ($U(x)$): a potential well between two neighbouring crystal planes [55].

distance between particle and atom $r = \sqrt{x^2 + y^2 + z^2}$, if it is not too much larger than a_{TF} (the screening length of the particle-atom interaction), the potential $V(r)$ is Thomas-Fermi-like, hence it can be described by the nucleus point-charge coulomb potential modulated by Fermi screening function $\Phi\left(\frac{r}{a_{TF}}\right)$ taking into account the electronic distribution around the nucleus:

$$V(r) = \frac{Z_i Z e^2}{r} \Phi\left(\frac{r}{a_{TF}}\right), \tag{2.2}$$

$Z_i e$ being the particle charge and Z the atomic number of the crystalline medium. Here, the screening distance is $a_{TF} \approx 0.8853 a_B Z^{-\frac{1}{3}}$ and the Bohr radius is $a_B = 0.529$ Å. Lindhart in his work defined the screening function as:

$$\Phi\left(\frac{r}{a_{TF}}\right) = 1 - \left(1 + \frac{3{a_{TF}}^2}{r^2}\right)^{-\frac{1}{2}}, \tag{2.3}$$

the integration of such potential over the lattice plane leads to the following result:

$$U_{pl}(x) = 2\pi N d_p Z_i Z e^2(\sqrt{x^2 + 3a_{TF}{}^2} - x). \tag{2.4}$$

A more accurate approach is given by Doyle and Turner [56], where the potential $V(r)$ is obtained by fitting the electron scattering factor, determined by a Hartree-Fock calculation, to experimental results. The Doyle-Turner potential has the form

$$V(r) = 16\pi Z_i a_B e^2 \sum_{i=1}^{4} \frac{a_i}{(b_i/\pi)^{3/2}} exp\Big[\frac{-r^2}{(b_i/4\pi)^2}\Big], \tag{2.5}$$

where a_i and b_i are tabulated coefficients [56]. The planar static continuum potential according to Doyle-Turner is:

$$U_{pl}(x) = 2\pi^{1/2} N d_p Z_i a_B e^2 \sum_{i=1}^{4} \frac{a_i}{(b_i/4\pi^2)^{1/2}} exp\Big[\frac{-x^2}{(b_i/4\pi^2)^2}\Big], \tag{2.6}$$

Another common approximation for the Fermi function Φ was given by Moliére [57], leading to a different approximation for planar potential:

$$U_{pl}(x) = 2\pi N d_p Z_i Z e^2 a_{TF} \sum_{i=1}^{3} \frac{\alpha_i}{\beta_i} exp\Big(-\frac{\beta_i x}{a_T F}\Big), \tag{2.7}$$

being $\alpha = (0.1, 0.55, 0.35)$ and $\beta = (6.0, 1.2, 0.3)$ the Moliére's coefficients.

An important factor to consider is the temperature effect as well. Since atoms modify their position through thermal vibration, the real potential is affected as well, especially near the lattice planes. In order to properly address the issue, position of each nuclei should be defined as a Gaussian probability distribution centred on each site, with deviation correspondent to the root-mean square amplitude, u_T[1]

$$P(x) = \frac{1}{\sqrt{2\pi u_T^2}} exp\left(-\frac{x^2}{2u_T^2}\right), \tag{2.8}$$

the modified potential can be obtained by convoluting $U_{pl}(x)$ over this distribution. As an example, for silicon at room temperature, u_T is about 0.075 Å, which is quite small as compared to the lattice constant d = 5.43 Å. Fig. 2.2 displays the continuous poten-

[1]One should remember that, even if a material is at T = 0 K, its atoms has an irreducible amount of vibrational energy

tial under Moliére approximation with the contribution of thermal vibrations at different temperatures for the case of Si(110) planes.

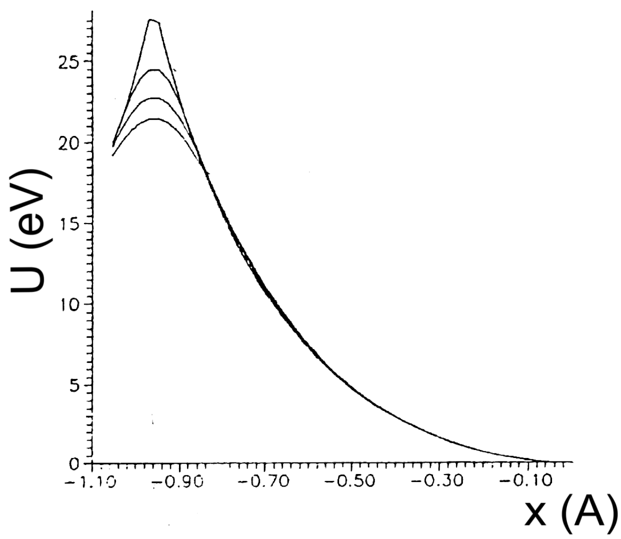

Figure 2.2: The Moliére potential of the Si(110) planes at different temperatures, and the potential of the static lattice. Top to bottom at the left edge: static, $77K$, $300K$, $500K$ [16].

The main contribution to interplanar particle motion in the lattice is caused by the two nearest planes, thus the total potential can be approximated as

$$U_{pl}(x) \approx U_{pl}(d_p/2 - x) + U_{pl}(d_p/2 + x) - 2U_{pl}(d_p/2), \tag{2.9}$$

x being the transverse coordinate, with origin defined at the minimum of the potential $U(0) = 0$. As a result, a positive particle moving in a crystal nearly aligned with crystal planes *sees* the crystal as a series of potential wells, U(x), formed between neighboring planes (see Fig. 2.1(b)).

Most employed material for channeling experiment with high-energy particle are Diamond, Silicon and Germanium. All with the same type of diamond-like fcc crystal lattice (see Fig. 2.3-left), they are the only three single crystals that can be growth to large sizes ($> 10^2 mm^3$) with almost perfect lattice structure. In some cases, since higher Z materials generate a stronger potential, W crystals while of worst quality are still an appealing alternative.Fig. 2.3-right shows the main planes of the cubic lattice, indicated by the Miller indexes. Each plane has a different inter-atomic distance, d_p. Table 2.1 summarizes the parameters of the strongest planar channels of the crystal of silicon at room temperature. Higher Miller indexes correspond to weaker crystal planes.

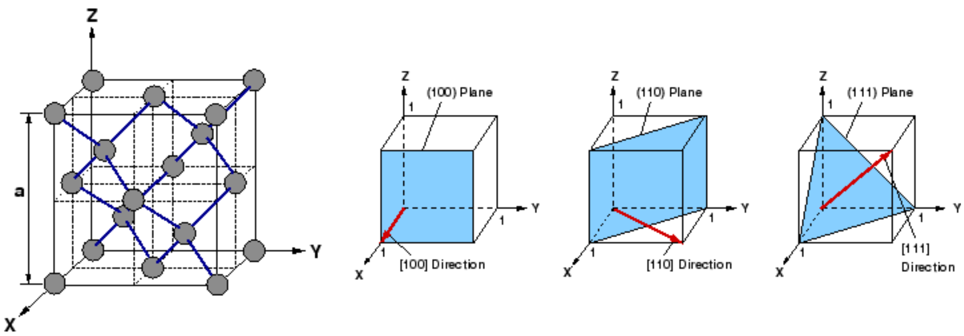

Figure 2.3: Left-The diamond cubic lattice is characterized by a tetragonal covalent bond: two identical fcc lattices, one inside the other and shifted along the bulk diagonal by one quarter of their length. Right-The main planes of the cubic lattice, i.e., (100), (110) and (111).

Plane	d_p [Å]	a_{TF} [Å]	u_T [Å]	$U(x_c)$ [eV]	$U'(x_c)$ [GeV/cm]
Si		0.194	0.075		
(110)	1.92			16	5.7
(111)L	2.35			19	5.6
(111)S	0.78			4.2	3.5

Table 2.1: Parameters of some planar channels of silicon crystal. The potentials U are given at the distance $x_c = d_p/2 - 2u_T$ in the Moliére approximation [16].

Fig. 2.4 displays some examples of the interplanar potential energy of positively charged particles interacting with the (110) and (111) planes, which are the most commonly used for *channeling experiments*, due to the generation of the largest potentials. The harmonic approximation $U \sim x^2$, plotted with a dashed line in Fig. 2.4(a), fits the interplanar Moliére potential rather well, and it is often used for analytic estimations. The planar potential-well depth in silicon is $\sim$ 20 eV.

Fig. 2.5 shows the scheme of continuous planar potential for either positive (a) or negative (b) particles in the case of a silicon crystal oriented along the (110) planes. The harmonic approximation does not hold for the planar potential for negatively charged particles, being opposite to that for positive particles and thus more similar to an "inverted parabola" [58].

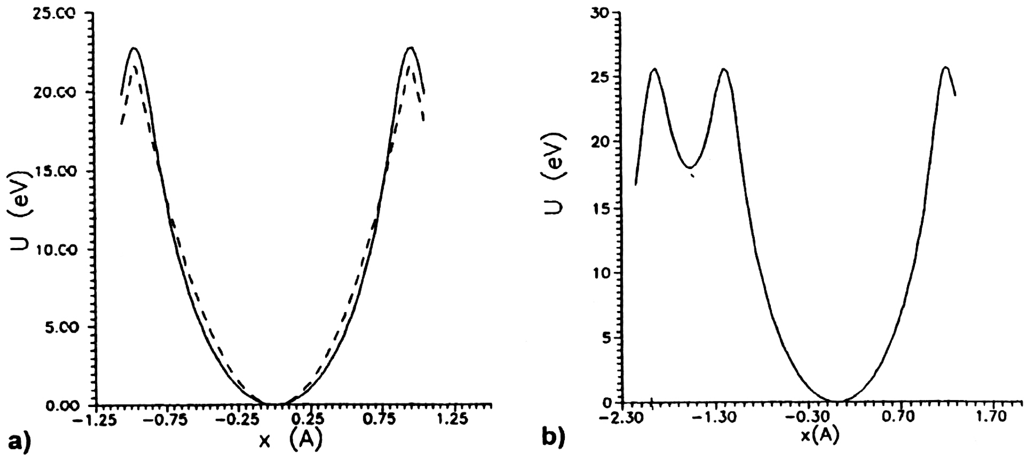

Figure 2.4: The interplanar Moliére potential for (a) the Si channels (110) and (b) the Si channels (111) for positively charged particles with Z_i=1 (solid lines). The dashed line represents the harmonic approximation. In the crystal with the (111) orientation the large distance ${d_p}^L = 2.35$ Åbetween the atomic planes changes periodically into a small one ${d_p}^S = 0.78$ Å[16].

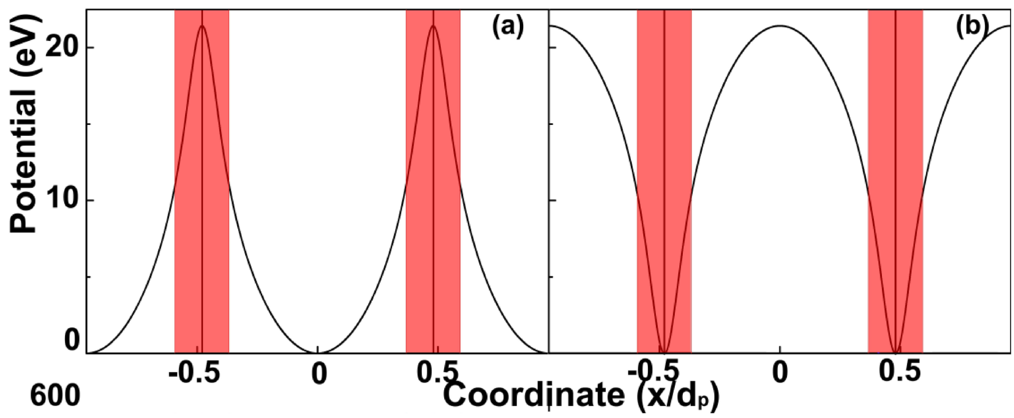

Figure 2.5: Planar potentials experienced by positive (a) and negative (b) particles channeled in the field of (110) silicon planes. Shaded regions highlight the regions of high nuclear density (nuclear corridors), vertical lines inside those regions show the positions of atomic planes [47].

Planar Channeling

Transverse motion of a particle travelling in a crystal at low angle wrt lattice plane is subjected to a continuous potential. When transverse motion of the particles is insufficient to cross such potential well, the trajectory is bounded between two neighbour planes in a channeled state. This process is schematically shown in Fig. 2.6.

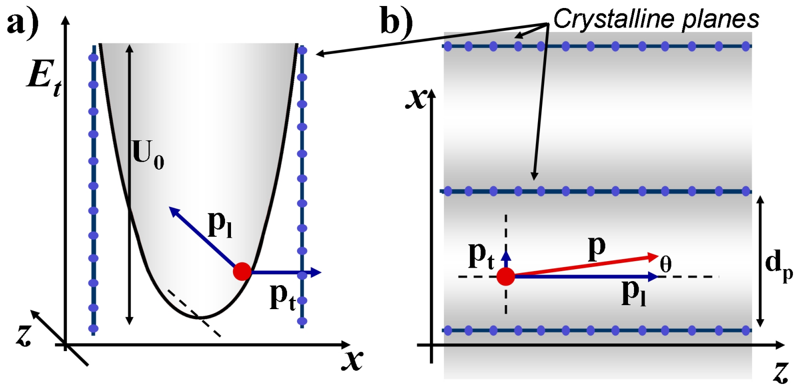

Figure 2.6: a)A positive particle bound in the interplanar continuous potential. b)Top view of the channel. Here are highlighted the components of the transverse (p_t) and longitudinal (p_l) momentum of the particle with respect to the plane direction. $\theta = p_t/p_l$ is the small misalignment angle with respect to the crystal plane. Adapted from [59]

Planar channeling is characterized by remarkably different features from motion in an amorphous medium or misaligned crystal [16]. Inside a solid medium, energy loss by a charged particle is mainly derived by two sources: electronic and nuclear stopping. The first being caused by the inelastic collisions with atomic electrons, the latter being related to scattering with nuclei. As nuclei are much more massive than electrons, far more momentum and energy is transferred per event. A single nuclear collision, ignoring spin effects and screening, behaves following the well-known Rutherford formula where $\frac{d\sigma}{d\Omega} \propto 1/\sin^4(\theta/2)$, hence small angular deflection are favoured wrt larger ones. Particle undergoes numerous scattering building a random total modification of its trajectory. At relativistic energies, electronic stopping is completely dominating, being nuclear stopping $\sim 10^3$ times smaller. A quantum perturbation treatment of the excitation of the atomic system may then be applied (Bethe-Bloch treatment) [1]. For light particles, such as electrons and positrons, the radiative losses become dominant in the energy loss spectrum at relativistic velocities [60].

Channeled particles, depending on electric charge, are subjected to either enhancement or suppression of energy losses. Positive particles are confined by continuous potential far from atoms on lattice plane and thus scarcely interacts with nuclei. Even electronic collisions are much lower as larger electronic density is near atoms. This of course leads to a significantly reduced energy loss: positive charged particles cross much larger distances than in an amorphous medium. The opposite occurs for negatively charged particles as potential drives them near planes, increasing probability of nuclear and electronic energy loss. Radiative losses instead are larger in both cases, as new emissions phenomena are induced by the oscillatory motion of the particle inside the channel (channeling radiation). This affects mainly light particles such as electrons and positrons.

While single scattering event between particle and atom are of quantum nature, channeling motion may be considered of classical mechanics for large momentum. In analogy with the quantum harmonic oscillator, such approximation increases effectiveness as energetic levels grow in the potential well. The quasiclassical estimate of the number of levels in the one-dimensional potential well at planar channeling yields $N \sim \frac{d_p}{\lambda_c}\sqrt{\frac{EU_0}{m^2}} \gg 1$, λ_c being the Compton wavelength, E the particle energy, U_0 the potential well depth and m the particle mass. The second condition is always fulfilled for heavy particles, such as ions and protons, but for light particles (electrons, positrons) the classical approach starts to work in the $10 - 100 MeV$ energy range [58].

The classical principle of energy conservation can thus be extended to channeling motion transversal energy (see eq. 2.1). When the transverse component p_x of the particle momentum p is much smaller than the longitudinal component p_z (*i.e.* $\theta \approx tg\theta = p_x/p_z \ll 1$), the total conserved energy E of the system can be written in the form:

$$E = \sqrt{{p_x}^2c^2 + {p_z}^2c^2 + m^2c^4} + U(x) \simeq \frac{{p_x}^2c^2}{2E_z} + E_z + U(x) = const, \tag{2.10}$$

being $E_z = \sqrt{{p_z}^2c^2 + m^2c^4}$ a conserved quantity, since the potential energy $U(x)$ is independent of z. As a consequence, the transverse energy, $E_T = \frac{{p_x}^2c^2}{2E_z} + U(x)$, must be conserved too. Being $p_x \simeq p_z\theta$ and assuming $E_z \approx E$, $p_z \approx p$, using the known relation $pc^2 = vE$, where v is the particle velocity, we may rewrite E_T as:

$$E_T = \frac{pv}{2}\theta^2 + U(x) = const. \tag{2.11}$$

The particle trajectory is obtained by the integration of

$$dz = \frac{dx}{\sqrt{2/pv[E_T - U(x)]}}. \tag{2.12}$$

Rewriting eq. 2.11 by taking into account that $\theta = dx/dz$ one obtain

$$E_T = \frac{pv}{2}\left(\frac{dx}{dz}\right)^2 + U(x) = const \tag{2.13}$$

Differentiating with respect to z and dividing all terms by θ, the result for the one-dimensional transverse motion in the potential $U(x)$ is:

$$pv\frac{d^2x}{dz^2} + \frac{d}{dx}U(x) = 0 \tag{2.14}$$

Eq. 2.14 describes the particle transverse oscillation of the particle motion under the influence of the planar potential U(x).

In the case of positively charged particle, in Sec. 2.2.2 it has been shown that the harmonic approximation $U(x) \simeq U_0\left(\frac{2x}{d_p}\right)^2$ for the interplanar potential can be used for qualitative general studies (while for precise calculation simulation would be needed). In this case the solution of eq. 2.14 is a sinusoidal oscillation:

$$x = \frac{d_p}{2}\sqrt{\frac{E_T}{U_0}}\sin\left(\frac{2\pi z}{\lambda} + \phi\right) \tag{2.15}$$

with the oscillation period being $\lambda = \pi d_p\sqrt{pv/2U_0}$.

In the case of negatively charged particles, the harmonic approximation for $U(x)$ never holds, therefore a single period cannot be defined. Nevertheless, the main features of the electron motion at planar channeling can be easily observed by means of the simple model of "inverted parabola potential" [58]:

$$U(x) \simeq U_0\left[1 - \left(1 - \frac{2|x|}{d_p}\right)^2\right]. \tag{2.16}$$

Within this simplified model the period of each channeled particle depends on its transverse energy inside the potential well, E_T, being $\lambda = d_p\sqrt{pv/2U_0}ln|\frac{1+\sqrt{E_T/U_0}}{1-\sqrt{E_T/U_0}}|$.

The particle remains trapped within the channel if its transverse energy is lower than the potential-well depth U_0 (defined at the distance $d_p/2$ from the center of the potential well:

$$E_T = \frac{pv}{2}\theta^2 + U(x) \leq U_0. \tag{2.17}$$

This equation clearly shows how transversal energy increase as misalignment with lattice grows. As previously stated channeling can occur only when E_T is smaller than the potential depth, thus the maximum impinging angle for a particle moves along the center line of a channel ($x = 0$, $U(0) = 0$), with oscillations around the center of the channel, can be calculated from eq. 2.17:

$$\theta_c = \sqrt{\frac{2U_0}{pv}}, \tag{2.18}$$

θ_c being the critical angle introduced by Lindhard, for both planar and axial channeling independently of the particle electric charge sign.

Dechanneling

The motion of channeled particles is affected by incoherent scattering with electrons and nuclei, which causes the non-conservation of the transverse energy E_T due to the contribution of a random scattering angle in a event of scattering. As a result E_T may become higher than the potential barrier, thus escaping bound state from the channel (*dechanneling* process) [16, 47]. There are two main sources of dechanneling in crystals: the multiple quasi-elastic scattering with nuclei and the multiple inelastic scattering with electrons.

In a regular medium, the electronic scattering is usually neglected in many physical approximation and the incoherent scattering with nuclei can be well described by a multiple Coulomb scattering[2] (MCS) process. MCS can be roughly represented by a Gaussian for small deflection angles [61], where the value

$$\theta_0 = \theta_{plane}^{rms} = \frac{13.6 MeV}{\beta c p} Z \sqrt{\frac{t}{X_0}} \left[1 + 0.038 \ln \left(\frac{t}{X_0} \right) \right] \tag{2.19}$$

is the width of the approximate Gaussian projected angle distribution, p, βc and Z are the momentum, velocity and charge number of the incident particle, and t/X_0 is the true path length in radiation length unit. A more accurate theory was given by Moliere [62], which takes into account the large scattering angles ($>$ a few θ_0) leading to larger tails that a Gaussian distribution does.

In the case of a crystalline material, it is not always possible to disregard the contribution of multiple scattering with electrons and nuclei scattering needs adjustment as well. For positive planar channeled particles, the two phenomena are addressed separately as electronic and nuclear dechanneling.

Interaction with nuclei leads quickly to variation in E_T and resulting overcome of potential barrier. While for TeV energy such effects may progress across few millimetres and calculation must employ simulation, for lower energy can be correctly assumed that all particle travelling near lattice planes undergo dechanneling. We can approximate the atomic density as a Gaussian distribution with standard deviation equal to the atomic thermal vibration amplitude, u_T, (see eq. 2.8), and then assume that the atomic density region interested by intense multiple scattering extends, for example, over 2.5 u_T, the so-called

[2] We are neglecting the strong interactions that may also contribute to multiple scattering for hadronic projectile.

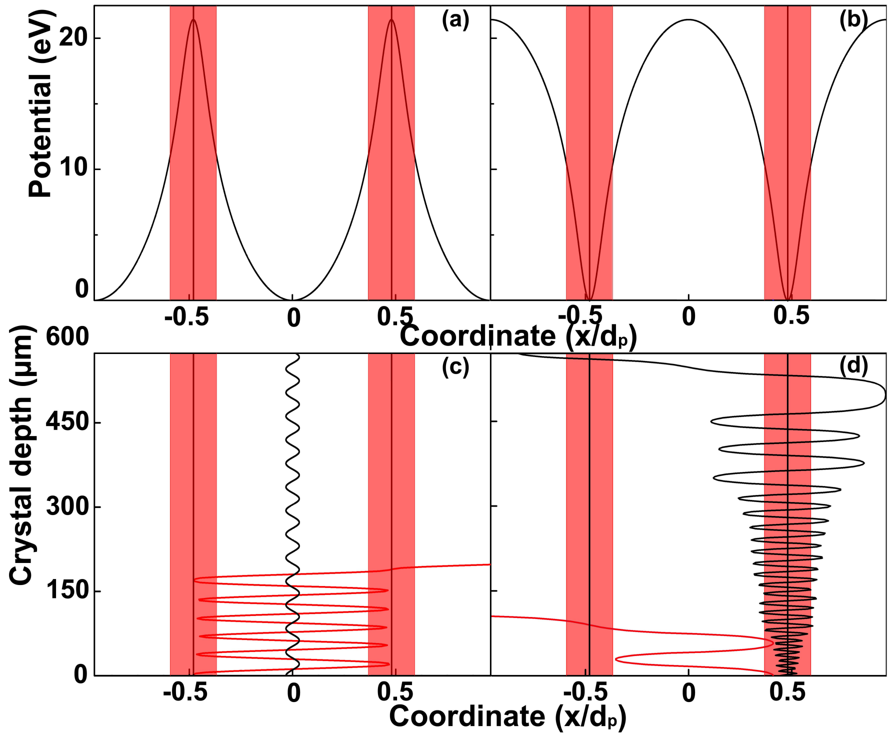

Figure 2.7: (a-b) planar potentials experienced by positive and negative particles channeled in the field (110) silicon planes. Shaded regions highlight the regions of high nuclear density (nuclear corridors), vertical lines inside those regions show the positions of atomic planes. (c) Trajectories of two 150 GeV/c π^+: the trajectory of the particle with larger oscillation amplitude is for a particle whose impact parameter lays inside the region of high nuclear density (i.e. the particle is in unstable channeling state). Such a particle is dechanneled after traversing a short distance in the crystal. The other trajectory refers to a particle impinging far from atomic planes (such particle is in stable channeling states). (d) trajectories of two 150 GeV/c π^-: all negative particles pass through the high-atomic density regions and are subject to nuclear dechanneling [47].

nuclear corridor (see Fig. 2.7 (a) and (b)). Particles crossing such areas in the interplanar channel would thus be significantly affected by nuclear scattering, consequently escaping channeled state. This kind of trajectories can occur either when a particle enters the lattice directly into the nuclear corridor or when transversal energy induces large oscillation reaching nuclei proximity. Thus it is useful to introduce the concept of critical transverse coordinate

$$x_c = \frac{d_p}{2} - 2.5u_T \tag{2.20}$$

and this other common definition of the *critical angle of channeling*

$$\theta_c = \sqrt{\frac{2E_c}{pv}} \tag{2.21}$$

where $E_c = U(x_c)$ is the critical transverse energy. Within this picture, particles impinging onto the crystal far from the atomic planes and with transverse energy $E_T \leq E_c$ are found in stable channeling states. While nuclear dechanneling acts mainly in the very first layer of the crystal, depending on the impact parameters, electronic dechanneling becomes the dominant effect afterwards. In the central zone of the interplanar potential where channeled particles oscillate, electronic density is fairly low and constant. Hence the particles slowly escape channeling as the series of minor scattering with valence electrons stochastically build up E_T. One can treat the non-conservation of transverse energy E_T for soft interactions in the framework of the diffusion theory starting from the Fokker-Planck equation [63]. Therefore, in the depth of the crystal the fraction of channeled particles decreases exponentially, $N_{ch} \approx N_{st}exp(-z/L_D)$, z being the crystal depth, N_{st} the total number of particles with $E_T \leq E_c$ at $z = 0$ and L_D the *dechanneling length*, which increases with the particle momentum. After some approximation and using the Lindhard potential for an atomic plane (eq. 2.4) in the case of high-energies ($\gamma \gg 1$), an approximated value for the electronic dechanneling length for positive particles channeled between atomic planes could be [16]:

$$L_D = \frac{256}{9\pi^2} \frac{pv}{\ln(2m_e c^2 \gamma/I) - 1} \frac{a_{TF} d_p}{Z_i r_e m_e c^2} \tag{2.22}$$

where m_e and r_e are the mass and the classical radius of an electron, I is the mean ionization energy and γ is the Lorentz factor. The diffusion approach remains valid for the electronic dechanneling, since the contribution of single strong collisions that my knock the particle out of the channeling mode at once remains small. This effect starts to become important for electronic dechanneling at energies $\geq$ GeV.

On the other hand, if a crystal is short enough to avoid the total loss of particles due to nuclear dechanneling, the numbers of channeled particles at coordinate z, $N_{ch}(z)$, over the total number of particles, N_0, can be roughly estimated as in [44], where both the dechanneling processes, which lead to a decay in the number of channeled particles, are approximated by exponential functions as following:

$$N_{ch}(z) \approx N_{un} e^{-z/L_n} + N_{st} e^{-z/L_D} \tag{2.23}$$

where N_{un} and N_{st} are the number of particles in unstable and stable channeling states at the crystal entry face ($z = 0$), respectively. For Si (110) at 300 K, $N_{un} \sim 19.5\% N_0$ and $N_{st} \sim 80.5\% N_0$. L_n and L_D are the nuclear and electronic dechanneling lengths, respectively. The electronic dechanneling is a slower process than the one due to the strong nuclear collisions. As an example, Fig. 2.7 (c) shows trajectories of two 150 GeV/c π^+ channeled in the (110) potential well depth [47]. The trajectory of the particle with larger oscillation amplitude is for a particle whose impact parameter lays inside the region of high nuclear density (i.e. the particle is in an unstable channeling state). Such a particle is dechanneled after traversing a short distance in the crystal. The other trajectory refers to a particle impinging far from atomic planes. Such particle founds in stable channeling state.

The electronic and nuclear dechanneling lengths could be measured in experiments, but it is not easy to separate the electronic long component from the nuclear short one, unless of being in special experimental conditions, e.g., through the usage of short bent crystals [44]. As an example, for 400 GeV/c protons interacting with Si (111) planes, $L_D \sim 220$ mm [64], while $L_n \sim 1.5$ mm [44].

The calculations seen above are valid in the case of motion of positively charged particles channeled between two crystallographic planes. For negative particles the planar potential is attractive and since the minimum of the potential well is located on the atomic planes, all the particles with $E_T < U_0$ at $z = 0$ are readily directed toward the nuclear corridor, crossing the dense layers of atomic nuclei (see Fig. 2.7(b)-(d)). As a consequence, all negatively charged particles lie in unstable channeling states ($N_{st} = 0$, $N_{un} = N_0$) and the mechanism of dechanneling via interaction with valence electrons negligibly contributes to dechanneling with respect to nuclear dechanneling. The diffusion approach can be used to treat also the dechanneling of negative particles, in particular for electrons [65].

A simple way to estimate the number of channeled particles at depth z is [47]:

$$N_{ch}(z) \approx N_0 e^{-z/L_{neg}} \tag{2.24}$$

Since the probability of scattering with nuclei increases, it increases also the probability of dechanneling. For this reason, the total dechanneling length for negative particles L_{neg} is much shorter than the electronic dechanneling length L_D for positive ones according to the theoretical and the experimental data [66]. Indeed, it has been shown in [47] that L_{neg} is of the order of the nuclear dechanneling length for positively charged particles L_n. As an example, Fig. 2.7(d) displays the trajectories of two 150 GeV/c π^- channeled in the field of (110) Si planes. One can notice that all negative particles pass through the high-atomic density region and are subject to nuclear dechanneling, independently on their impact parameters with atomic planes. This approach is generally correct for crystal (length $> 0.2L_e$), but in shorter crystal such approximation can lead to slight overestimation of the efficiency. In delicate experimental setup such as LHC, where crystal effect on the beam dynamics must be calculated with few percent accuracy, this effect is indeed relevant. In this case, fraction of the channeled particles as a function of penetration in the crystal can be calculated starting from the diffusion equation whose solution is

$$P_{ch}(z) = \frac{N_{ch}(z)}{N_0} = \frac{1}{N_0}\sum_{n=1}^{\infty} A_n e^{-\lambda_n z} \tag{2.25}$$

Where $N_c h$ are the channeled particles, N_0 are the total number of particles in the beam. It is easy to see how for long crystal the approximation of the summation to the first term $()A_1 \approx 1$ and $\lambda_1 \approx \frac{1}{L_e})$ may not create issue, while for shorter length also the other parameter are non-negligible. Also the definition of the nuclear corridors is model dependent, and thus may lead to some discrepancies. Thus Monte Carlo simulation are needed in order to confirm results of analytical model when high precision is critical.

The stochastic nature of the dechanneling mechanisms leads to the existence of an opposite process to dechanneling. The rechanneling phenomena consists in the scattering processes (both with electrons and nuclei) that modify a free particle trajectory into a channeled state. The reversibility rule [1] assures that for any trajectory of a particle in a crystal a time-reversed trajectory is possible. Therefore, as well as there are particles that leave channeling mode in the depth of a crystal, the are particles entering the channeling mode (*feeding in*). This effect should be taken in account as could modify in non-negligible manner the channeled fraction of a beam.

2.2.3 Axial Channeling

The continuous approximation can be used also in the case of a particle aligned with the atomic strings. In such case, a charged particle is influenced mostly by a crystal axis, which generates a stronger electric field than for a plane. According to Lindhard, the axial continuous potential averaged along the longitudinal coordinate of the string can be written in the form [16]:

$$U_{ax}(r) = \frac{Z_i Z e^2}{a_i} ln\Big(1 + \frac{3{a_{TF}}^2}{r^2}\Big) \tag{2.26}$$

where a_i is the interatomic spacing in the string and r is the distance from the particle to the axis (see Fig. 2.8).

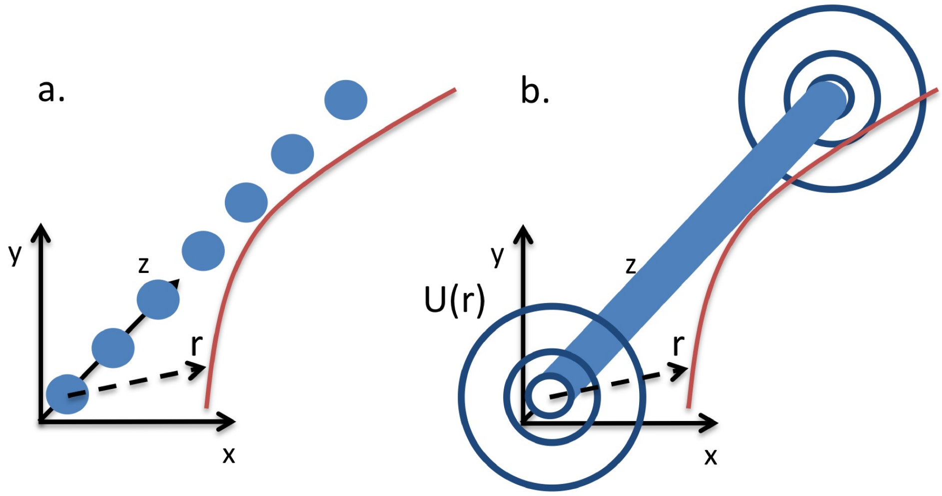

Figure 2.8: a) Trajectory of positive particle moving in a crystal aligned with respect to a crystal axis. b) Continuous potential U(r) is felt by the particle mainly due to the neighbouring axis.

Whereas in planar channeling particles are confined along one dimension, axial channeling features two degrees of freedom in the radially symmetric field of $U_{ax}(r)$. Thus transverse motion is characterized by two conserved quantities, the angular momentum L and the transverse energy E_T in the transverse plane. If a particle imping onto a crystal axis with a small angle ψ, with projections $\psi_r = dr/dz$ directed toward the axis z and $\psi_\phi = rd\phi/dz$ perpendicular to it ($\psi^2 = \psi_r^2 + \psi_\phi^2$). The conserved transverse energy can be expressed as

$$E_T = \frac{pv}{2}\psi^2 + U(r) = \frac{pv}{2}\left(\frac{dr}{dz}\right)^2 + \frac{L^2}{2m\gamma r^2} + U(r), \tag{2.27}$$

m being the particle mass. The particle motion in the axial field is then defined by the following equations

$$dz = \frac{dr}{\sqrt{2/pv[E_T - U(r)] - L^2/p^2r^2}}, \tag{2.28}$$

$$d\phi = \frac{L/r^2 dr}{\sqrt{2m\gamma[E_T - U(r)] - L^2/r^2}}. \tag{2.29}$$

Although axial potential is deeper than the corresponding planar counterpart, confinement around a single atomic string is less strong than the confinement between two adjacent planes. Indeed, positive particles while bound to the potential may still diffuse to other neighbour axes. Another difference from the planar case appears for negatively charged particles with large E_t and L (but not larger than critical values): these features leads to wider orbit around the nuclei at the minimum of the potential, thus reducing scattering wrt planar channeling and amorphous medium.

2.2.4 Energy Loss

Energetic heavy charged particles in an amorphous substance (or a misaligned crystal), lose energy mainly in inelastic collisions with atomic electrons, i.e., through ionization energy losses. The *stopping power* dE/dx, x being the depth penetration, is described by the Bethe-Bloch formula and the energy loss shows the Landau distribution form [60]. The frequent soft collisions, that cause only an excitation, provide a Gaussian-like peak in the energy loss spectrum, while the rare close hard collisions, in which the energy transferred is sufficient to cause ionization and eventually secondary ionization ($\delta - rays$), contribute to the long high-energy tail and to the spread of the energy-loss distribution.

When a positively charged beam is aligned with respect to atomic planes it could be divided in two parts: channeled beam (with $x \leq x_c$) and random beam (with $x > x_c$). The channeled beam moves in a region with lower electron density as compared to the amorphous case (see Fig. 2.9 (a)), so the contribution due to hard collisions is suppressed. For this reason, both the average loss of energy and its spread are decreased compared to the amorphous case. A quantitative description of the position-dependent energy loss was given by Esbensen and Golovchenko [67]. On the contrary, since negatively charged particles oscillates around planes, the ionization losses for channeled particles are comparable to the one for amorphous medium. In fact, in the case of axial channeling, negatively charged particles oscillate around axes, thus seeing an increased atomic density as compared to amorphous case. The result is an increase of energy loss as compared to random orientation (about the 20% more for GeV negative particles) [68].

Furthermore, because of their small mass, electrons and positrons not only lose energy in collisions with atoms, but also in the emission of electromagnetic radiation arising from scattering in the electric field of a nucleus (**Bremsstrahlung**) [8]. At energies larger than the critical one [69],

$$E_c \approx \frac{610MeV}{Z + 1.24}, \tag{2.30}$$

bremsstrahlung dominates in the energy losses of electrons and positrons as compared to ionization losses (see in Fig. 2.9(b)). In silicon, $E_c \sim 40$ MeV.

As introduced before, the e.m. radiation emitted by e^+/e^- through coherent interactions is more intense than for common bremsstrahlung in an amorphous medium. Such increase occurs not only for channeling, thereby called *channeling radiation* (CR) [70], but also in the case of particles that move in over-barrier states in the fields of several atomic planes or axes [6]. A qualitative description on the process of e.m. radiation emission in oriented crystals is presented in Chapter 3.

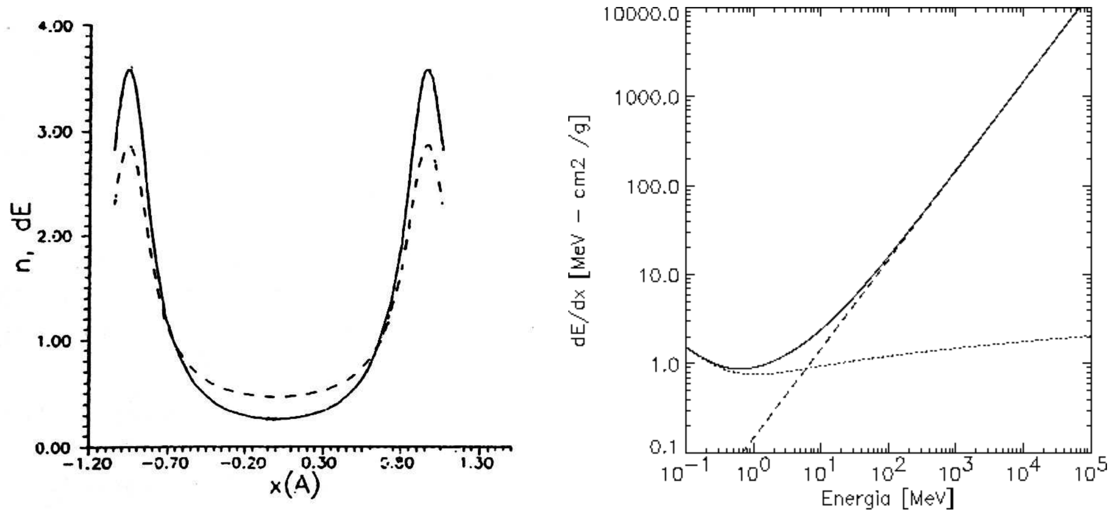

(a) (b)

Figure 2.9: (a) The electronic density (*solid line*) and the mean ionization energy loss (*dashed line*) in an aligned crystal, normalized to the amorphous values, in Si(110). (b) Stopping power for electrons in tungsten (solid-line): bremsstrahlung contribution (dashed-line) and Bethe-Bloch one (dot-line). Adapted from [16]

2.3 Coherent interactions in bent crystals

2.3.1 Planar Channeling in a bent crystal

The concept of exploiting channeling in bent crystal to deflect high energy charged particle beam was first conceived by Tsyganov in 1976 [12]. His hypothesis was that particles bound to lattice structure would remain so when crystal was bent, hence gaining an angular shift after crossing the medium.[3]

In case of macroscopic curvatures (from $\approx cm^{-1}$ to several m^{-1}), bending has a negligible effect on the planar (axial) potential in the angstroms scale of the laboratory inertial frame (see Fig. 2.10(a)). On the contrary, in the non-inertial reference frame (comoving with a particle channeled with zero transverse momentum along the bent planar channel) a centrifugal apparent force appears due to the bending of the crystal (see Fig. 2.10(b)).

[3]In this Section, we follows mainly the book [16].

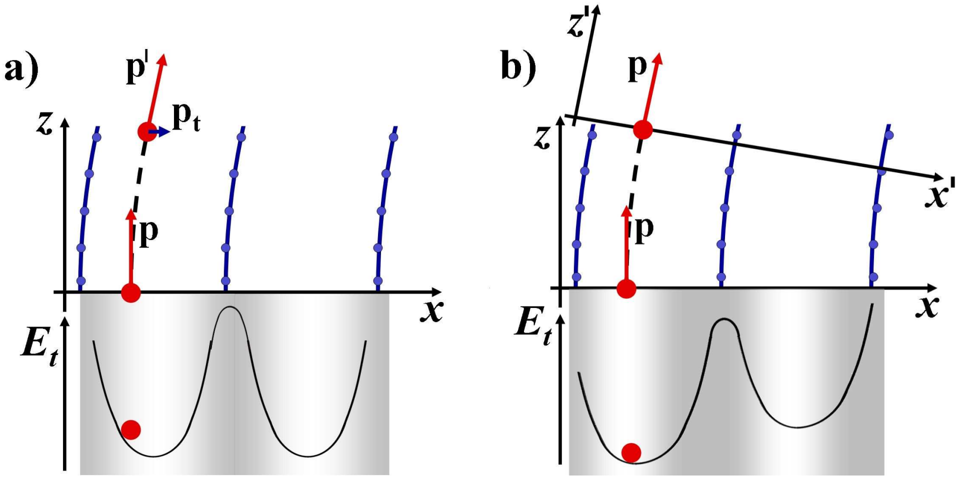

Figure 2.10: Scheme of the channeling motion of a positive particle that enters in the channel aligned with respect to the crystal planes: a) in the laboratory inertial frame; b) in the non-inertial comoving reference system which rotates with the particle; the centrifugal force appear. Adapted from [55].

In the lab-frame, a particle enters in the channel aligned with the crystal planes, i.e. with transverse momentum $p_t = 0$, and during the motion the particle acquires a non-zero p_t in order to follow the channel bending. In other words, the interplanar continuous potential exerts a force that modifies the particle momentum. On the other hand, in the comoving reference frame the particle momentum direction does not change, but a centrifugal force directed towards the external side of the channel appears. In the comoving frame, where z axis follows the direction of bent atomic planes and x is the transverse coordinate defined with respect to atomic planes at some point z, the equation of motion 2.14 for a channeled particle becomes:

$$pv\frac{d^2x}{dz^2} + U'(x) + \frac{pv}{R(z)} = 0, \tag{2.31}$$

x and z being the transverse and longitudinal coordinates in the comoving frame, respectively, while $1/R(z)$ is the local curvature of the channel. If the bending radius R is independent from z, the particle moves as if it was in an *effective* interplanar potential of the form:

$$U_{eff}(x) = U(x) + \frac{pv}{R}x, \tag{2.32}$$

with a transverse energy $E_T = \frac{pv}{2}\theta^2 + U_{eff}(x)$.

Fig. 2.11 shows some examples of $U_{eff}(x)$ for different pv/R ratios for the Si planes (110), as compared to the case of unperturbed potential $U(x)$ for positive particles. If pv/R increase, the depth of the effective potential well decreases while its minimum value

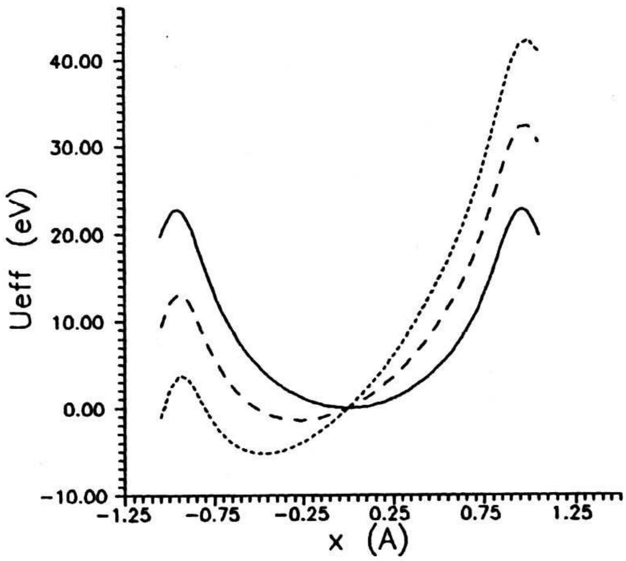

Figure 2.11: The interplanar potential in Moliére approximation for Si (110) (*solid line*) and the effective potential for pv/R of 1 GeV/cm (*dashed line*) and 2 GeV/cm (*dotted line*) [16].

is shifted towards the atomic plane. For these reasons, at some critical $(pv/R)_c$ the well completely disappears and channeling becomes impossible. The critical radius of curvature is defined by the maximal interplanar electric field ε_{max} near the atomic planes:

$$R_c = \frac{pv}{e\varepsilon_{max}}. \tag{2.33}$$

For instance, $e\varepsilon_{max}$ is about 6, 12 and 48 GeV/cm for (110) planes in Si, Ge and W, respectively. The depth of the potential well in the case of bent crystal is ${E_c}^b(R_c/R) = E_c(1 - R_c/R)^2$, where E_c is the critical transverse energy in a straight crystal. Following this definition, it is possible to define the critical angle for bent crystals:

$${\theta_c}^b(R_c/R) = \theta_c\,(1 - R_c/R)\,, \tag{2.34}$$

θ_c being the critical angle for a straight crystal. One can notice that ${\theta_c}^b$ is reduced of a factor $(1 - R_c/R)$ from θ_c. Dechanneling length may be affected as well due to the modified potential wrt the straight crystal case. Such variation in case of constant bending radius along the whole curvature can be easily estimated by the formula:

$$L_D(R) = L_D(\infty)\left(1 - \frac{R_c}{R}\right)^2 \tag{2.35}$$

In the evaluation of the channeling efficiency for a bent crystal, the contribute to dechanneling caused by bending may be approximated as an a mere acceptance issue (eq. 2.34) and compute electronic dechanneling with modified dechanneling length (eq. 2.35). This should be applied only for constant bending situation, where along all the curvature R value does not change.

Lattice quality and radiation damage

Channeling phenomenon heavily depends on the presence of the regular and periodic arrangement of atoms occurring in crystals. Previous discussion considered a perfect lattice, with atoms displacement from theoretical structure caused only by thermal vibration. In a real crystal, atoms may indeed be misplaced, and localized alteration of the lattice may appear. It is thus of great concern to quantify the effects of defects on coherent phenomena. Presence of single atomics vacancies or interstitial gives lower influence since during each oscillation a channeled particle would interact with huge number of atoms, hence individual contributions is masked by the rest of. It can be safely assumed that point defects influence decreases as $\lambda \propto \sqrt{pv}$, where λ is the oscillation period. Dislocation effect instead grows as beam energy increases [71]. Indeed, dislocations induce stress in the lattice and hence a deformation. The local curvature radius R_l at a distance r from the dislocation can be estimated by formula

$$R_l = b\frac{g^2(\nu)}{2r^2} \tag{2.36}$$

where b is the burger vector which define the dislocation deformation on the lattice structure, and g is a coefficient dependent on the Poisson's ratio ν

$$g(\nu) = \frac{3 - 2\nu}{2\pi(1 - \nu)} \tag{2.37}$$

As critical radius increases with particle energy (see eq2.33), consequently channeled particles becomes more sensitive to change in local curvature as well. For 7 TeV proton of LHC, crystal should avoid dislocation density $> 1/cm^2$. This strongly limits the potential material to be used for crystal assisted collimation/extraction to silicon and germanium (possibly diamond as well). Semiconductor industry is constantly improving crystalline perfection of other material as well (silicon carbide, gallium arsenide) and in future more material could be selected. As logical consequence of the importance of a lattice quality close to perfection in high energy application, radiation damage on the crystal should be addressed as well. Indeed, quality of the lattice must be preserved during operation to ensure efficient coherent phenomena. Several experiments on silicon crystals were performed in order to empirically test lattice radiation hardness and its effect on deflection features (see table 2.2).

$proton/cm^2$	energy [GeV]	Effect
10^{17}	400	no effect on deflection efficiency [72]
10^{18}	28	no damage detected by RBS [73]
2.9×10^{19}	70	no difference observed in deflection efficiency [74]
$(4.1 \pm 1.4) \times 10^{20}$	28	damage observed with RBS, no test on channeling [75]
5×10^{20}	450	30% reduction in deflection efficiency[76]

Table 2.2: list of experiments related damage of ultrarelativistic particles passage in crystal

The results in table 2.2 shows good stability of silicon up to $10^{19} protons/cm^2$, while from $10^{20} protons/cm^2$ dose damage starts to be observed. It is also worth mentioning that in [75, 76] irradiation was not performed in alignment with crystals, thus they did not benefit from channeling which would have suppressed energy deposition in the samples. Scaling the results achieved to other energy is not trivial task. Interaction with lattice during channeling and nuclear cross section with atom nuclei depends on energy, as well as lattice quality condition for efficient crystal assisted beam steering. Nevertheless, for collimation applications or other parasitic application on accelerator beam intensity should endure low flux.

2.3.2 Dynamics of over-barrier particles in bent crystals

As stated previously a particle crossing a crystal in close alignment with its planes and axes interacts with an ordered and periodic continuous potential instead of random scattering sites. When a particles transverse energy exceeds the potential well depth (over-barrier particle), although not in a bound state they are still affected by it. Indeed, particles motion can feature two coherent orientational effects when the medium crystal is bent [77]. More precisely, two different effects have been discovered:

- Volume reflection (**VR**);
- Volume capture (**VC**).

Fig. 2.12 shows the scheme of the different possible planar coherent interactions between a charged particle and a straight or a bent crystal. Fig. 2.12(a)-(c) represents the motion of an unchanneled positive particle and a channeled one in a straight crystal in the plane (x, E_T) (a) and in the plane (x, z), (c). On the other hand, in Fig. 2.12(b)-(d) the motion of positive particles in channeling, VR and VC conditions is shown in the planes (x, E_T) and (x, z). In next paragraphs the VR and VC effects are described.

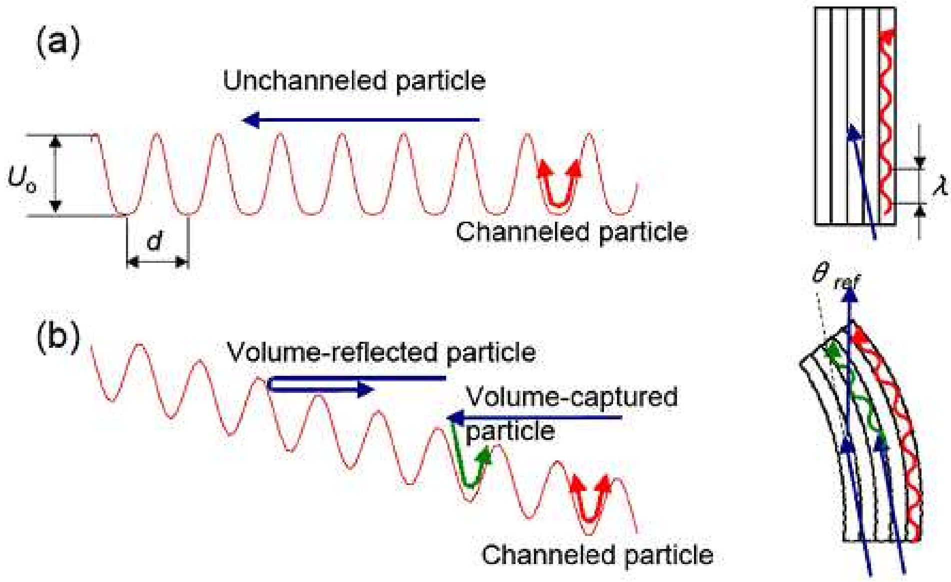

Figure 2.12: (a)-(c) Channeled and unchanneled particle in a straight crystal; (b)-(d) particle in channeling, VR and VC conditions in a bent crystal [78].

Volume Reflection

In a bent crystal, even if a particle trajectory is misaligned from planes with an angle exceeding the critical one introduced by Lindhard, i.e. being over-barrier, its trajectory may become tangential to the crystallographic planes during the motion (and so tangential to the planar potential) due to the curvature of the plane itself (see Fig 2.13)). VR consists in the reversal of transverse momentum of over-barrier particles by the interaction with the planar potential barrier at the tangency point [4]. As a result, volume-reflected particles are deflected by an angle of the order of the Lindhard angle θ_c to a direction opposite to that of channeled particles. In other words, in a bent crystal not only channeled but also unchanneled particles can be deflected. Features of angular acceptance and total angular deflection are opposite to the case of planar channeled particles. The angular acceptance for VR is equal to the bending angle of the crystal (l/R, where l is the crystal length) because any particle with an angle of incidence $\theta_c < \theta_{in} < l/R$ will become tangent to bent crystal planes at some depth of the crystal. Over-barrier motion in similar for both

[4]In this section we will follow mainly the paper [79].

positive and negative particles and deflection is imparted to trajectory in a single point and depends only to potential depth. These features do not discriminate between negative and positive particles, indeed it was observed as VR is and efficient steering mechanism for both cases [80–82].

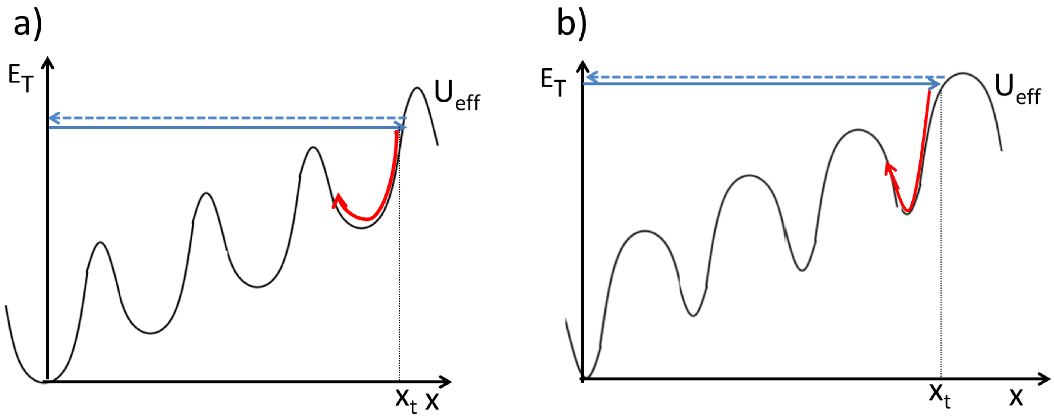

Figure 2.13: Reflection and capture of a charged particle in the crystal volume at the comoving transverse coordinate x_t. Phase space of the particle transversal energy as a function of x comoving with the bent planes either for positive (a) or negative (b) particles.

For large bending radius ($R \gg R_c$), the deflection angle for VR, is about $\theta_{VR} \approx 2\theta_c$, for positively charged particles, while being smaller for negative particles, due to the shape of the effective interplanar potential [77]. Indeed, the reflecting region for a negative particle (between the planes) is nearly flat and the particle has to accomplish a longer path near turning points as compared to positive particles (see Fig. 2.13(b)).

If the curvature increases, the reflective area, ΔU, increases (see Fig. 2.14), leading to deflection angles θ_{VR} below $2\theta_c$. This can be ascribed to the fact that reflection may occur in points in which the interplanar potential is less intense. On the other hand, the increasing in the reflective area, increases the VR deflection efficiency [83].

Summarizing, VR shows a wider angular acceptance with respect to planar channeling, while a smaller angular deflection ($\theta_{VR} \sim \theta_c$). Drawback of the phenomenon for application in steering particles is the impossibility to select an arbitrary deflection angle. This becomes a serious limitation as particles energy increase, as the reflection angle would gradually decrease (only few micro-radians or less at TeV range). With the aim of increasing the deflection angle of VR while maintaining a large angular acceptance, the possibility to exploit the effect of a multi-VR in a series of bent crystals or in a single crystal has been suggested and experimentally validated [40, 84].

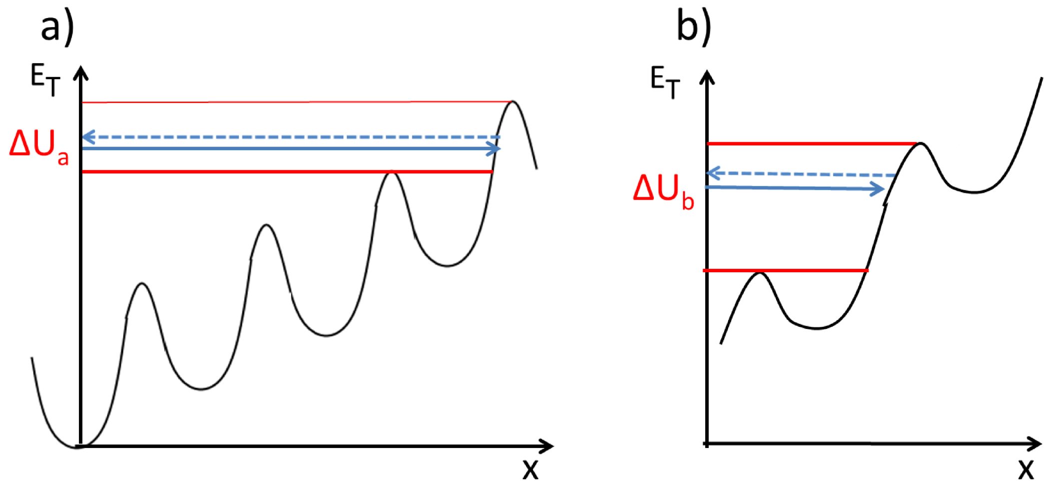

Figure 2.14: (a) and (b) are the phase spaces of the particle's transversal energy, with $R_a > R_b$. The reflective area $\Delta U_a < \Delta U_b$.

Volume Capture

In section 2.2.2, the dechanneling (*feeding out*) mechanism in a straight crystal has been described. The reversibility rule assures that if some particles leave the channel, there have to be particles entering in the channeling mode (*feeding in*) [1]. The feeding in/out processes are caused by the incoherent scattering that may change the transverse energy of the particle (see Fig. 2.13 red lines). More in details, the feeding out (dechanneling) is the transition of a particle from the channeled to the beam ('over barrier'), while the feeding in (re-channeling) describes the transition of a particle state from the random beam into a channeled state.

Volume capture is a directional coherent feed-in process occurring in bent crystals [85, 86]. The above paragraph painted out that when a beam passes through a bent crystal, a large part of the beam is reflected in the region of tangency with the bent planes. This is not the only type of motion possible for these particles. Indeed, a fraction of such particles are captured into the planar channel due to incoherent scattering with crystal atoms. In other words, VC is a mechanism that generates VR inefficiency. Since VC has the same broad angular acceptance of VR, it is more efficient than the feeding-in mechanism in straight ones. As a result, in a bent crystal the feeding out mechanism increases according to the reversibility rule. For instance, in the case of positive particles the dechanneling probability increases in a bent crystal because of the decreasing of the potential well E_c (θ_c) and because channeled particles are shifted towards atomic planes.

VC probability depends strongly on the bending radius: it decreases for smaller R, according to the decreasing of the planar potential well depth.

2.4 Magnetic and Electric Dipole Precession

The magnetic dipole moment (MDM) and the electric dipole moment (EDM) are static properties of particles that determine the spin motion in an external electromagnetic field, as described by the T-BMT equation[87–89]. Theoretical predictions of such quantities are being tested in several experiments for a wide range of physical systems such as free particles, atoms, molecules and condensed state matter. MDM measurements are useful in order to validate the quark model structure in baryons [90]. Current models indicate charm quark as main contribution to the total MDM of the baryon, thus the investigation would imply an almost direct measure of charm quark MDM (only indirect search was performed at BESIII for Δ_c). Additionally, charmed baryons states while being of similar mass are efficiently distinguished by study related to spin. MDM measures on charmed baryons would help study charmed baryon spectroscopy as well.

EDM is of great interest as it is the only static property of a particles which requires the violation of parity (P) and time reversal (T). Consequently, to conserve CPT invariance, EDM implies violation of CP. Thus, EDM is a very small quantity, and it is highly suppressed and generally QED calculations set its value lower than current experiments sensibility. Hence excess of EDM measured would lead to a CP violation mechanism beyond standard model. New physics models are largely influenced by EDM maximum values, thus as many as possible experimental limits are extremely useful to refine them. Indirect bounds on charm (beauty) quark EDM are set from different experimental measurements and span over several orders of magnitude, i.e. charm (beauty) EDM $\lesssim 10^{-15} - 4.4 \times 10^{-17} e\ cm$ [91–95] ($\lesssim 2 \times 10^{-12} - 2 \times 10^{-17} e\ cm$[93–96]), depending on different models and assumptions.

Direct observation of charmed baryon EDM and MDMD have never been performed until now. Indeed, such measure holds great experimental difficulties as particles have extremely short lifetime of $10^{-13} - 10^{-12} s$. Thus, in order to manipulate significantly these particles extremely intense fields should be employed. Crystal are an available source of them thanks to the large internal fields bound to continuous potential.

The possibility to measure the MDM of short-lived baryons using channeling in bent crystals was firstly pointed out by V.G. Baryshevsky in 1979. The method is based on the interaction of the MDM of the channeled particles with the intense electric field between crystal atomic planes. The measurement of the MDM of charm baryons using bent crystals has been widely discussed since the 80's [97–99]. Lately, the possibility of the measurement at LHC energies has been considered [100–102], while the search for charm baryon EDM using bent crystals at LHC has been first proposed in [103]. Here a quick explanation of the theory about EDM and MDM contribution to spin precession and how it behaves in bent crystal during planar channeling.

2.4.1 Spin precession

The spin precession of a charged particle is induced by the interaction of its electromagnetic dipole moments, e.g. MDM and EDM, with external electromagnetic fields. The time evolution of the spin-polarization vector $\mathbf{s}$ is regulated by the T-BMT equation

$$\frac{d\mathbf{s}}{dt} = \mathbf{s} \times \mathbf{\Omega}, \quad \mathbf{\Omega} = \mathbf{\Omega}_{\text{MDM}} + \mathbf{\Omega}_{\text{EDM}} + \mathbf{\Omega}_{\text{TH}}, \tag{2.38}$$

where the precession angular velocity vector $\mathbf{\Omega}$ is composed by three contributions corresponding to the MDM, EDM, and Thomas precession:

$$\begin{aligned}
\mathbf{\Omega}_{\text{MDM}} &= \frac{g\mu_B}{\hbar}\left(\mathbf{B} - \frac{\gamma}{\gamma+1}(\beta \cdot \mathbf{B})\beta - \beta \times \mathbf{E}\right), \\
\mathbf{\Omega}_{\text{EDM}} &= \frac{d\mu_B}{\hbar}\left(\mathbf{E} - \frac{\gamma}{\gamma+1}(\beta \cdot \mathbf{E})\beta - \beta \times \mathbf{B}\right), \\
\mathbf{\Omega}_{\text{TH}} &= \frac{\gamma^2}{\gamma+1}\beta \times \frac{d\beta}{dt} = \frac{q}{mc}\left[\left(\frac{1}{\gamma} - 1\right)\mathbf{B} + \right. \\
& \left. \frac{\gamma}{\gamma+1}(\beta \cdot \mathbf{B})\beta - \left(\frac{1}{\gamma+1} - 1\right)\beta \times \mathbf{E}\right],
\end{aligned} \tag{2.39}$$

where $\mathbf{E}$ and $\mathbf{B}$ are the electric and the magnetic fields in the laboratory rest frame, and q, γ and β are the electric charge, boost and vector velocity of the particle, respectively. The g and d dimensionless factors indicates the gyromagnetic and gyroelectric ratios, which are used to define the magnetic and electric dipole moment of a particle with spin J (in Gaussian units)

$$\boldsymbol{\mu} = Jg\mu_B\boldsymbol{s} \qquad (MDM)\boldsymbol{\delta} = Jd\mu_B\boldsymbol{s} \qquad (EDM) \tag{2.40}$$

where $\mu_B = e\hbar/(2mc)$ is the particle magneton[5].

[5]The spin-polarization vector is defined such as $\mathbf{s} = \langle\mathbf{S}\rangle/(J\hbar)$, where $\mathbf{S}$ is the spin operator.

As seen in equations 2.39, spin changes with velocity proportional to the fields applied. Thus for evanescent particles with short lifetime ($\tau_{\Lambda_c^+} \approx\ 10^{-13}s$) such as charmed baryons, spin change would result undetectable when using artificial electromagnetic fields.

2.4.2 Spin precession in planar channeling

The spin precession of particles channeled in bent crystals was firstly observed by the E761 Collaboration [54]. Using a 800 GeV/c proton beam impinging on a Cu target, Σ^+ baryons with 375 GeV/c average momentum were produced and channeled in two bent crystals with opposite bending angles. The MDM of the Σ^+ baryon was measured and proved the viability of this technique for the measurement of the MDM of short-lived particles. Indeed, during planar channeling particles are subjected to the intense electric field between two crystal planes $\mathbf{E}$. In the reference frame following the particle inside along its motion, the electric field is transformed into an electromagnetic one

$$\mathbf{E} \rightarrow \begin{cases} \mathbf{E}^* \approx \gamma \mathbf{E} \\ \mathbf{B}^* \approx -\gamma \boldsymbol{\beta} \times \mathbf{E}/c \end{cases} \tag{2.41}$$

The already intense fields are further enhanced by the Lorentz transformation by a factor γ. In the limit of large boost, the spin precession induced by the MDM in the yz plane is [104]

$$\Phi \approx \frac{g-2}{2}\gamma\theta_C. \tag{2.42}$$

Where θ_c is the angle the channeled particle is being deflected. Such precession angle reaches the range of 1 rad after large deflection ($\theta_c \approx 1 - 10mrad$) for relativistic particles with Lorentz factor $\gamma \approx 10^{2-3}$.

The equations describing the spin precession of planar channeled positive particles in presence of MDM and EDM are derived in Ref. [103]. In the limit of large boost, and assuming small EDM effects compared to the main MDM spin precession, a polarization component orthogonal to the bending plane is induced by EDM momentum itself.

$$s_x \approx s_0 \frac{d}{g-2}(\cos\Phi - 1). \tag{2.43}$$

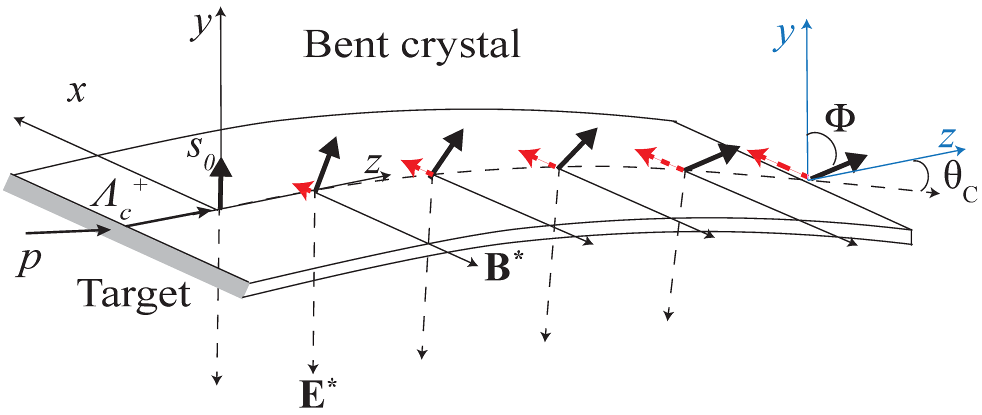

Figure 2.15: Sketch of the deflection of the Λ_c baryon trajectory and spin precession in a bent crystal. The initial polarization vector $\mathbf{s_0}$ is perpendicular to the production plane, along the y axis, due to parity conservation in strong interactions. The spin precession in the yz and xy planes are induced by the MDM and the EDM, respectively. The red (dashed) arrows indicate the (magnified) s_x spin-polarization component proportional to the particle EDM. The Φ angle indicates the spin precession due to the MDM. [53]

The effect of MDM driven precession taking place in the bending plane is given by

$$\begin{aligned} s_y &\approx s_0 \cos \varPhi, \\ s_z &\approx s_0 \sin \varPhi. \end{aligned} \tag{2.44}$$

In the following, we demonstrate that in presence of a non-harmonic potential V, identical spin precession equations derived for the harmonic potential case hold. We consider the layout of Fig.2.15, with the crystal bent along an atomic plane. Polar coordinates are introduced for describing the particle trajectory in the bending plane

$$y(t) = \rho(t)\cos(\Omega t), \quad z(t) = \rho(t)\sin(\Omega t), \tag{2.45}$$

where Ω is the revolution frequency for the particle traversing the bent crystal, and the electric field described by the planar channel potential $V(\rho)$ is

$$\mathbf{E} \;=\; \begin{cases} E_x = 0 \\ E_y = -\dfrac{dV}{d\rho}\cos(\Omega t) \\ E_z = -\dfrac{dV}{d\rho}\sin(\Omega t)\ . \end{cases} \tag{2.46}$$

Neglecting EDM contributions, the spin evolution resulting from Eqs. (2.38), (2.39), (2.45) and (2.46) is

$$\mathbf{s}(t) \;=\; \begin{cases} s_x(t) = 0 \\ s_y(t) = s_0 \cos\left(\dfrac{2\mu'\Omega}{\hbar c}\displaystyle\int_0^t \rho \frac{dV}{d\rho} dt'\right) \\ s_z(t) = s_0 \sin\left(\dfrac{2\mu'\Omega}{\hbar c}\displaystyle\int_0^t \rho \frac{dV}{d\rho} dt'\right), \end{cases} \tag{2.47}$$

for the initial condition $\mathbf{s}_0 = (0, s_0, 0)$ and where

$$\mu' \equiv \frac{g-2}{2}\frac{e\hbar}{2mc}. \tag{2.48}$$

The radial coordinate ρ is constant up to $\delta\rho/\rho = \mathcal{O}(\text{Å}/m) = 10^{-10}$, therefore the spin precession depends on $\int_0^t dV/d\rho\; dt'$. Over a complete oscillation in the channel potential the effect of this term is equivalent to that of the electric field in the particle equilibrium radial position ρ_0',

$$\int_0^t \frac{dV}{d\rho} dt' = -E(\rho_0')t, a \tag{2.49}$$

which is determined solely by the centripetal force f_c induced by the bending on the lattice planes (see section 2.3)

$$E(\rho_0') = -\frac{f_c}{e} = -\frac{m\gamma c^2}{e\rho_0'}. \tag{2.50}$$

This statement follows by computing

$$\int_0^t \frac{dV}{d\rho} dt' - [-E(\rho_0')t] = \int_0^t \left(\frac{dV}{d\rho} - \frac{f_c}{e}\right) dt' \tag{2.51}$$

for a complete particle oscillation. By changing the integration variable to $d\rho$ and $dt' = d\rho/\dot{\rho}$, then $\dot{\rho}$ is determined by the non-relativistic energy conservation for the radial motion of channeled particles [16]

$$\frac{1}{2}M\dot{\rho}^2 + eV(\rho) - f_c\rho = W_r, \tag{2.52}$$

in which $M = m\gamma$ and W_r is the total radial energy, assumed to be constant during a particle oscillation. The relation holds because the longitudinal motion is ultra-relativistic and independent from the radial one, which is non-relativistic since the potential depth is $\mathcal{O}(100eV) \ll m$. The integration boundaries $\rho_{1,2}$ are chosen to be the particle oscillation limits, in which

$$\frac{1}{2}M\dot{\rho}^2 = 0 \leftrightarrow eV(\rho_{1,2}) - f_c\rho_{1,2} = W_r\ . \tag{2.53}$$

Finally, the integral can be trivially computed

$$\begin{aligned}
&\sqrt{\frac{m}{2e}}\int_{\rho_1}^{\rho_2}\frac{e\frac{dV}{d\rho}-f_c}{\sqrt{W_r+f_c\rho-eV(\rho)}}d\rho \\
&=-\sqrt{\frac{m}{2e}}\Big(\sqrt{W_r+f_c\rho_2-eV(\rho_2)} \\
&-\sqrt{W_r+f_c\rho_1-eV(\rho_1)}\Big) \\
&=0.
\end{aligned} \tag{2.54}$$

Summarizing, spin precession effects given by the actual shape of the planar channel potential cancel out at each particle oscillation and the net spin precession depends uniquely on the crystal curvature. This result generalises the same conclusion previously obtained for harmonic potentials [97, 104]. The spin evolution equations describing MDM and EDM effects, Eqs. (2.42), (2.43) and (2.44), hold as for a harmonic planar channel potential.

Chapter 3

Electromagnetic radiation emitted by ultrarelativistic electrons and positrons in straight and bent crystals

The lattice structure studied in 2 influences not only particle motion, but also affects radiation emission. Indeed, for a moving charged particles radiation strongly depends on the trajectory and its accelerations. Channeled particles motion features oscillations in the potential well which do not take place in amorphous medium, and over-barrier particles cross planes and axes with period dependent on impinging angle. If a crystal is slightly bent, the particle dynamics is modified and so the process of radiation generation.

In this chapter, a brief qualitative description of e.m. radiation emission process in straight and bent crystals is introduced.

3.1 General features of emission of radiation by high-energy particles in straight crystals

In this Section, a brief description of the radiation emission process in straight crystals is given following mainly the book of Baier, Katkov and Strakovenko [58]. From the classical electrodynamics it is well known that an accelerating charged particle in an external electromagnetic field emits electromagnetic radiation [105]. For ultrarelativistic particles Lorentz factor $\gamma \gg 1$, hence its total energy ε is much larger than its rest mass following from $\gamma = \varepsilon/mc^2$. Radiation stimulated from transversal acceleration benefits from γ^2 boost wrt the case of longitudinal acceleration [58, 105]. Indeed, the latter contribution can be usually neglected and only the calculation from the first can be carried out. The e.m. radiation is emitted mainly forward into a narrow cone, with opening $\theta_\gamma \sim 1/\gamma$, along the particle velocity.

In general [105, 106], a critical feature to define radiation processes consists in the ratio between total deflection angle $\Delta\vartheta$ in the external field and the typical radiation angle $1/\gamma \ll 1$. If $\Delta\theta \ll 1/\gamma$, the whole radiation emitted by the particle is contained within the narrow cone with an opening angle $\sim 1/\gamma$ and it is determined by nearly the whole particle trajectory. On the opposite situation, when $\Delta\theta \gg 1/\gamma$, only a portion of the total trajectory supports radiation emitted within the emission cone $1/\gamma$. This fraction of trajectory is called the radiation formation length $l = R/\gamma$, where R is the instantaneous bending radius. If the external field does not vary too much along l, one may neglect the variation of the field within the formation length, thus considering the external field as constant. This is the case of *uniform field approximation*, which is typical of synchrotron radiation.

In the case of periodical or quasi-periodical motion, which is typical for many cases of interactions between charged particles and crystals[1], these two limits can be rewritten by comparing the radiation formation length (coherence length) with the oscillatory period (λ) of the particle motion:

- CASE 1: $\lambda \ll l$, the radiation is formed on many periods λ hence interference effects are relevant.

- CASE 2: $\lambda \gg l$, the radiation is formed inside each period, so that the total intensity of radiation is a non-coherent sum of intensities for each λ.

As for the studies on motion in bent crystal, for a straightforward understanding of the qualitative features of radiation emitted in quasi-periodical motion, it is more convenient to work in the co-moving frame, in which the mean particle velocity is zero (see section 2.3). If the transverse velocity of the particle, $v_\perp$, remains non-relativistic in the co-moving frame, the radiation features a *dipole* nature. I.e. the transverse displacement during the formation length $\Delta x \sim \Delta\theta l$ is small compared to the emitted wavelength [107], and radiation can be fully determined by the Fourier components of the particle velocity. This corresponds to CASE 1, for which few first harmonics, multiples of the frequency of the

[1]In this list, we exclude the chaotic motion typical of above-barrier particles in the field of many crystal axes [107].

particle motion, are emitted, *i.e.*, the radiation monochromaticity is inversely proportional to the number of harmonics.

The frequency of radiated photon in the laboratory reference frame is obtained through the Doppler effect:

$$\omega \approx \frac{\alpha\omega_0}{1 - \mathbf{n}\cdot\mathbf{v}} \approx \frac{2\gamma^2\omega_0\alpha}{1+\gamma^2\theta^2}, \tag{3.1}$$

ω_0 being the frequency of the particle's motion in the laboratory frame, θ the photon emission angle with respect to the mean velocity of particle $\mathbf{V}$, α the number of harmonics and $\mathbf{n} = \mathbf{k}/\omega$ where $\mathbf{k}$ is the photon wave vector. When transversal motion in the comoving plane increases velocity and becomes relativistic, higher harmonic are needed in order to define its trajectory. Monochromaticity is gradually lost and the emission becomes nearly continuous (CASE2). Relevant case for our studies is the assumption that the transverse momentum is much smaller than particle longitudinal one ($|\mathbf{v}_\perp| \ll v$). Frequency of radiation in laboratory reference frame thus becomes:

$$\omega \approx \frac{2\gamma^2\omega_0\alpha}{1+\gamma^2\theta^2+\rho/2}, \tag{3.2}$$

where ρ is the parameter which characterize the multipolarity of radiation[2]:

$$\rho = 2\gamma^2\langle(\Delta\mathbf{v})^2\rangle \tag{3.3}$$

where $\langle(\Delta\mathbf{v})^2\rangle = \langle\mathbf{v}^2\rangle - \langle\mathbf{v}\rangle^2$ is equal to the mean square fluctuation of the transverse velocity of the particle $\bar{v_\perp}^2$ and it is of the order of the deflection angle squared ($\sim \Delta\theta^2$) on particle trajectory. Indeed ρ is efficiently parametrize oscillation of motion and relativistic condition of transverse velocity, and its easy to observe how equation 3.2 returns to 3.1 in case of very small oscillations. A useful definition of the radiation regime can be thus organized by ρ value.

- $\rho \ll 1$ the radiation features a **dipole-like** nature, lower frequency but much more monochromatic

- $\rho \sim 1$ an important contribution is given by high harmonics

- $\rho \gg 1$, mainly high harmonics are emitted and the radiation becomes **synchrotron-like**

[2] $\langle\ ...\rangle$ denotes averaging over time.

As stated before, in the latter limit the radiation is formed over a short section of the particle trajectory, l, during the short time $1/|\dot{\mathbf{v}}|\gamma$. If one takes into account the Doppler effect, the characteristic frequency of the radiation is $\omega \sim |\dot{\mathbf{v}}|\gamma^3$ which is typical of synchrotron radiation.

The two limit cases seen above about the type of radiation emitted by a charged particle in a quasi-periodical motion are relevant to the description of interaction with a crystalline medium. For channeled particles, the magnitude of the oscillation (hence the transverse velocity variation) strongly depends on the angle of incidence in the lattice. This angle cannot be larger than the critical angle θ_c, otherwise over-barrier motion would take place. It is useful now to define a new angle, related to potential well depth and particle rest mass in order to classify the radiation regimes in a crystal.

$$\theta_v \equiv \frac{U_0}{mc^2} \tag{3.4}$$

U_0 and m being the potential well depth and electron mass, respectively. The value θ_v is independent from the electron/positron energy. The threshold for non-dipole regime coincides with the condition $\theta_v = \theta_c = \theta_\gamma$, and therefore with a particle energy $E = m^2c^4/U_0$.

For a given θ_0, the type of radiation process depends strongly on the particle energy ε. Four regions of interest can be identified. The following description take in account the energy range valid for electrons and positrons, since their light mass favours radiation losses with respect to heavier particles. For heavier particles radiation is much suppressed at the energy currently achievable in accelerators. As stated in Chapter 2, at very-low energies (up to several MeV in the axial case and up to tens of MeV in the planar case in Si) the number of energy levels inside U_0 is limited and the particle motion cannot be described by classical mechanics. Radiation emission is better explained as transition of the channeled particles between quantum levels of the potential well. In the hundreds MeV energy range, $\theta_v \ll \theta_c \ll \theta_\gamma$. The e.m. radiation is of dipole nature ($\rho \ll 1$) for any incidence angle θ_0. For over-barrier particles ($\theta_0 \gg \theta_c$), the coherent bremsstrahlung (CB) theory can be used. The CB theory is based on the Born approximation to the potential of a crystal and it is applicable in condition of emission of dipole radiation and in the validity of the rectilinear trajectory approximation. As shown in [107], the first Born approximation cannot be used in the case $\theta_0 \sim \theta_c$. At higher beam energies, the relation between the characteristics angles becomes $\theta_v \sim \theta_c \sim \theta_\gamma$. In this case the radiation process is everywhere of dipole nature, except in the case of channeling with $\theta_0 < \theta_c$. The channeling radiation (CR) starts to become non-dipole-like ($\rho \sim 1$) at $\varepsilon > 5GeV$ ($\varepsilon > 1GeV$) in the fields of strongest

Si planes (axes). At very-high energy, $\theta_v \gg \theta_c \gg \theta_\gamma$. As a consequence, for channeled particles $\theta_0 \ll \theta_v$ the synchrotron-like radiation applies ($\rho \gg 1$), while the CB theory can be used in the opposite case for which $\theta_0 \gg \theta_v$ and $\rho \ll 1$. The intermediate case $\theta_0 \sim \theta_v$ implies that $\rho \sim 1$ and the dipole emission condition is no longer obeyed. In this range of energies ($\varepsilon \simeq 100GeV$), hard photon ($\hbar\omega \sim E$) emission becomes possible and, therefore, it is necessary to take into account the quantum recoil in the process of radiation emission. Here follows a more precise discussion of channeling radiation and over-barrier radiation at low angle approximation (CB), with a final remark on the strong field regime for $\gamma \leq 10^{4-5}$.

Fig. 3.1 represents some typical $e^{\pm}$ trajectories for different incidence angles with respect to crystal planes:

- **1**: high above-barrier motion with $\theta_0 \gg \theta_c$, which implies the possibility to use the rectilinear trajectory approximation and so the CB theory;
- **2**: low above-barrier motion with $\theta_0 \sim \theta_c$ and transverse energy, E_T, larger than U_0.
- **3**: channeling motion with $\theta_0 \sim \theta_c$ and $E_T < U_0$

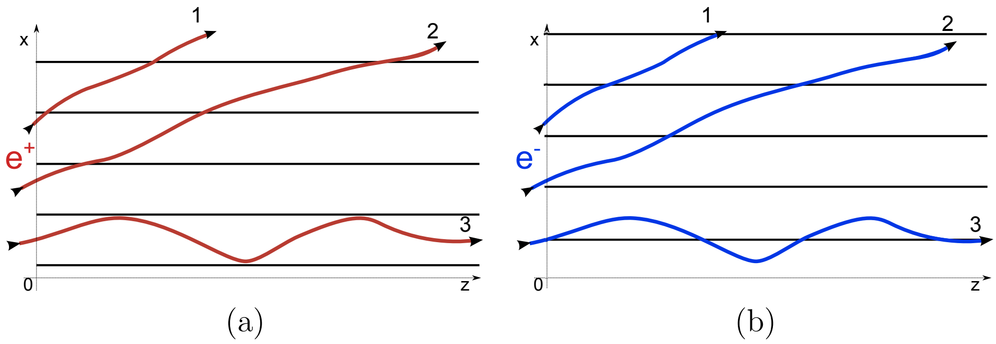

Figure 3.1: Typical positrons (a) and electrons (b) trajectories for different incident angles with respect to the planes: **1** $\theta_0 \gg \theta_c$; **2** $\theta_0 \sim \theta_c$ and $E_T > U_0$; **3** $\theta_0 \sim \theta_c$ and $E_T < U_0$.

3.2 Coherent Bremsstrahlung

In this section, a brief introduction of the concept of coherent bremsstrahlung is given following the work of Ter-Mikaelian[3]. Bremsstrahlung is the process of electromagnetic radiation emission by a charged particle when it is decelerated by the field of another charged particle, typically an electron in the field of an atomic nucleus. In the process

[3]In this section we use the units: $\hbar = 1$

of bremsstrahlung, a photon with energy $\omega = \varepsilon - \varepsilon'$, ε and ε't being the initial and final energies of the particle, is emitted in a direction $\mathbf{n}$, while a momentum $\mathbf{q} = \mathbf{p} - \mathbf{p}' - \frac{\omega}{c}\mathbf{n}$, $\mathbf{p}$ and $\mathbf{p}'$ being the initial and final particle momenta, is transferred to the medium. The minimal value of transferred momentum along the direction of motion of the primary particle, $q_{\parallel}$, is equal to δ, which is defined as

$$\delta = \frac{\omega mc^2}{2\varepsilon\varepsilon'} mc. \tag{3.5}$$

It is clear from eq. 3.5 that the value $1/\delta$ is dimensionally a distance. Indeed, such length describes the region of space along which bremsstrahlung takes place:

$$l_c = \frac{1}{\delta} = \frac{2\varepsilon\varepsilon'}{\omega mc^2}\frac{1}{mc}, \tag{3.6}$$

where m is the mass of the particle.

For soft photon emission ($\omega \ll \varepsilon$) at ultrarelativistic energies, eq. 3.6 becomes

$$l_c = \frac{2\varepsilon^2}{\omega mc^2}\frac{1}{mc} \simeq \frac{c}{\omega(1 - v/c)}, \tag{3.7}$$

l_c is called coherence length and it was introduced for the first time by Ter-Mikaelian. As charged particles momentum increases the emission of soft photon (lower energy) is characterized by longer coherence length increases. This effects at high energy becomes so evident that photon emission can't be approximated to a point-like event. A classical interpretation consider that as the charged particles emits e.m. waves along its trajectory, radiation emitted within a coherence length is in phase $\Delta\phi < 1$ (hence coherence attribute)[107].

$$\Delta\phi = \omega l_c/v - kl_c = 1, \tag{3.8}$$

where ω and k are the frequency and the wave vector of the emitted wave. From eq. 3.8, we found for ultrarelativistic energies:

$$l_c = 2c\gamma^2/\omega, \tag{3.9}$$

which coincides with eq. 3.7 introduced before and defines the order of magnitude of the space region along the particle momentum within which interference effects manifest themselves. The region of interference can be reduced from l_c total length as trajectory diverge from a rectilinear path[108]. This effect can be caused inside a medium by multiple scattering, leading to suppressions effects in the emitted bremsstrahlung radiation. If a periodic pattern is present within l_c length, interference phenomena may take place. Crystal offer the most compact periodic structures in nature, with lattice constant d of the order of few angstroms ($10^{-10}m$). l_c of ultrarelativistic particles can be order of magnitude larger than d (i.e. GeV electrons for MeV radiation have $l_c \approx \mu m = 10^4 \mathring{A}$), thus lattice periodicity can induce interference during radiation emission.

Interference effects in the bremsstrahlung of electrons/positrons crossing the periodic structure of a crystal appeared for the first time during the 1950s in the works of Ferretti [5], Ter-Mikaelian [6], Dyson and Uberall [7]. Such effect took the name *coherent bremsstrahlung* (CB), to be distinguished from the ordinary bremsstrahlung in an amorphous medium described by Bethe and Heitler (BH) [4]. CB was experimentally proven true by Diambrini-Palazzi et al. at Frascati in 1960.

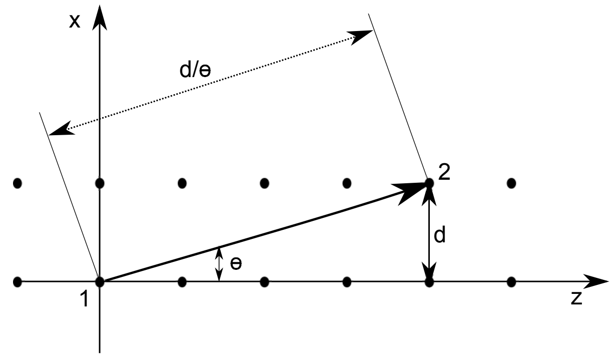

Figure 3.2: Illustration of the classical interpretation of interference processes in crystal [6].

The bremsstrahlung differential cross section in matter can be approximated in the "complete screening case" as:

$$\frac{d\sigma_{BH}}{d\omega} = \frac{16}{3} Z^2 \alpha r_e^2 \frac{1}{\omega} \left[(1 - y + \frac{3}{4} y^2) ln(183 Z^{-1/3}) + \frac{1}{12} \right], \tag{3.10}$$

where $y = \omega/\varepsilon$ is the fraction of the electron energy transferred to the radiated photon, $r_e = e^2/mc^2$ and Z are the classical electron radius and the atomic number, respectively. For rough estimation, eq. 3.10 can be rewritten in a simpler way as [61]:

$$\frac{d\sigma_{BH}}{d\omega} \approx \frac{A}{X_0 N_A \omega} (\frac{4}{3} - \frac{4}{3} y + y^2), \tag{3.11}$$

where $A(g/mol)$ and N_A are the molar mass and the Avogadro numbers, respectively,

[4]The quantum theory of bremsstrahlung has been developed by Bethe and Heitler [8]

and $X_0(g/cm^2)$ is the radiation length. X_0 is an intrinsic characteristic of a material, it indicates the stopping power of a material as the mean distance over which a high-energy electron loses all but $1/e$ of its energy by bremsstrahlung.

Interference phenomena in bremsstrahlung radiation can be interpreted with a classical approach (in this case $\omega \ll \varepsilon$ must be always valid). Let us consider a crystal with lattice constant d. If an $e^{\pm}$ impinges onto a crystal with velocity v and with a small angle θ with respect to an axis (or a plane) (see Fig. 3.2). Given a small impinging angle θ, the trajectory will cross atomic planes (or axes) with period $P \approx d/\theta$. Constructive interference condition can be easily calculated as

$$p\omega\left(\frac{1}{v}-\frac{1}{c}\right) = 2\pi n \tag{3.12}$$

which can be rearranged as

$$\delta = \frac{2\pi n}{p} = \frac{2\pi}{d} n\theta \tag{3.13}$$

where δ is the previously observed minimum transferred momentum from particle to photon where δ, as before, denotes a minimal parallel momentum transferred, $q_{\parallel}$. So larger angle (and thus shorter interference period) induce constructive interference for harder photons.

The electron/positron radiation differential cross section for CB can be represented as a sum of coherent and incoherent radiation [6, 107]:

$$d\sigma = d\sigma_{inc} + d\sigma_{coh}, \tag{3.14}$$

where $d\sigma_{inc}$ the incoherent cross section, simply defined as the sum of Bethe-Heitler atomic cross sections (N being the number of atoms) and a term $d\sigma_1$ related to crystalline structure (thus not appears in amorphous media).

$$d\sigma_{inc} = Nd\sigma_{BH} + d\sigma_1, \tag{3.15}$$

The term $d\sigma_1$ is of great interest, as it defines the reduction of incoherent scattering induced by the presence of the ordered lattice structure.[6]

$$d\sigma_1 = -Nd\sigma_{BH}e^{-\mathbf{q}^2u_T^2}, \tag{3.16}$$

From the equation is clear how, in the limit of null thermal vibration ($u_t = 0$), the total incoherent cross section 3.15 would be totally suppressed. In realistic situations, cryogenic temperature would lead to a decrease of incoherent bremsstrahlung of 5-25% (depending on temperature and material) . Coherent cross section is defined as:

$$d\sigma_{coh} = \frac{2e^2\delta}{m^2\Delta}\frac{d\omega}{\omega}\frac{\varepsilon'}{\varepsilon}\sum_{\mathbf{q}}|G(\mathbf{q})|^2\frac{\mathbf{q}_\perp^2}{q_\parallel^2}\left[1+\frac{\omega^2}{2\varepsilon\varepsilon'}-2\frac{\delta}{q_\parallel}\left(1-\frac{\delta}{q_\parallel}\right)\right]e^{-\mathbf{q}^2u_T^2}\times\theta_{hs}\left(\left|q_\parallel\right|-\delta\right) \tag{3.17}$$

where Δ is the volume of the unit cell, u_T the RMS of thermal vibrations and $G(\mathbf{q})$ is the Fourier component of the crystal potential defined as [58]:

$$U(\mathbf{r}) \equiv \sum_{\mathbf{q}} G(\mathbf{q})e^{-i\mathbf{qr}} \tag{3.18}$$

where the sum is over the reciprocal lattice vectors $\mathbf{q} = 2\pi(n_1, n_2, n_3)/d$, d being the lattice constant. $q_\parallel = \mathbf{qv_0}$ and $\mathbf{q}_\perp = \mathbf{q} - \mathbf{v_0}(\mathbf{qv_0})$ are the parallel and the transverse transferred momenta, respectively, while $\mathbf{v_0}$ is the initial velocity of the relativistic particle. The Heaviside step function $\theta_{hs}\left(\left|q_\parallel\right|-\delta\right)$ denotes the edge of the peak and the region of $\left|q_\parallel\right| \geq \delta$. As a consequence, peaks of constructive interference appear in the radiation spectrum when this condition is fulfilled.

In Fig. 3.3 is shown the intensity of CB radiation of 1 GeV electrons passing in a diamond crystal near plane (001) at angle of 4.6 mrad relative to the <110> axis for the Frascati results[9], where sharp peaks can be noticed.

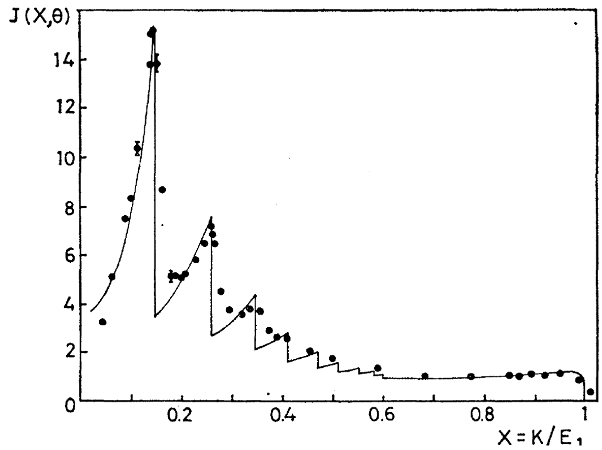

Figure 3.3: Bremsstrahlung intensity for 1 GeV electrons passing in a diamond crystal near plane (001) at angle of 4.6 mrad relative to the <110> axis for the Frascati results.[9]

3.3 Channeling Radiation

The channeling of electrons and positrons may be accompanied by an intense radiation (CR). The features of this kind of radiation have been predicted by Kumakhov [70] in the mid-70s. The oscillatory motion of a planar channeled particle stimulates radiation emission, especially for light mass particles. In low energy condition radiation emission is described as leap from discrete quantum energy levels in the potential well. Although the energy difference is typically of the order of eV, in the laboratory reference frame the actual energy is much larger given the energy boost by Doppler effect (as stated in eq. 3.1). CR photon can reach MeV or GeV energy, depending on the momentum of the channeled particles. For larger momentum instead radiation loose dipole nature and becomes synchrotron-like.

For instance, if we consider as approximation the motion of channeled positrons in the harmonic interplanar potential $U = U_0(2x/d_p)^2$, the frequency of motion results to be:

$$\omega_0 = \frac{2}{d_p}\sqrt{\frac{2U_0}{m\gamma}}, \tag{3.19}$$

m being the positron mass. In the dipole limit, the emitted radiation frequency is shifted by the Doppler effect:

$$\omega = \frac{\omega_0}{1 - v/c\cos\theta}. \tag{3.20}$$

In the ultrarelativistic limit ($\gamma \gg 1$), the radiation frequency emitted in the forward direction ($\theta = 0$) becomes (see eq. 3.2):

$$\omega \approx 2\gamma^2\omega_0 = \frac{4}{d_p}\sqrt{\frac{2U_0}{m}}\gamma^{3/2}. \tag{3.21}$$

Even if the motion of a channeled electron/positron resembles the one a in magnetic undulator, to calculate the emitted radiation one must average on the contribution of all possible trajectories. The form of each trajectory is dependent on the transverse impact parameter with respect to the planar potential for a given angle of incidence θ_0. Moreover, a significant difference between particles of opposite charges comes into play for CR. In the planar channeling mode, positrons move in an inter-planar potential well, while electrons move around a plane. The particles that pass closer to planes feel a stronger electric field during their motion and so generate more intense radiation. Most of the intense radiation for planar channeled positrons is due to particles with high-amplitudes of oscillations, while for electrons is due to particles with small amplitude with respect to plane [16].

3.4 Strong field regime

A general way to deal with the radiation emitted by ultrarelativistic particles in crystals is based on the usage of the general quasiclassical operators method proposed by Baier and Katkov (BK) in 1967-1968 [58]. Because the BK formalism takes into account real trajectories, it can be readily applied to study radiation generation also in deformed crystals, e.g., bent and periodically bent crystals. This general method is necessary because while the motion of ultrarelativistic charged particles in crystals can be well described by classical mechanics due to the high number of quantum states in the transverse potential well, for sufficiently high-energies this approximation does not hold true for the process of radiation emission as well. In fact, it may happen that the emitted photon energy ($\hbar\omega$) becomes of the order of particle energy ε. In such a case, one should consider the quantum recoil in the process of photon emission. Following QED results, such situation is expected to become more and more relevant as charged particles are subjected to external fields of the order of Schwinger critical fields.

$$E_0 = m^2c^3/e\hbar \simeq 1.3 \times 10^{16} V/cm, H_0 \simeq 4.4 \times 10^9 T. \tag{3.22}$$

Such intense fields values activate non-linear QED effects such as pair creation from vacuum. These extremes values are reached rarely in physical system such as in pulsar atmosphere or recently in near collision ion beams at LHC. Indeed, the continuous potential of a crystal is of the order of $10^{10} - 10^{11}$ V/cm, which is much smaller than the critical field. Nevertheless, if the particle is ultrarelativistic with $\gamma > 10^5$, in the rest-frame the particle feels a Lorentz-boosted field comparable to the critical field, E_0 [109]. In such a case, the classical description of the process of radiation emission is no more valid.

In 1967-1968, Baier and Katkov (BK) proposed the usage of a *quasiclassical operator method* to solve the QED problem of emission of radiation by a charged particles in an external fields [110, 111]. In the QED description of this kind of processes, two types of quantum effects, i.e., the quantization of particle motion and the quantum recoil of the primary particle in the γ-quantum emission, are taken into account. The BK method is based on the fact that for the case of ultrarelativistic particles the motion can be consider classically, while the quantum recoil may not be negligible.

With the usage of the BK quasiclassical method, a QED problem is then reduced to the problem of solving the classical equations of motion of a charged particle in an external field and then calculating some integrals along the classical trajectory. This method has the advantage to be applicable in the whole photon energy range, except for the extreme limit where $\hbar\omega \cong \varepsilon$. The radiated energy, written in BK quasiclassical formalism [58] (in $c = \hbar = 1$ natural system of units) is:

$$\frac{dE}{d^3k} = \omega \frac{dN}{d\omega d\Omega} = \frac{\alpha}{4\pi^2} \int\int dt_1 dt_2 \overline{N}_{21} \exp\left[ik'(x_1 - x_2)\right], \tag{3.23}$$

where $dN(\omega)$ is the photon emission probability, Ω the solid angle of photon emission, $\alpha = 1/137$ is the fine structure constant, $k = (\omega, \mathbf{k})$ is the 4-momentum of the photon radiated with energy ω and 3-momentum $\mathbf{k}$, $k' = \varepsilon k/\varepsilon'$, where ε and $\varepsilon' = \varepsilon - \omega$ are, respectively, the particle energy before and after the photon emission, $x_{1,2} = (t_{1,2}, \mathbf{r}(t_{1,2}))$ and $\mathbf{v}(t_{1,2})$ are the particle coordinate 4-vector and 3-velocity at instants of time t_1 and t_2. The integrals in eq.3.23 are taken along the whole particle trajectory and

$$N_{21} = \frac{1}{2} \sum_{\mathbf{e},\zeta_i,\zeta_f} N_{21}(\mathbf{e}, \zeta_i, \zeta_f) = \left[(\varepsilon^2 + \varepsilon'^2)(\mathbf{v}_1 - \mathbf{n})(\mathbf{v}_2 - \mathbf{n}) + \omega^2/\gamma^2\right]/2\varepsilon'^2, \tag{3.24}$$

is the radiation polarization matrix averaged over the initial particle polarization ζ_i and summed over the final particle ζ_f and photon $\mathbf{e}$ ones, where $\mathbf{n}$ is the photon direction.

The main difference with the general classical equation for radiation emission in an external field (see eq. 1.23 of [58]) is the substitution of $\omega \to \omega' = \varepsilon\omega/(\varepsilon - \omega)$. In the limit of $\omega \ll \varepsilon$, these two expressions coincide and the radiation can be treated in the classical framework.

Compact directional calorimeter

The strong field condition is more easily reached for axial fields of dense material containing elements with large atomic number Z. Beside pure elemental crystals made of Tungsten or Iridium, such condition is often met for inorganic scintillators. Indeed, in high energy physics such materials have been an invaluable resource for particle detection and measurements of total energy. On the contrary of plastic scintillator, inorganic ones are characterized by single crystal structure. The described orientational effects may indeed take place in these crystals as well. Previously, it was stated as in strong field condition particles lose quickly a non-negligible part of the momentum into radiation, thus quantum recoil had to be taken into account in the photon emission calculations. As a direct consequence of this phenomenon, the electromagnetic shower develops much faster than in any regular medium. Moreover, since the effect is enhanced as projectile γ increases, the shower total length remains almost constant (instead of increasing).[112] An e.m. calorimeter composed by carefully aligned crystal scintillators would contain ultrarelativistic particles in a much compact length. This would be a great advantage in the study of forward particles in high energy physics experiments, where angular divergence is mostly contained and known. In particular, beam dump experiments would benefit from the enhanced stopping power of this new type of calorimeter to separate e.m. interacting particles from dark matter candidates. Another suitable application would be the employment of this technology in astrophysics airborne experiments. Indeed, the cosmic rays reach energies unattainable by accelerators up to $10^{19} eV$. Airborne experiments such as Fermi LAT, PAMELA, CALET, AMS and DAMPE face strong limits on the maximum measurable energy, as total mass of the calorimeter is limited by satellite size and launch costs. Indeed, a brute force approach by size increase is not a viable solution, thus almost fixed e.m. shower length achieved by oriented crystal can provide a feasible solution to the issue.

Chapter 4

LHC crystal collimation

The Large Hadron Collider represent the frontier of high energy physics research. The record momentum reached by the beam particles makes it a one of a kind machine. A very important feature for its proper working is the presence of an efficient collimation set-up. Indeed, in a circular collider, it is impossible to avoid the formation of an halo of particles beside the main beam. Such particles can diverge from the desired trajectory for several causes like aberration of electromagnetic optics, scattering with the residual gas on the pipeline. These effects cannot be completely cancelled, but the presence of uncontrolled particles poses a serious threat for the operation and performances of the machine. One of the most delicate issue is the radioprotection of super magnet dipoles. In LHC a large amount of energy is stored in the beam (350 MJ in normal operation, doubled in high luminosity set-up) but a very small portion of energy ($15 - 50\ mJ/cm^3$) can heat-up the super magnet enough to provoke phase transition from super conduction. This situation is called "quenching" and can potentially lead to violent reactions and consequent destruction of the magnet and damage its surrounding environment. Beside this worst-case scenario, halo particles can induce unwanted noise and hamper the sensitivity of the experiment. Being mostly parallel to the beam, they can cross several detector cells along the beam direction. This obstruct data taking operations, creating more signals per particles than background particles from beam interaction. The LHC high-luminosity goal to enhance luminosity tenfold exploits several approaches, one being the increase of beam intensity. Hence collimation remains a very sensitive issue.

4.1 LHC collimation setup

LHC beams are being collimated in two dedicated sites along the ring (IR3, IR7). Most interaction with beam takes place in IR7, where *betatron cleaning* takes place, i.e. particles whose trajectory was distorted and features transversal oscillation with larger amplitude are separated from the beam. Stopping ultrarelativistic protons and ions circulating in beam halo is a challenging task, given the large amount of momentum to be dissipated. Current setup exploit several stages to deflect beam halo away from the beam orbit an subsequently intercept it with absorbers and other collimator (fig.4.1a). The first two stages of collimation are the closest to main beam and thus intercept more particles. Both are made of carbon fiber composite, in order to reduce energy deposition in the medium and preserve its structure. Only a small fraction of particles are stopped in the primary collimator, most deposit part of their energy and are scattered into a *secondary halo*. Hadronic shower is also developed inside the collimator, thus also secondary particles are added into the secondary halo. This secondary halo is then intercepted by the second collimator, which acts in a similar manner by stopping some particles and creating a *secondary halo*. Being the tertiary halo less intense than the previous two, it is possible to deposit all energy in a solid medium without damaging it. The absorber, placed far away from the beam orbit ($\gtrsim 14\sigma$), is made of a tungsten alloy and almost completely the particles. Downstream and close to the experiments is placed a tertiary collimator, made in tungsten as well, devised in order to protect magnets from the last particles escaped from the previous stages. Collimation inefficiency η_c is the quantity used to indicate the portion of background particles surviving collimation, being the final goal to reduce it as much as possible. During operation with 6.5 TeV proton the value is of the order $\eta_c \approx 10^{-15}$ after . Collimation of ion beam is more challenging than for proton beam, although the energy stored in the beam is much lower (up to 13.3 MJ vs 350 MJ). Complications arises due to nuclei fragmentation and electromagnetic dissociation in collimators. During 2018 operations, although quenching was avoided, 7 out of 48 $^{208}Pb^{82+}$ fills were dumped because of high losses in IR7.[113].

4.2 Crystal collimator parameters

In crystal assisted collimation the beam halo is deflected from the beam not by multiple scattering but by channeling in a single bent crystal. In this setup, a bent crystal is mounted on an high precision goniometer with sub-micro radian precision, in order to align lattice planes with the incoming particles within the critical channeling angle. The channeled proton crosses the medium undergoing strongly suppressed energy loss in comparison with a misaligned crystal or amorphous material, but significantly modify their trajectory following lattice planes curvature. Thus, the beam halo is not randomly scattered but is accurately deflected by a precise angle in a much more controlled manner. Far from the beam orbit an absorber stops and contain the deflected particles. and an heavy collimator contains the last remaining particles escaping the absorber. (fig.4.1b)

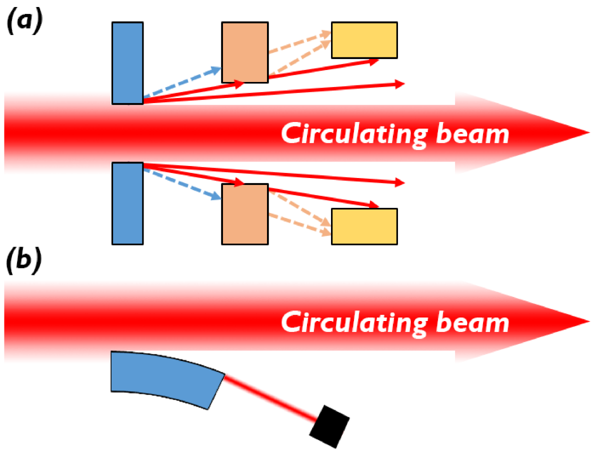

Figure 4.1: (a) Classical approach for collimation of circulating beams in a particle accelerator is based on a chain of bulky materials placed at different apertures along the beam path. Interaction between the *primary halo* and a first block of material (blue box) leads to partial absorption of the halo and, as a by-product of the interaction, to a spray of particles (*secondary halo*) composed of primary halo's particles (red arrows) which are not stopped and hadronic showers generated in single or double diffractive events (dashed arrows). The secondary halo is partially absorbed by a second block, which plays for the secondary halo the same role of first block for the primary halo. (b) Collimation based on a bent crystal as primary collimator. A bent crystal (blue) is aligned to the primary halo beam and channels its particles between the crystal's atomic planes. Channeled particles are efficiently deflected to a massive absorber (black). Given the nature of interaction between the crystal and the beam, the rate of inelastic interactions is strongly suppressed. The elements depicted in this figure have sizes that are not to scale.

This approach benefits from the reduction of material placed near the beam in the first stages of collimation. Indeed, the most delicate part of the collimation process concerns the primary (and secondary) collimators, as they are the nearest to the primary beam and suffer the most intense flux of particles. Whereas collimators are $\approx 1\ m$ long, only few millimetres of medium are required in this configuration. Moreover, channeling reduce nuclear interaction between beam and atoms, as particles are confined between lattice planes. Channeled protons slightly approach nuclei only twice every channeling oscillation which at LHC energy range are of the order of tens and hundreds of microns ($56\mu m$ 400 GeV and $235\mu m$ at 6.5 TeV). The contribution to hadronic shower is primary limited to non-channeled particles.

Clearly, steered particles do not suffer inelastic interaction with the crystal, which acts as a smart element for particle beam steering. Table 4.2 summarize the most challenging or relevant specifications that a crystal must satisfy for installation in the LHC

Material	Silicon
Dislocation Density	$< 1/cm^2$
Channeling Plane	(110)
Miscut *	$< 10\mu rad$
Weight	$< 150g$
Length	$4 \pm 0.1\ mm$
Steering angle	$50 \pm 2.5\ \mu rad$
Torsion	$< 1\ \mu rad/mm$

Table 4.1: list of features required for bent crystal collimator of LHC. *The *reference plane deviation* is hereafter expressed as *miscut*, as this term is widely diffused in relativistic particles channeling scientific papers

Silicon was selected as the material given its high lattice perfection and availability in large ingots and wafers. Germanium also is produced with required quality and sizes, but it is heavier element with half nuclear interaction length and thus has larger probability to develop hadronic showers. The channeling plane was chosen based on the depth and width of the potential well. The (110) plane has a total height of $\approx 16eV$ and width of $1.92\mathring{A}$ is the best solution. The angle between lattice planes and the crystal surface is defined as *reference plane deviation* by the official international standards [31]. Hereafter the term *miscut* will be employed given its large diffusion in scientific papers in the field of relativistic particle channeling. This parameter can affect channeling performance in two different manner. In case of *negative miscut* angle lattice planes intercept surface before the end of the crystal, thus particles channeled in such planes would exit the crystal early before acquiring the desired angular deflection. This effect is avoided for *positive miscut*, where misalignment has opposite sign. In both cases, simulation shows a fivefold increase of nuclear reaction rate [114]. Indeed, positive miscut would lead to an unwanted increase of the impact parameter of particles on the samples, as show in fig. 4.2. Although the optimal condition would be a perfect correspondence between atomic plane and crystal surface, such requirement cannot be achieved in a real sample. The miscut should be at least much smaller than the steering angle of the crystal. For LHC beam, a suitable value of positive miscut was estimated to be lower than $10\mu rad$. A low miscut value has also the positive consequence of improving optical pre-alignment of samples once installed in the beam-pipe.

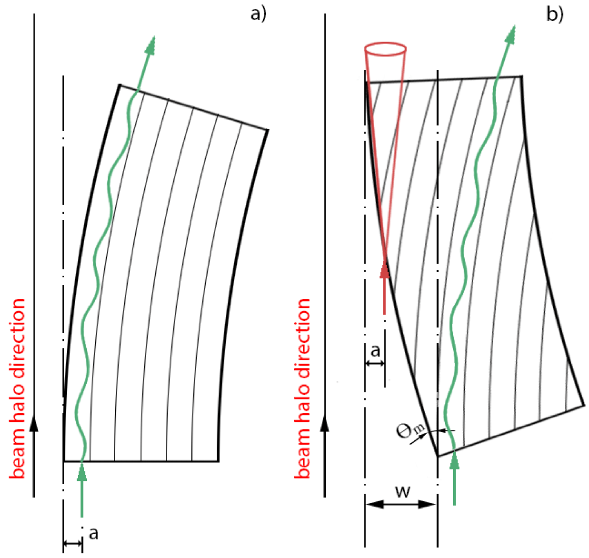

Figure 4.2: (a) sketch of bent crystal with zero-miscut angle aligned to the halo of a beam circulating in a particle accelerator. Particles (green arrow and trajectory) are captured in channeling regime independently of their impact parameter to the crystal, a. (b) As an angle of miscut, Θ_m, is introduced, a correlation between impact parameter and crystal-beam orientation is established. Only particles with sufficiently large impact parameter, w are captured under channeling regime and steered. Particles with lower impact parameter (red arrow) interact with the crystal as if it is an amorphous target, particles are deflected through multiple scattering (red cone).

In order to achieve and maintain alignment between beam and crystal a goniometer with $0.1\mu rad$ resolution is employed. The weight of the assembly is thus limited to 150 g by the goniometer maximum load. The goal of minimizing the crystal length in order to reduce inelastic nuclear reaction in the crystal was balanced by the need of a large bending radius to achieve large channeling efficiency[45]. The optimal value obtained was $50\mu rad$ of deflection and length of 4 mm. The value was calculated taking into account successive iteration of the same particle with the crystal during each accelerator laps (*multipass*), which increase actual efficiency up to > 95[115]. Torsion is an unwanted deformation parameter in the crystal bending, which induces a tilt of lattice plane along direction transverse to the beam propagation (fig. 4.3). Such effect would reduce the size of crystal simultaneously in alignment with the beam, possibly preventing channeling of the whole beam halo and increasing risk of losing alignment with the beam. Thus, torsion should be limited in order to have small misalignment wrt critical angle over the size of the beam.

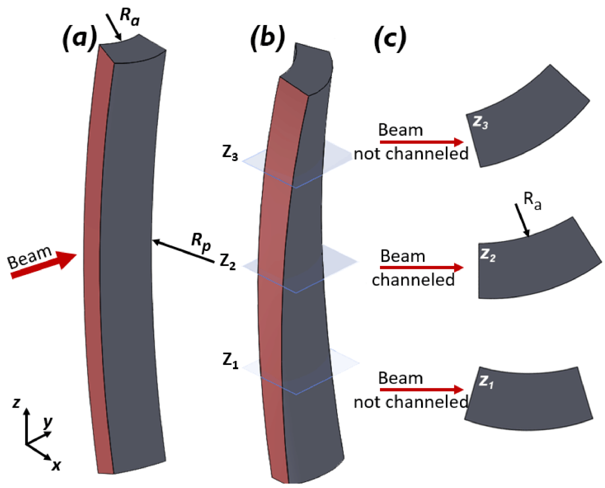

Figure 4.3: (a) Representation of a bent silicon strip crystal. A couple of moment are applied at end of the crystal, resulting in a "primary" bending of the crystal, with radius R_p, and a "anticlastic deformation" of crystal cross section, manifesting with a curvature of radius R_a. (b) As consequence of mechanical imperfections of the holder or of the mounting procedures, the bent crystal might be subject to torsion. (c) Cross sections of a strip crystal bend and subject to torsion, taken at three different positions. As result of torsion, alignment between crystal cross section and the beam linearly changes along the vertical direction of the crystal, reducing its geometrical acceptance

4.3 Crystal fabrication

Miscut measure and reduction Crystal samples are cut from a silicon wafer. Semiconductor standard provides miscut within 0.1° ($\approx$ 1745 μrad), specially manufactured wafers can reach a maximum precision of 0.01° ($\approx$ 172 μrad). As stated previously, samples require miscut angle lower than 10 μrad, thus wafer miscut must be reduced. To accomplish this request, a precise characterization of the miscut of starting silicon wafers was done by using a high resolution X-rays diffractometer together with an autocollimator (see fig.4.4).

In more details, Bragg diffraction is an interference phenomenon between x-rays and a crystal lattice. Occurring of this effects is clear evidence of x-rays impinging on lattice plane at a well-known precise angle (*Bragg angle*). Hence it is possible to keep track of lattice plane tilt wrt x-rays by exiting diffraction. Using the precise goniometer of the X-rays diffractometer, it is possible place the wafer in diffraction condition. In case of zero

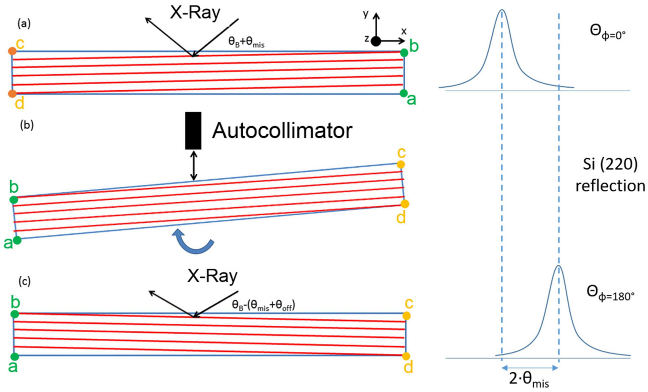

Figure 4.4: Method for miscut characterization with high resolution X-rays diffractometer and autocollimator. Mounted crystal is oriented to excite Bragg deflection (a). Crystal rotated of 180° around the y-axis. Bragg deflection is lost due both to miscut and rotational stage mechanical plays. Mechanical plays are compensated by means of the autocollimator (b). Bragg deflection is found again and miscut is determined (c)[50]

miscut, during rotation along surface normal axis diffraction condition should be preserved. Instead, misalignment between sample surface and lattice planes causes an angular shift of the diffraction angular position. After 180° rotation, the measured angular shift corresponds to double the miscut angle along that direction. This measure requires to maintain microradian level of precision during all movement of the crystal. Small mechanical plays and misalignment from diffractometer axes, otherwise negligible during limited movement, become relevant for the measure. In order to avoid such imprecisions, an optical collimator is employed. This instrument remains fixed during all operations and monitors the surface angular position during all the procedure. Whereas diffractometer and crystals rotate during the measures, the autocollimator remain fixed and thus unaffected by errors. By exploiting this reference, the miscut is being measured within the maximum accuracy of $\pm\ 0.0001° \approx 1.7\mu rad$. Once the miscut of the wafer has been measured, procedure for its reduction can be carried out. Classical polishing methods cannot reach the resolution for the required adjustment, thus novel approach was employed, i.e. Magnetorheological Finishing (MRF). MRF is a precision polishing method developed by QED Technologies (QED). It is a deterministic finishing process that has the demonstrated ability to produce optical surfaces with an accuracy better than 30 nm peak to valley (PV) and surface micro—roughness (R_A) less than 1 nm on optical glasses, single crystals (such as calcium fluoride and silicon), and glass—ceramics over areas as large as several cm^2. The MRF process is based on the use of magnetorheological fluid, whose unique property is the variation of viscosity up to several orders of magnitude induced by an external magnetic field. The fluid can be transformed from a liquid into a quasi-solid in milliseconds. In QED's use of this property, the fluid is pumped onto and around a rotating spherical wheel, with the wheel acting as a conveyor of sorts. The fluid forms a "ribbon" on the wheel, and as the ribbon passes through an area in which a local, high intensity, magnetic field has been created, its viscosity greatly increases. By introducing the surface to be polished into this high viscosity area, local, shear—based material removal can be created (see fig. 4.5). By control— ling the shape and other parameters that affect the removal, QED can create a sub—aperture polishing tool and deterministic process that has long term stability and relatively high removal rates on most optical materials. The forces acting on the surface are predominantly tangential. The normal forces on the individual abrasive particles are very small (limited to hydrostatic). This is in contrast to conventional polishing techniques where an abrasive is forced into the surface through the action of a lap (either bound or loose). Here normal forces can dominate, creating scratches, sub-surface damage, and stress.

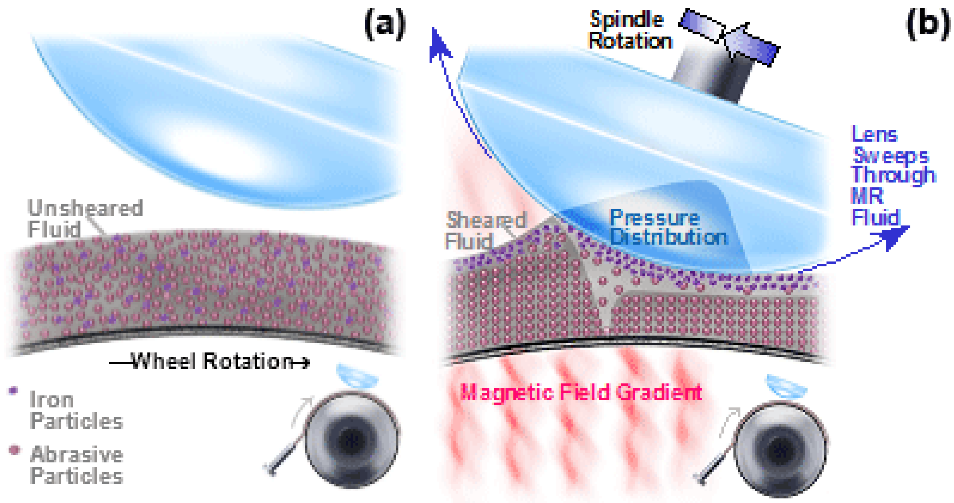

Figure 4.5: (a) Creation of MRF polishing "spot". When the magnetic field is off, there is a random distribution of iron and abrasive particles in the ribbon of fluid being transported by the rotating wheel. (b) When the magnetic field is turned on, the iron particles align and form chains giving to the fluid structure and stiffness. In addition, the water and abrasives move to the surface because the iron particles are attracted toward the wheel. When the workpiece is inserted into the fluid, the converging gap creates a highly sheared fluid layer that removes material with very low normal forces acting on the individual abrasive particles.

The process was usually carried out in a series of iterations with wafers being sent back to Ferrara for feedback on the proceeding on miscut reduction. The first MRF step focused mainly on increase of planarity in the wafer $\approx 0.4\ \mu m$ to $\approx 0.01\ \mu m$. This passage is often critical, as for non-planar surfaces miscut is obviously not constant over all the wafer and hinders both measure and reduction. Flatness and roughness of samples was checked via laser interferometry with a Zygo interferometer operating in Fizeau configuration (see Fig.4.6). Following a summary table of the processed wafers

wafer #	**initial miscut**	**miscut after I polish**	**miscut after II polish**	**miscut after III polish**	**miscut after IV polish**
wafer #1	$127 \pm 1\ \mu rad$	$98 \pm 1\ \mu rad$	$2 \pm 1\ \mu rad$		
wafer #2	$145 \pm 1\ \mu rad$	$132 \pm 1\ \mu rad$	$3 \pm 1\ \mu rad$		
wafer #3	$130 \pm 1\ \mu rad$	$130 \pm 1\ \mu rad$	$2 \pm 1\ \mu rad$		
wafer #4	$123 \pm 1\ \mu rad$	$113 \pm 1\ \mu rad$	$13 \pm 1\ \mu rad$	$6 \pm 1\ \mu rad$	$1 \pm 1\ \mu rad$
wafer #5	$50 \pm 1\ \mu rad$	$36 \pm 1\ \mu rad$	$1 \pm 1\ \mu rad$		
wafer #6	$67 \pm 1\ \mu rad$	$2 \pm 1\ \mu rad$			
wafer #7	$120 \pm 1\ \mu rad$	$117 \pm 1\ \mu rad$	$9 \pm 1\ \mu rad$	$0 \pm 1\ \mu rad$	

Table 4.2: list of the steps in miscut reduction of the wafers produced. An average of two iterations are usually needed: the first to increase wafer planarity, the second to actually reduce the miscut. Wafer #4 and #7 are dedicated to test the smallest miscut achievable by MRF technique: reduction of miscut under 10 μrad threshold has been achieved over the whole wafer, not only the direction along beam propagation

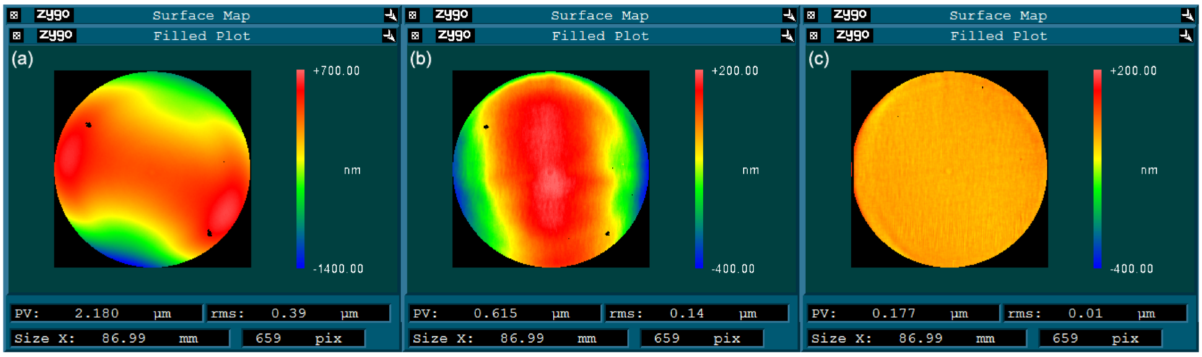

Figure 4.6: (a) interferometric characterization of wafer surface prior to polishing operations shows surface flatness of 0.39 μm. (b) After a first polishing run with a high removal rate MRF fluid surface flatness is improved to a value of 0.14 μm. (c) After a second polishing run using a low roughness fluid, surface flatness improves to 0.01 μm. Black dots in (a) and (b) are fiducials used to orient the wafer in the measuring step. [116]

The crystalline quality of the treated surface has been characterized by the following means:

- high-resolution X-ray diffraction (HR—XRD);
- micro-raman spectroscopy;
- Rutherford back scattering in channeling mode (RBS—c);
- transmission electron microscopy (TEM);

Such techniques, well established for the determination of crystalline quality, highlighted the absence of any lattice damage induced to the silicon wafer, demonstrating the possibility to apply MRF polishing to delicate substrates as silicon wafers.

X-Ray rocking curves obtained on both surfaces of the crystal parallel to the particle

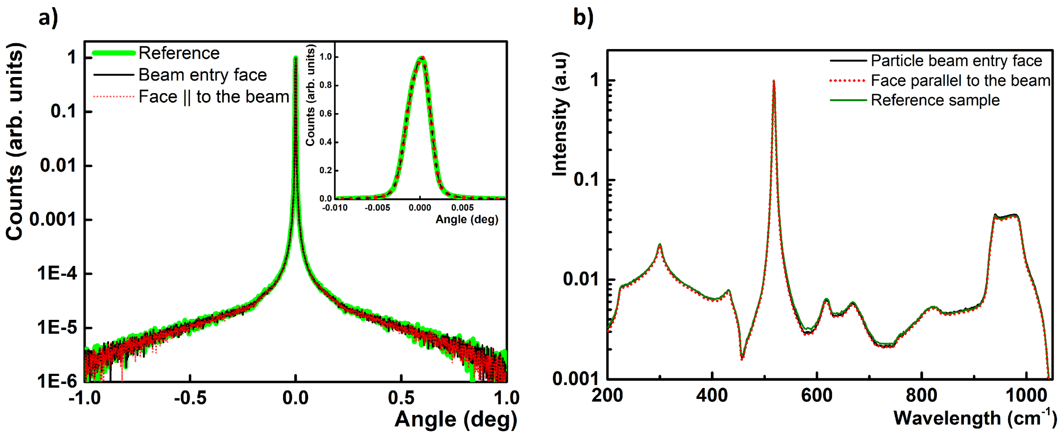

Figure 4.7: a) High resolution X-ray diffraction rocking curve on the surface of the crystal parallel to the propagation of the beam (red dashed curve), on the beam entry face (black curve) and on a reference surface (green curve). The inset shows a zoom of the rocking curves in their central region; b) micro-Raman spectra collected on crystal surface parallel to the beam (red dotted curve) and on beam entry face (black line) are compared to micro-Raman spectra recorded on a reference sample

beam and on the surface which represent the entry face for the beam, compared to the rocking curve recorded on a reference crystal. Comparison of the recorded rocking curves demonstrates an extremely high quality for both surfaces subjected to MRF and chemo-mechanical polishing: operating with a 8.04 keV X-Ray beam (Cu $K\alpha_1$). The obtained signal is averaged over $\approx$ 13 μm superficial layer of the crystal. The presence of a number of dislocations in excess with respect to the reference sample, eventually induced by surface machining would be revealed by scattering tails around the main peek induced by the dislocations deformation field. As can be noted in fig.4.7 no variation with respect to the reference is detectable.

In order to receive information from a thinner region below the surface, we used micro-Raman spectroscopy based on a 532 nm wavelength laser focused at a spot of a few microns. The chosen wavelength probes a thickness of $\approx 1.3\ \mu m$ under the crystal surfaces. Result of characterizations, reported in figure 4.7 shows absence of amorphous or strained layers and of silicon phases different from cubic diamond structures Rutherford Back-Scattering in Channeling condition (c-RBS) and Transmission Electron Microscopy (TEM) were used to get information related to the atomic ordering of the first atomic layers of both the faces of the crystal which are parallel to the beam and to the beam entry face.

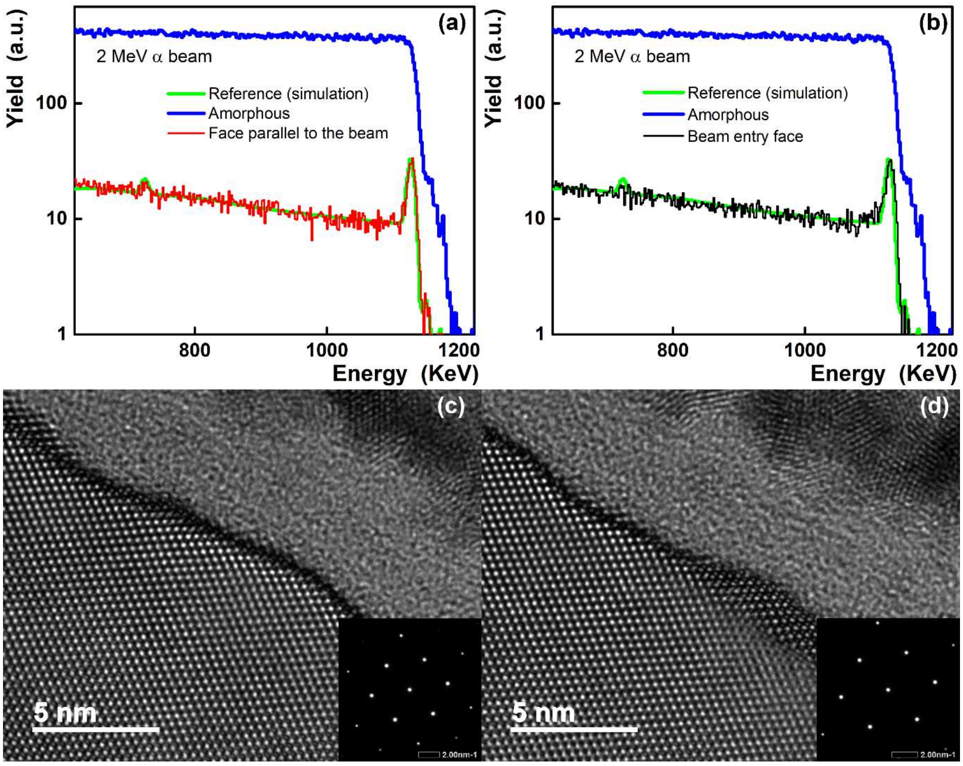

Figure 4.8: RBS-c and TEM characterizations. (a) and (b): RBS-c spectra of 2 MeV $\alpha++$ recorded on the crystal face parallel to the direction of propagation of the beam in a circular accelerator and on the face acting as entry face for the beam. (c) and (d): TEM characterizations for the same surfaces. Both surfaces results to be free from sub-surface lattice damage induced by MRF and chemical-mechanical polishing operations, respectively

c-RBS was carried out using 2.0 MeV 4He+ at scattering angle of 160° in IBM geometry. Surface χ_{min}, defined as the ratio of the RBS yield under channeling alignment and random condition extrapolated at the surface channel, is chosen as quantitative parameter. The higher the degree of crystalline order in the lattice, the lower the surface χ_{min} due to the reduction of dechanneling from the defects in the crystal. RBS-c provides information on the presence of crystalline defects up to a depth of 2 μm with nanometric resolution in the crystal depth. Both surfaces recorded a value for χ_{min}, which is compatible with the value recorded on a reference crystal with a surface free from crystallographic defects. Moreover, simulations allow to quantify the surface peak areal density of Si atoms that do not contribute to channeling. It is worth to note that even in perfect crystals the Si atomic areal density corresponding to this peak is $10^{16} atoms/cm^2$ [117, 118] under the present experimental conditions. This is due to the fact that at this energy, the beam focusing due to channeling needs to cross a certain crystal thickness before starting to decrease the backscattering yield. Mapping the crystal surface on both beam entrance and lateral faces with 4He+ spots 1×1 mm^2 gives surface peak values from 1×10^{16} to 1.4×10^{16} $atoms/cm^2$. This means that a non-crystalline surface Silicon fraction can be present as low as from 0 to 0.8 nm over the sample surfaces, reasonably in a SiO_2 nano-layer that naturally forms after air exposure. [117, 118] The high order of crystalline perfection is confirmed also by TEM characterizations, showing an ordered arrangement of atomic columns preserved up to the crystal surfaces (see figure 4.8)

Crystal Sample Geometry and Bending Since the first proposal of beam manipulation via channeling in bent crystals by Tsyganov in 1976 [119], several different bending technologies have been exploited to fabricate the crystalline deflectors. First experiments focused mainly on large deflection angles of tens of milliradians [2, 120]. The crystals were several centimetres long. Primary curvature obtained via 3-points schemes was exploited to deflect the channeled particles. Such method did not allow to obtain a uniform bending along the whole samples as usually maximum curvature occurred in the central zone. Moreover, steel pins used to deploy could induce local deformation which further compromise bending quality. New designs such as “U-shaped”[121] and “O-shaped” [122] were developed respectively at CERN and IHEP(see Fig. 4.9). These types were fabricated from a single block of silicon shaped in order to apply bending forces far from the beam trajectory, thus solving localized deformation issue and achieving greater control over the curvature. In particular, the “U-shaped” sample employed at CERN tests featured a refined surface processing process at ESRF in order to achieve high level of lattice quality and low roughness (≈3 nm) [121].

The success of the experiments based on the multi-pass configuration, induced the use of shorter crystals and smaller deflection angle in order to maximize channeling efficiency.

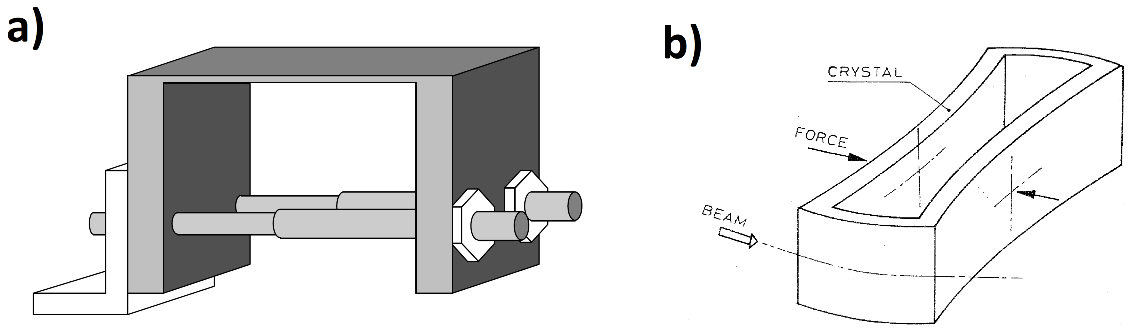

Figure 4.9: [121]Fig. a)U-shaped crystal employed at CERN for extraction of 120 GeV/c proton from SPS, channeling was exploited on (110) silicon plane along 4cm length to induce 8.5 mrad deflection with ≈10% efficiency; [122]Fig. b) Scheme of O-shape setup exploited for extraction of 70 GeV/c proton beam of U-70 accelerator, planar channeling on (110) planes along 5mm length was used to induce 1.5 mrad deflection with ≈40% efficiency

Hence secondary curvature designs were found extremely suitable for the new generation of experiments. The anticlastic curvature, studied in previous configurations as an unwanted effect, was first exploited in 2001[29]. This technology is the base for the first sample fabricated in this thesis work and will soon be thoroughly discussed. Another important design employs quasi-mosaic curvature. This secondary curvature arises for certain crystallographic orientations as result of lattice elastic anisotropy, as stated by Sumbaev in 1957[123]. This technology allowed for very compact crystal deflector and was developed shortly after the first anticlastic in 2004 in Protvino accelerator[124]. Currently crystal deflector are being developed and tested for LHC collimation by the Petersburg Nuclear Physics Institute.

As previously stated (see table 4.2), the crystal must have 4 mm thickness along the beam and 80 m of radius of curvature. In order to achieve such bending, exploitation of secondary curvatures is a suitable solution. Indeed, in specific bending schemes adjustment on primary curvature allows fine tuning of the secondary one. For LHC beam collimation, two type of curvature has been proposed: anticlastic and quasi-mosaic. The latter arises from elastic anisotropy of crystal lattice, thus occurs only for specific crystallographic orientations. Although silicon (111) planes can bend via quasi-mosaic deformation, is it impossible to achieve for the most efficient (110) planes. In this work, only anticlastic deformation had been exploited for the production of bent crystal for LHC collimation. The anticlastic curvature is not an exclusive feature of the crystals but is attainable on any type of solid, isotropic ones included. First studied of the effect are related to problems such as deformation of magnetic tapes subjected to strain. Starting from the second half of the 90s anticlastic curvature has been exploited in channeling experiments. The anticlastic deformation occurs in a strip-like sample, i.e. with length along primary curvature much larger than the other two dimensions. The longitudinal strains inducing the primary curvature by elastic reaction of the solid induce lateral strains along the width direction. As a result, the sample takes the shape of a saddle with anticlastic curvature being of opposite convexity wrt the primary one. A configuration of particular interest for the production of crystal for channeling is one which present a relatively small principal curvature imparted by two equal forces at the opposite edges of a parallelepiped sample, whose length is larger than the width and much larger than the thickness. This problem has been first addressed by De Saint-Venant in 1864 and afterwards further elaborated by Kelvin and Tate in 1879, Lamb in 1861 and finally Searle in 1908 [125]. The solution was obtained applying the semi-inverted process with the elastic theory as a homogeneous and anisotropic bar under infinitesimal deformations and small displacement.

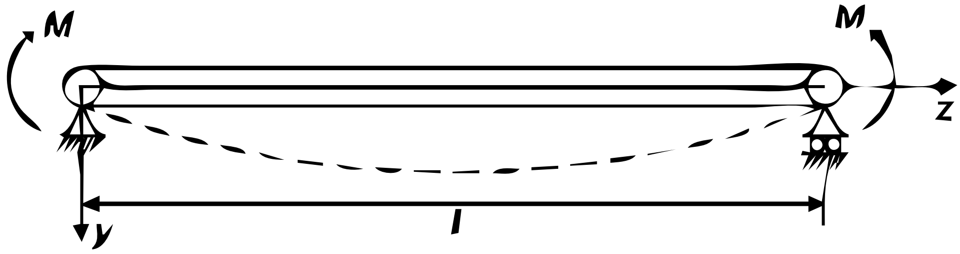

Figure 4.10: Scheme of the setup for the De Saint-Venant problem[126]

The displacement of the strip along the main dimension y is defined by the following formula ∋

$$\nu\left(x,y,z\right)=\frac{1}{2S_{33}R}\left[-S_{13}x^{2}-S_{23}y^{2}+S_{33}\left(lz-z^{2}\right)-S_{35}xz\right] \tag{4.1}$$

where ν indicates the variation of position caused by the moments M, l is the length of the crystal, R is the primary curvature radius and S_{ij} are elements of silicon compliance matrix calculated for the specific crystallographic orientation. The presence of the z^2 term pertains to the imposed principal bending, while the x^2 term shows that x-y cross section is deformed as a parabola, i.e. anticlastic deformation, whose magnitude is linearly proportional to the imposed bending. The anticlastic curvature in this system lies on the xy plane and is indicated in those two equivalent way:

$$\frac{1}{R_A} \propto \frac{d^2\nu}{dx^2} = \begin{cases} -\frac{M}{I} S_{13} \\ -\frac{1}{S_{33}R} S_{13} \end{cases} \tag{4.2}$$

Where R_A indicate the anticlastic radius of curvature. A useful parameter to quantify the extent of anticlastic deformation is the dimensionless ratio R_A/R between the secondary and the primary curvature radius.

$$\frac{R_A}{R} = -\frac{S_{33}}{S_{13}} = \gamma \tag{4.3}$$

where γ is the poisson ratio. This value depends on the orientation of the crystal (see Fig. 4.11), but it is neS_{33} is never null, thus is possible to freely select the crystallography orientation for optimal channeling. The validity of this equation is limited to cases when the

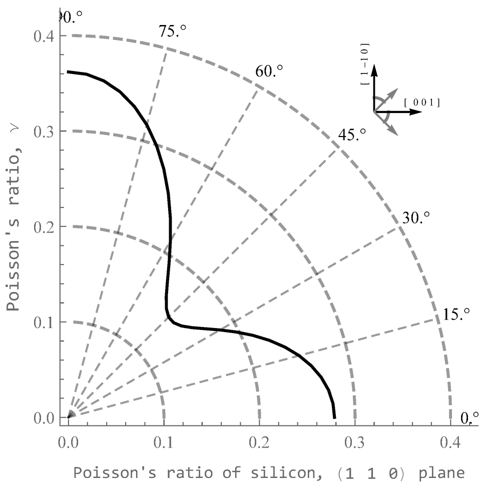

Figure 4.11: graph of Poisson ratio calculated with *Anicryde* software[127]

width of the sample is narrow enough to develop a plain stress regime: in fact, by increasing the crystal width b the system tends to behave like a plate under plain strain condition, thus preventing anticlastic deformation. The Searle parameter is used to evaluate this condition:

$$\beta = \frac{b^2}{Rt} \tag{4.4}$$

where t is the thickness of the crystal. If $\beta < 1$ anticlastic bending arises on the whole crystal width (beam-like behaviour); while if $\beta \gg 1$ anticlastic bending remains only in the external regions of the crystal (plate like behaviour). The following LHC crystal samples are well within beam-like conditions, thus a very uniform bending in obtained along the whole anticlastic length.

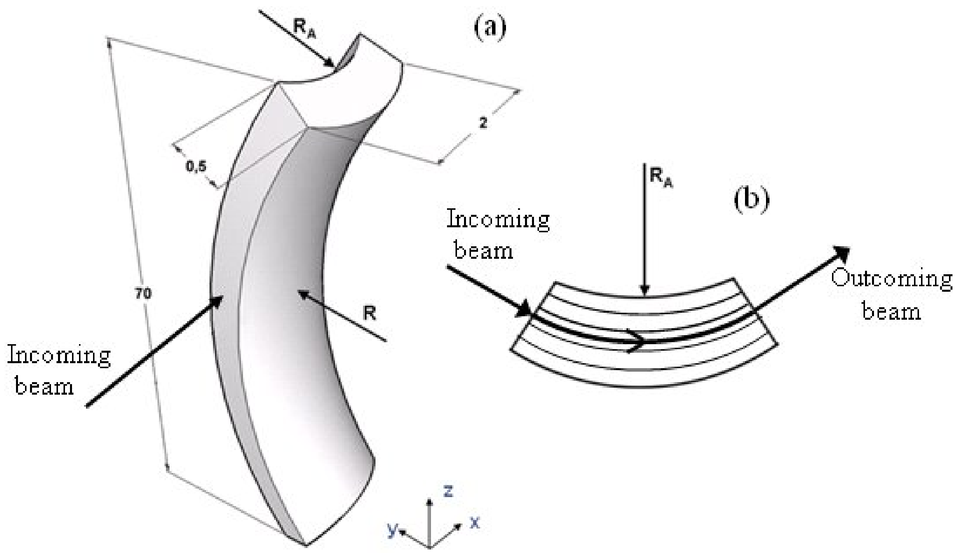

Figure 4.12: Scheme of the silicon strip anticlastic bending exploited for channeling particle steering[126]

crystal sample fabrication Once the wafer surface is correctly finished with suitable flatness, roughness and miscut, crystal samples can be cut from the sample into the desired shape. Geometrical size, orientation of the cuts and sharpness of the edges are important parameters. Indeed, most of the particles flux is concentrated on the first superficial layer of the crystal, thus edges must be For the cutting operation was employed a circular saw model Automatic DISCO dicing saw DAD 3220, available in the Sensor and Semiconductor Laboratory of the Department of Ferrara. The machine uses diamond coated blades that can rotate with a speed from 3000 to 40000 revolutions per minute. The samples are securely held during the cutting procedure by an adhesive film placed on a chuck equipped with a vacuum system. Alternatively, for greater stability the wafer can be bonded with thermal glue to a rigid sacrificial substrate. The chuck can move in the horizontal plane with micrometric precision and rotate with the accuracy of $\pm 25\ \mu rad$. In order to intercept the sample, the blade height can be adjusted with micrometric precision as well. Both superficial grooves and throughout cuts (up to 5 mm thickness) can be accomplished. Before cutting, the sample is aligned wrt to the blade by moving and rotating the chuck. A microscope is installed in order to inspect the sample and observe reference points such as wafer flats or previous cuts/grooves. Afterwards the chuck moves into the spinning blade with speed controlled with $\pm\, 0.05m/s$ precision. To prevent overheating and the consequent rupture, during the cut sample and blade are cooled with demineralized water, through two nozzles at the sides of the blade and a nozzle that sprays directly on the point of contact. The amount of water is dosed in such a way as to avoid that this causes the detachment of the sample from the chuck during cutting the same, but at the same time to ensure a good refrigeration system and removal of part of the silicon dust created by the cutting process. The Dicer is controlled through an internal computer where cutting sequences and parameters can be programmed. In the market there is a wide range of diamond blades with various technical characteristics, the most interesting for our sample cutting procedure are the grit and thickness, where the grit specifies the degree of abrasiveness of the blade and determines the diameter of the diamond grains present on the blade. In table 4.3 are listed the features of the blade used to cut the samples

Grit	**Grains size**	**Grain density**
1500	5 μm	60%

Table 4.3: parameters of the diamond coated dicing blade used for cutting the strips from wafer

The cutting procedure allows to freely select the crystallographic orientation, while techniques like anisotropic etching are only available for specific case[128]. The main drawback the cutting technique is the formation of a damage layer on the diced surfaces. As channeling requires lattice structure close to perfection, any defect hinders the performance of the crystal deflector and must be removed. This procedure was carried out using two different approaches: chemical wet etching or mechanical lapping and polishing. Removal of the damaged layer via chemical etching allows to avoid causing further damage on the lattice during the procedure. In order to preserve the integrity of the non-machined faces of the sample, the whole wafer was coated with a $10000\mathring{A}$ thick film of silicon nitride (Si_3N_4) via low stress chemical vapor deposition. The solution prepared for the process is composed by three acid: HF, HNO_3, and CH_3COOH (HNA) [129]. Such etching mixture is widely used in silicon micromachining. Nitric acid readily oxidizes Si to SiO_2, which is eroded by HF, acetic acid serves as a solvent and makes the reaction more controllable. Such etching mixture is particularly suited to etch silicon isotropically, i.e. with the same rate independently of the crystallographic orientation. The whole process is summarized in the following formula:

$$3Si + 12HF + 4HNO_3 \rightarrow 3SiF_4 + 4NO + 8H_2O \tag{4.5}$$

The solution composition was 3 parts HF (50%), 5 parts HNO_3 (70%) and 3 parts CH_3COOH (99%); the etching speed of the process was estimated $\approx 50\ \mu m/min$ and from the samples cut faces were etched $\approx 100 - 120\ \mu m$. Mechanical removal of the damage is possible as well, the lapping process consists in inducing friction between the sample and a liquid solution containing small hard particles. In this case, the lapping process was performed at ESRF Crystal & Crystal Analyser Laboratories. The samples were aligned and bonded together with wax into a single item, with glass external plate to protect the otherwise exposed outer samples. Lapping starts with 2:15 solution of aluminum oxide 9 μm particles with demineralized water, afterwards the solution is exchanged for one with smaller particles (3 μm). The finishing of the surfaces is achieved via *polishing* of the surfaces. Polishing is similar to lapping, but the solution exerts much less friction on the surface. Indeed, removal of material take place in ductile regime and not in brittle regime as in during lapping. The material removal speed is much slower and delicate, thus mirror-like surfaces free of damage are obtained. Afterwards samples are de-bonded and cleaned from wax. The samples produced are of parallelepiped shape (henceforth called *strip*). The length along the beam is fixed at 4 mm for all samples as this parameter is calculated to optimize channeling efficiency. The sizes transverse to beam direction have less constrains, the length in one direction was selected 55 mm in order to easily achieve beam-like regime in anticlastic deformation and leave the metal holder parts clamped to the ends of the strip as far as possible from the . Crystal thickness is an important parameter for crystal bending as it influences the rigidity of the strip. For the first prototypes on adjustable holders thin strips were selected, with 0.5 mm thickness. For the newer samples mounted on static holder, thicker samples were selected with four times the thickness (2 mm).

4.4 Bending Characterization

4.4.1 Characterization in Ferrara

Precise measurements of the curvature imposed on a crystal sample is crucial for the production process. Indeed, as will be explained in Section 4.5, a system to check bending of samples is essential in order to correctly calibrate the holder curvature. Also for the newer static holders (Sec. 4.6) fabrication techniques and manual mounting of the silicon strips cannot alone guarantee for the resulting curvature and torsion without a careful control. Optical interferometry can measure the shape of the surface of the crystal with nanometric vertical sensibility and micrometric lateral resolution. The instrument employed was the optical profiler Veeco NT1100 (Veeco Metrology Group). It exploits white light travelling through an interferometric objective and illuminates the sample to measure. Along the path the beam an impact on a partially reflective mirror, and half of it strikes a reference surface internal to the interferometer. The beam reflected from the sample being measured and the reflected one from the reference sample are recombined in a series of interference fringes, where the best contrast between the fringes represents the best focus. The following picture 4.13 shows the scheme of the interferometer. This system can be used in two ways:

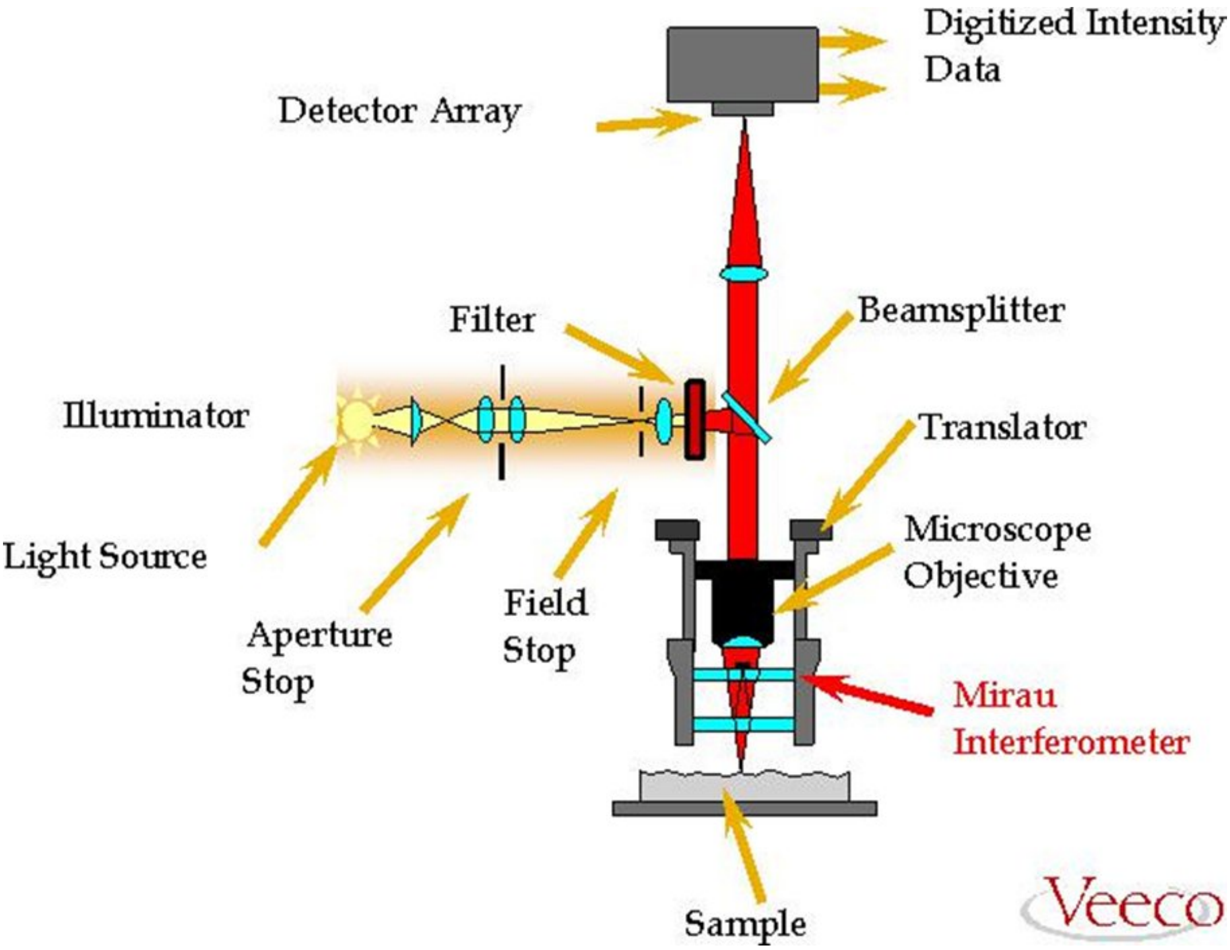

Figure 4.13: scheme of the interferometer Veeco NT110.

Phase-shifting Interferometry (PSI) and *Vertical Scanning Interferometry* (VSI). The latter mode is mainly employed for samples with either discontinuous morphology (such are steps in micromachined silicon) or relatively higher roughness. For the characterization of finely polishes crystals the first and more precise techniques was adopted. The PSI (Phase-shifting Interferometry) uses a filtered light (632 nm) for its operation. During the measurement, a piezoelectric transducer (PZT) linearly moves the reference surface of a small adjustable amount, in order to produce a phase shift between the reflected beam from the sample being measured and reflected from the reference sample. The system records the intensity of the interference pattern at different phase shifts, and then converts the data by integrating the field intensity. The data are processed to remove phase ambiguity between adjacent points, and so is calculated the relative height *h(x,y)* of the sample surface by the variation of phase as follows:

$$h(x,y) = \frac{\lambda}{4\pi}\Phi(x,y); \tag{4.6}$$

Where λ is the wavelength of the beam and $\Phi(x,y)$ are the phase data. This method is only usable for sufficiently planar and continuous surfaces, because if two adjacent points differ by height more than $\lambda/4$, which is $\approx 160\ nm$, there may be errors on the height of multiples of $\lambda/2$. To resolve rougher surfaces or steps, the interferometer relies on VSI measurements. This operation uses white light and also in this case a partially reflective mirror. The two beams respectively invest the sample to be measured and the reference one and then recombine in an interference pattern, where the best contrast between the fringes represents the best focus. In this case, however, the system measures the extent of fringe modulation, or coherence, instead of the phase between the interference fringes. The technique consists in the variation of the beam optical path through a continuous shift of the vertical axis of the objective, moving the focus to the sample and then measuring the surface at various altitudes. For both techniques using a white light source, which in the case of the technique PSI is filtered to obtain a monochromatic beam with a wavelength of 632 nm.

The magnification is achieved by two stages of exchangeable lenses: the objective lens, i.e. the one that moves during the VSI measures, and the FOV (field of view) lens, which extends the range of magnification of the objective lens. The interferometer available at the laboratories of the University of Ferrara used to measure the samples is able to obtain a magnification from 1.25x to 100x.

This technique is highly sensitive, thus nanometric imperfections in the optics of the instrument affects measurements. The issue is dealt with by calibrating the system with a reference mirror. The mirror certified flatness guarantees less than $1.25\mathring{A}$ in a neighbourhood of a circle of radius 1 mm. Thus, when a measure of it is acquired, the resulting shapes are caused by aberrations from optics. The acquiring software in following measures subtracts the calibration image from the results.

Another step necessary to increase the reliability of curvature estimation is the rejection of the surface local morphology contribute. Indeed, the sample surface should not be considered perfectly planar at this scale of precision. Hence the sample is measured before bending, in order to assess the surface shape up to nanometric details. Once bent, the

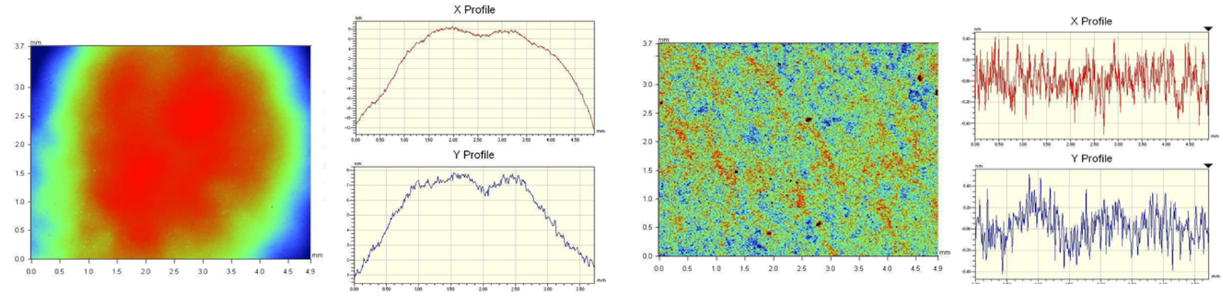

Figure 4.14: (a) measure of the reference flat mirror, the images and profiles indicate the optical aberration induced by the lens imperfection. (b) measure of the flat after calibration, roughness $R_a < 1nm$ and flatness of the reference are successfully observed

sample is observed a second time and the previous measure is subtracted from the acquired image (similarly as the calibration procedure). The final result is a pure indication of the effects caused by the bending procedure, thus the precision of the interferometer is fully exploited.

A second technique is employed, in order to further control the curvature of the samples. While interferometry observes the shape of the surface, *x-rays diffraction* allows to directly interact with lattice planes. Analysis is performed using a high- resolution X—rays diffractometer Panalytical X'PERT3 MRD (XL) (XRD). The radiation source is a x-rays tube with Cu target, beam through a Goebel mirror reduces angular divergence to $0.02° - 349\ \mu rad$, then Cu $k_{\alpha 1}$ ($\approx 8.04\ keV$) energy is selected by a four-bounce Bartels germanium monochromator. Beam after these optics is highly monochromatic ($\Delta\lambda/\lambda \approx 10^{-5}$) and with small angular divergence on the horizontal plane ($\approx 0.003° - 52\ \mu rad$). The size of the beam is controlled by metal slits with 10 μm accuracy, which can be additionally checked during operations by translating a sharp edge (*"knife"*) over the beam. Measures are usually carried out with $1x10mm^2$ beam size, reduced to either $0.1x10mm^2$ or $0.5x1mm^2$ when larger space resolution is required (but at cost of strong reduction of beam flux). The sample is mounted onto the cradle which allows large control over position:

- 3 orthogonal translation axes with resolution of $\pm 5\ \mu m$ (x-y) and $\pm 0.5\ \mu m$ (z)
- 2 rotation axes ϕ and χ with $0.01° - 174\ \mu rad$ precision
- 1 high resolution rotation axis ω with $0.0001° - 1.7\ \mu rad$ precision

Moreover, the detector can be positioned at precise angle wrt the beam with high precision $0.0002° - 3.4\ \mu rad$ as well. XRD is equipped with two detectors. Both are gas ionization detectors and measure the flux of the incoming beam, without providing imaging details. The *open detector* (OP)does not discriminate the direction of the incoming photon within $\pm 0.5° \approx 8.7 \times 10^3 \mu rad$ from its nominal orientation 2θ, it is employed for studies on crystal bending or for material phases identification. The second detector is called *triple axis* (3AX)and differs from the open one because it only counts photon which has been diffracted into it by a germanium crystal suitably aligned, this allows for a fine angular acceptance of $\approx 0.003° - 52\ \mu rad$ with respect to the detector angular position. The two detectors are both installed on the instrument and can easily be switched by changing a fixed bias on the 2θ axis.

The measure is obtained by exploitation of the selective condition for x-rays diffraction given by the Bragg law:

$$2d \sin(\theta_b) = n\lambda; \tag{4.7}$$

where d is the interplanar distance, λ is the wavelength of the x-rays radiation, n is an integer and indicate the order of the diffraction, and finally θ_b is the *bragg angle* between incoming beam and lattice plane for which reflection takes place. For the case of silicon samples mounted on XRD, both d, n and λ are of course inherently fixed (monochromatic beam and single crystal). Whereas in a bent crystal the angle between incoming x-rays

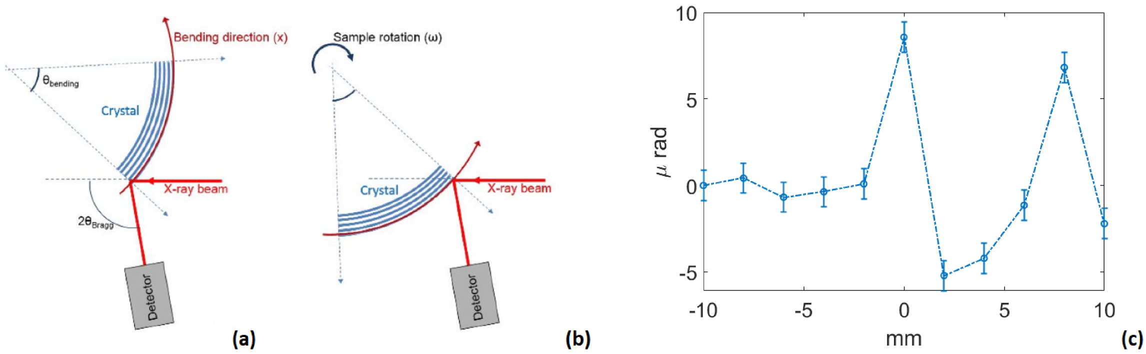

Figure 4.15: (a)(b) angular shift of alignment with x-rays beam with crystal planes at different position on a bent crystal. (c) misalignments induced by mechanical plays during sample translation

beam and lattice planes is a function of the position along the curvature. The diffraction peak can only be observed by adjusting crystal alignment for each position. Recording this angular shift along anticlastic curvature of a strip is a direct method to evaluate the angular deflection a channeled particle will undergo as its trajectory must remain parallel to the lattice planes. In case of uniform bending, the angular shift is constant and thus the radius of curvature can be calculated as

$$R = \frac{1}{\Delta\omega} \tag{4.8}$$

where $\Delta\omega$ is the angular shift expressed in radians. The anticlastic curvature can be measured directly along the 4 mm length or exploiting Poisson's ratio relation previously stated in eq 4.3.
Operation for this technique requires small rotation of the sample on the ω XRD axis (*rocking curve* RC)at different position, and calculation of the centroid of the RC each time. Although small rotation of the rocking curve is reproducible within $0.0001° \approx 1.7\ \mu rad$, the translation mechanism could lose such a fine alignment due to mechanics plays and thus add an additional angular shift completely unrelated to the sample bending condition. In order to avoid such issue, RCs were measured on a flat crystal during the same translation executed to perform a curvature measure. In such situation, the only sources of angular shift are caused purely by instrumentation errors. This procedure was repeated ≈ 100 times and the resulting errors were fairly reproducible, thus have been treated as a constant bias and subtracted from sample characterization.

The measure of torsion was obtained in an analogous way, by observing angular shift of RCs on the entry face of the crystal. In past years a very good agreement between x-rays characterization and direct measurements with relativistic particles beams have been observed.

Sample Name	**Bending Angle X-rays** [μrad]	**Bending Angle Channeling** [μrad]
STF47	33 ± 2	34 ± 2
STF48	144 ± 2	144 ± 2
STF49	247 ± 3	247 ± 2
STF50	142 ± 5	139 ± 2
STF51	33 ± 2	33 ± 2
STF70	56 ± 2	52 ± 2
STF71	60 ± 5	61 ± 2
STF99	119 ± 3	120 ± 2
STF100	67 ± 6	63 ± 2
STF101	170 ± 6	165 ± 2
STF102	45 ± 3	42 ± 2
STF103	52 ± 5	55 ± 2
STF105	49 ± 3	50 ± 2

Table 4.4: list of crystal previously produced in Ferrara[130–133]

4.4.2 Test beam at H8

After being produced and characterized in the laboratory of the University of Ferrara, the deflection angle and steering efficiency of the bent crystals was directly measured within UA9 collaboration. During 2016-2018, a total of 8 beamtests were performed at H8 extracted beamline of SPS, in CERN North Area. The H8 beamline uses a secondary beam produced by the collision of 400 GeV protons extracted from SPS into a 30 cm thick beryllium target. Magnets and collimators separate the different types of particles produced and select beam momentum. The chosen particles are secondary pions (π^+) in order to maximize flux and momentum. The beam is supplied during $\approx 10\ s$ spill every $\approx 35\ s$. In the following table 4.4.2, beam parameters are summarized.

Particles type	π^+
Beam Momentum	180 GeV
Horizontal Size	$\approx 2\ mm$
Vertical Size	$\approx 2\ mm$
Horizontal Angular divergence	$30 \pm 2\ \mu rad$
Vertical Angular divergence	$44 \pm 2\ \mu rad$
Average Flux	$\approx 3.5 - 4 \times 10^5\ pps$

Table 4.5: summarized beam parameters

The particles are tracked using a silicon strips telescope, designed and assembled by Blackett Laboratory of Imperial College group for UA9 collaboration[134]. A total of five station are placed along the beam in the experimental area. Two are placed upstream the crystal and three downstream (fig.4.16). Each station is equipped with two silicon microstrip detectors fabricated by Hamamatsu Photonics (HPK) on high resistivity float-zone material, one for horizontal position measure and the other rotated 90° to measure the vertical one. Each detector consists in a total of 639 microstrips, each 60 μm wide and 320 μm thick. The total active detection area is $3.8 \times 3.8\ cm^2$. Angular resolution on the incoming angle reach 2.8 μrad, and a total resolution limited to 5.2 μrad by multiple scattering caused by the sensors themselves. When a particle crossed the detector, the position and timing is recorded. Reconstruction software then analyses and associates the events which align in two straight lines with vertex on crystal position (approximated as a point-like object). Identification of each particle's trajectory is critical for a precise experimental assessment of channeling efficiency. Indeed, trajectory reconstruction allows to identify the part of the beam which actually intersects the crystal. Moreover, from the two planes upstream the sample is possible to calculate the incoming angle of the particle.

Thanks to this information is possible to discriminate particles impacting the crystal at angles larger than the critical one for planar channeling.

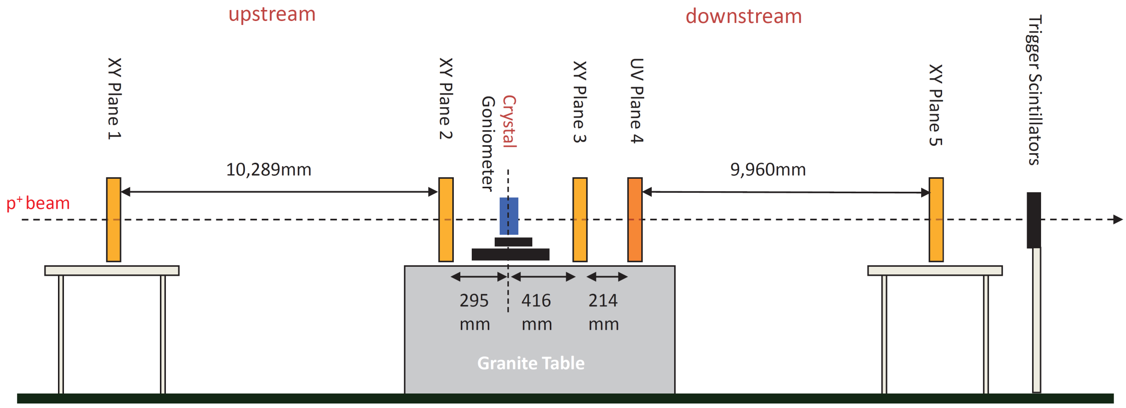

Figure 4.16: Experimental layout in H8 beam line for UA9 channeling experiments

The goniometer necessary for alignment of crystal is placed on a granite table, in order to guarantee stability of the assembly from vibrations during the experiment. After mounting the samples, an optical laser system is exploited to roughly pre-align lattice planes to the crystal. A reference mirror is installed in the experimental area, previously positioned in order to be as parallel as possible to the particle beam. A laser is aligned perpendicular to such reference, exploiting a pentaprism to place the source few meters upstream thus extending the optical lever arm. The sample is installed before the reference mirror and reflects the light back to the laser source. In order to align the crystal, the reflected light must return back to the laser source. As the techniques align the crystal surface, if the miscut of the sample is known, it must be compensated by rotating accordingly the sample. This method allows to achieve rough alignment within 150-200 μrad, strongly reducing the time needed for the alignment procedure. To perfectly align the crystal with the beam, an angular scan is performed with the goniometer while particles impact the sample. The alignment is achieved once the channeling phenomena is observed, i.e. when a portion of the beam gets deflected. Once found precisely the angular position which roughly maximize steering efficiency, the sample is left in a fixed position until a sufficiently large statistic is acquired.

4.5 First prototypes

In order to impose the desired bending to the crystal as well as for handling purposes special holders had been designed. The holders to bend strip crystals were initially devised in collaboration with the Russian Institute for High Energy Physics IHEP, and are based on deformation control technology. Since 2007 such holders have been designed in mechanical workshop of physics department and INFN of Ferrara University[116]. A screw is coupled to the holder by four bolts, by tightening or releasing the bolts the holder is elastically deformed thus changing the mounting surfaces tilt. After the bolts are adjusted, the strip is mounted on the holder. The strip opposite ends are firmly fixed on the two mounting surfaces. The mechanism is based on a titanium cylinder fasten with screws on the holder. The strip once mounted its ends are bounded to the holder surfaces tilt. If the two tilts are carefully regulated to identical opposite angles, the strip bends into an arc of circumference. As stated before in Sec. 4.3, to the main curvature (along the 55 mm length) an anticlastic one is generated along its 4 mm dimension. This technology allows to achieve with the same holder a large range of curvatures, on the other hand, mechanical strain due to holder deformation propagates through the holder and alters planarity and parallelism of surfaces where crystal lean on inducing torsion on the crystal. In order to correct for torsional effects a screw is used. Such screw—based torsion compensation system demonstrated to be very effective, allowing to obtain torsions of less than 1 $\mu rad/mm$. The holder is composed of a total of 14 parts:

- 1 "main component", made of Titanium grade V manufactured by "Cinel — Instruments for Research and Industry" by means of milling and and electro—discharge machining operations. Between milling and electro- discharge machining the part was subject to a thermal annealing in order to release the mechanical stress generated in the first operation (see table 4.5). Titanium grade V was supplied by "Stupino Titanium Company";

- dowel pins, diameter 2—H7 mm, made of Titanium grade V, provided by "Cinel — Instruments for Research and Industry". Those parts were manufactured by means of turning operations. Titanium grade V was supplied by "Stupino Titanium Company";

- 1 threaded bar M5X0.25, made of Titanium grade V and manufactured by the company the "Biomeccanica Srl" in April 2015 by means of turning op— erations. Prime Titanim grade V was supplied by "Tifast SRL"

- 6 nuts M5x0.25, made of Titanium grade V and manufactured by the company "Biomeccanica Srl" by means of turning operations. Prime Titanium grade V was supplied by "Tifast SRL";

- 4 screws M2, made of stainless steel 316 LN, provided by "Bulloneria Morelli Di R. Morelli 85 C. Sas".

Time [min]	**Temperature** [$°C$]	**Pressure** [mbar]
0	*Room temperature*	1.26×10^{-6}
30	350	3.24×10^{-6}
40	350	3.24×10^{-6}
70	700	3×10^{-5}
250	700	3×10^{-5}
1080	*Room temperature (radiative cooling)*	1.23×10^{-6}

Table 4.6: heating cycle performed by Cinel on holder main body

Two samples were produced and tested with 180 GeV π^+ beam. Before testing, curvature and torsion were tested using optical interferometry and x-rays diffraction. **STF107**

Sample	**STF107**	**STF110**
Thickness along the beam	4.08 ± 0.02 mm	4.00 ± 0.02 mm
Transverse length	0.55 ± 0.02 mm	0.50 ± 0.02 mm
Bending angle (x-rays)	56 ± 2 μrad	52 ± 3 μrad
Bending angle (interferometer)		53 ± 5 μrad
Torsion	$<\ 2$ $\mu rad/mm$	$<\ 2$ $\mu rad/mm$
Channeling Planes	(110)	(110)
Channeling Axis	$< 111 >$	$< 110 >$
Poisson's Ratio	6.14	3.59
Miscut	40 ± 4 μrad	4 ± 2 μrad

Table 4.7: table shows the parameters measured at SSL of Ferrara for the prototypes for LHC

was a silicon strip with "large" miscut, but it otherwise meet every requirement for LHC installation. The sample was tested twice at CERN on July and September 2016. Between the two measures, the sample was subjected to a heating cycle which simulate the bake-out procedure of LHC beam pipe. The sample bending condition remained stable during the process. **STF110** successfully met all requirement on bending and miscut necessary for LHC installation. A slightly different crystallographic orientation was selected, with respect STF107 and previous sample produced [116]. Whereas the channeling planes remained (110), the lattice axis along particle propagation is changed to $\langle 110 \rangle$. This does not affect the planar potential, but modifies the elastic properties of the strip. Beside holder imperfections, torsion can indeed be caused by crystal elastic anisotropy. In the configuration selected for STF110, such effect is strongly suppressed (while for STF107 is non-negligible). Similarly to STF017, the sample was tested twice on CERN H8 beamline before and after bake-out heating cycle. After heating steering the sample failed the stability test, as it showed a deflection angle variation of over 10 μrad. Such radical fluctuation is not compatible with LHC collimation, because it would lead to large variation in channeling efficiency. The non reproducibility of the prototypes' stability lead to discard of the technology for the following holder models. Indeed, the bending mechanism based on screws and bolts allows to actively modify the deformational states of the strips, bypassing strict mechanical precision constrains, but causes as well significant difference between samples.

4.6 New type: static holder

The new generation of holder was focused on achieving reproducible thermal stability. State of the art in controlled deformation of silicon crystals is nowadays dictated by technologies employed at worldwide x-rays synchrotrons, where controlled deformation of crystals, typically silicon or germanium is accomplished through mechanical benders actuated by motors. This choice allows complete control over the sample at any time during operation. Compensation of mechanical imperfections, which arise in mechanical manufacturing of benders or crystals, is then a relatively trivial issue. Recently channeling experiments following this principle has been performed at Mainz Mikroton, with few tens of microns thick silicon and germanium crystal, steering an 855 MeV electron beam [135]. Unfortunately, such solutions are not suited for the case of LHC, usage of motor-actuated benders might represent a risk. Fault of a motor might indeed compromise a key-component of the machine, and its replacement would be an operation far from trivial, as the crystal would operate in an extremely radioactive area. Moreover, a motor-actuated bender would likely result in a bulky device. Thus, the first step was the decision to avoid imposing curvature by stressing and deforming the holder itself. Indeed, pre-existing stresses could affect the stability of the sample during heating and affect reproducibility of the system. In order to accomplish this goal, a static version of the holder was devised. This allowed to significantly simplify the structure of the holder, in fact the number of components was halved from 14 to 7:

- 1 *holder main body* in titanium grade 2 or 5, fabricated by Perman Srl.
- 2 *mounting clips* to hold the silicon strip to the holder, also fabricated by Perman Srl.
- 4 titanium grade 2 or 5 *M2 screws*, ≈ 8 *mm* long.

The modification comes at expenses of stricter constrains over the precision during production and mounting of samples. Indeed, without any bending regulation mechanism, the holder requires to be manufactured in the perfect position. A total of 27 holders where produced and tested during this R&D project, in order to assure a comprehensive study over the features and reproducibility of the holders.

4.6.1 Holder

A static bender capable of impart the correct deformational state to the crystal looks the most promising approach, even if mechanical tolerances are extremely challenging.

Material of the bender must be compatible for operation in a ultra-high vacuum environment and should not lead to electron cloud activity in the accelerator [136]. Moreover, the assembly must remain as light as possible: alignment of the crystal to the beam is provided by a piezo-actuated goniometer; as for any piezo-actuated motor, its performances are maximized as it operates under as low as possible weights. A material satisfying the cited requirements is *titanium grade 5* (an alloy composed of 90% titanium, 6% aluminium, 4% vanadium) and *titanium grade 2* ($> 99\%$ pure titanium). This material, thanks to its low density and high strength, typically finds applications for aerospace, naval and biomechanical applications, engine components, sport equipment's, but is rarely used in ultra-high precision mechanics due to its poor machinability [137].

Instead of actively deform the structure of the holder, the surfaces were the strip is mounted (coloured in red in fig. 4.17) are already fabricated with the required inclination via electrical discharge machining. Thus, the strip is bent like in the previous generation, in order to produce the desired anticlastic curvature on its central zone. The angular offset is 822 ± 4 μrad, which corresponds to a slope of ≈ 0.1 μm over the length of 1 cm. Being the machine nominal precision one order of magnitude larger, the actual cut is performed along a longer distance $\gg 1$ cm. Consequently, the process cannot guarantee to successfully achieve the desired inclination. Thus, a strip is mounted on a new holder and its bending is quickly characterized via x-rays diffraction. If the assembly does not display the correct curvature, holder surfaces are machined another time. The same surface can be processed several times on the same holder.

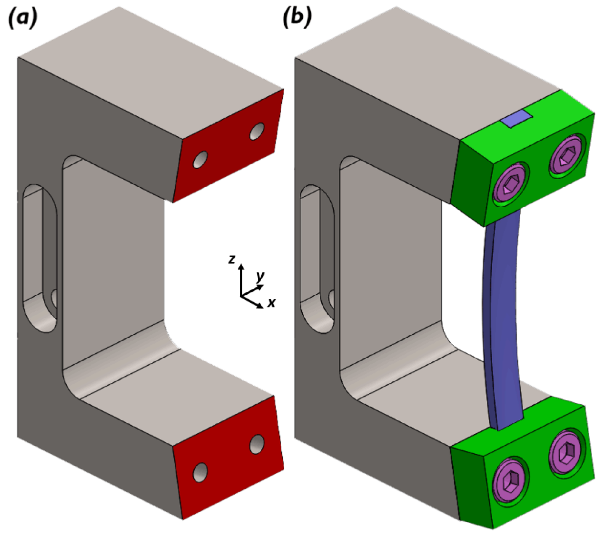

Figure 4.17: (a) Base structure of a static bender for strip crystals. Surfaces of red colour are tilted of 822 ± 4 μrad around the y-axis toward the inner side of the bender to impart a "primary bending". The same surfaces are tilted of less than 38 μrad around the z-axis to avoid torsion (for representation purpose tilting around the y-axis is largely increased). (b) Representation of crystal (blue colour) assembled on the bender device (deformation of the crystal is purposely enlarged). A couple of clips (green colour) clamps the crystal on the holder. Screws (violet colour) secures the clamps to the bender

The machining procedure generate on the holder a superficial layer of altered material few microns thick, composed mainly by oxides, carbides and other phases of titanium [138].This layer is also source of residuals stresses caused by inhomogeneity in temperature distribution during discharges and quenching effect of the dielectric fluids [138]. This layer is removed via wet chemical etching of the holder. The solvent solution is obtained by dilution of hydrofluoric acid in de-mineralized water in the following concentration:

$$HF(50\%) : H_2O = 1 : 13; \tag{4.9}$$

The holder is dip in the solution for ≈ 10 s and then into a baker of de-mineralized water. In order to remove efficiently solvent and residues from etching, the baker is placed in ultrasonic tank to enhance cleaning. Water is changed two times after 30s and 1 min. The last bath lasts $\geq$4 min. The whole procedure is then repeated two more times. After the first two iterations, the layer is not visible at naked eye inspection on the whole item.

A third and final etch is then performed in order to thoroughly remove even microscopic traces. Indeed, the total etching must be contained in order to limit excessive erosion and preserve the precise shape of the structure. The mounting clip, being fabricated as well with the same electrical discharge machining, follows an analogous etching procedure.

The mounting process is a critical step of the production, the assembly is carried out in clean room in order to avoid dust to hinder coupling between silicon strip and holder parts. The passage is handled manually, but tightening of the screws is executed using high precision torque wenches. The first torque starts at the lowest value of 0.08 $N \times m$ and progressively scale up at step of 0.1 $N \times m$. The torque imposed on the screws is the only parameters which enables a minimum adjustment of the sample curvature and torsion. Tightening final part is carried out checking bending condition of the sample and correcting torsion. Unchecked torsion ranges from 5 $\mu rad/mm$ to 15 $\mu rad/mm$, the final torsion correction allows to suppress the value under the required limit.

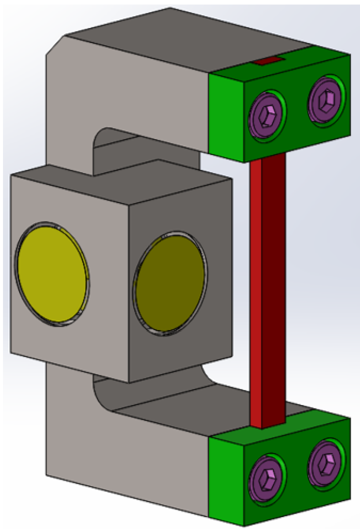

Figure 4.18: Coloured in yellow the two mirrors for optical pre-alignment of samples in LHC beam pipe. All the surfaces of the strip are polished and thus can be easily be inspected with optical interferometry techniques.

The design include the possibility to install a support for two small round mirror (see fig. 4.18). This addition is required only for samples which are installed in LHC. The mirrors are exploited as reference for the optical alignment set-up built in the beam pipe. In this case, the angle between strip surfaces and reference mirrors must be measured before installation. Such measurements can be easily carried out by Zygo Verifire HDX interferometer at SSL in Ferrara. Such instruments exploit a collimated laser beam with minimal angular divergence and 150 mm diameter, allowing interferometric measurements of aligned surfaces at difference distance from optical interference cavity. Thanks to the nanometric precisions along the laser path and micrometric lateral resolution, the measurement of the tilt between crystal and reference mirror is expected to be measured with accuracy of few microradians.

4.6.2 Thermal stability

Ultra-high vacuum inside the LHC beampipe ($\lesssim 10^{-10} - 10^{-11}\ mbar$) is a critical feature for the performance of the machine. In order to achieve the best possible condition, a bake-out procedure is needed to allow fast and efficient de-adsorption of molecules from pipe internal surfaces. As a direct consequence the bender-crystal assembly must satisfy is the stability of the crystal deformational state with respect to vacuum bake-out cycles. The assembly must indeed operate in a ultra-high vacuum environment. Reaching of the operational conditions is accomplished through a minimum of three bake-out cycles which brings the chamber with installed the crystal at $250°C$ for 48h for each cycle. In order to assure thermal stability of the bender material, a series of annealing thermal cycles are performed on titanium material prior and after its machining process.

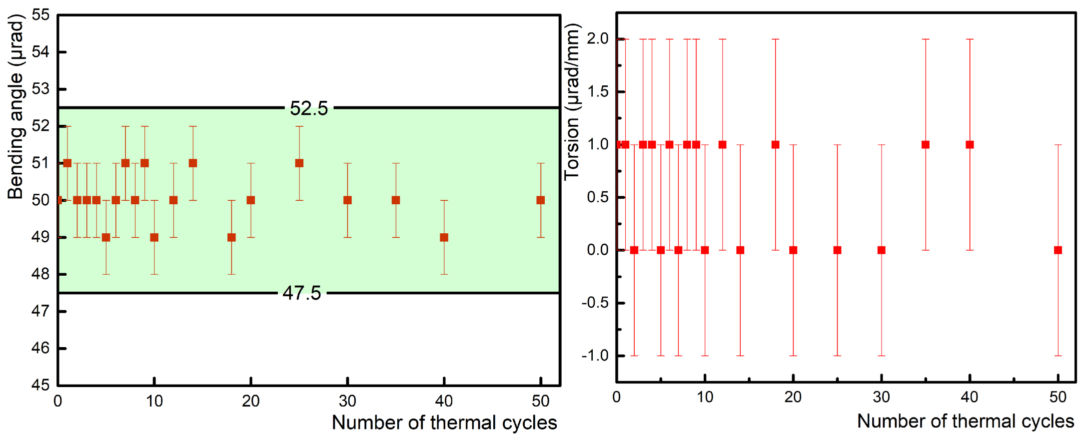

Figure 4.19: . Study of thermal stability of the crystal against bake-out thermal cycles. (a) Value of bending angle vs the number of thermal cycles. Green area highlight the region of acceptable bending angle of the crystal expressed in Tab. 4.2 . (b) Measured torsion as a function of the number of thermal cycles. Stability of the bending angle and torsion values demonstrates the robustness of the crystal deformation state and of the bender

We assume thermal stability of the assemblies if the crystal does not change its deformational state after at least 10 vacuum bake-out cycles: crystal deformational state is characterized before and after each thermal cycle.

Figure 4.19 report measured bending angle and torsional value for a crystal subjected to a total of 50 thermal cycles, highlighting robustness of the assembly against thermal cycles of bake out.

4.6.3 Final samples

During 2018 a set of 10 low miscut strips were produced. The crystal were bent using the new static holders, bending and thermal stability were characterized at SSL in Ferrara and INFN National Laboratory of Legnaro (LNL). Planar channeling features were tested for all the samples using the 180 GeV π^+ at H8 beam line in CERN.

The silicon crystals were all cut from the same wafer in strips $2 \times 4, 1 \times 55\ mm^3$. Crys-

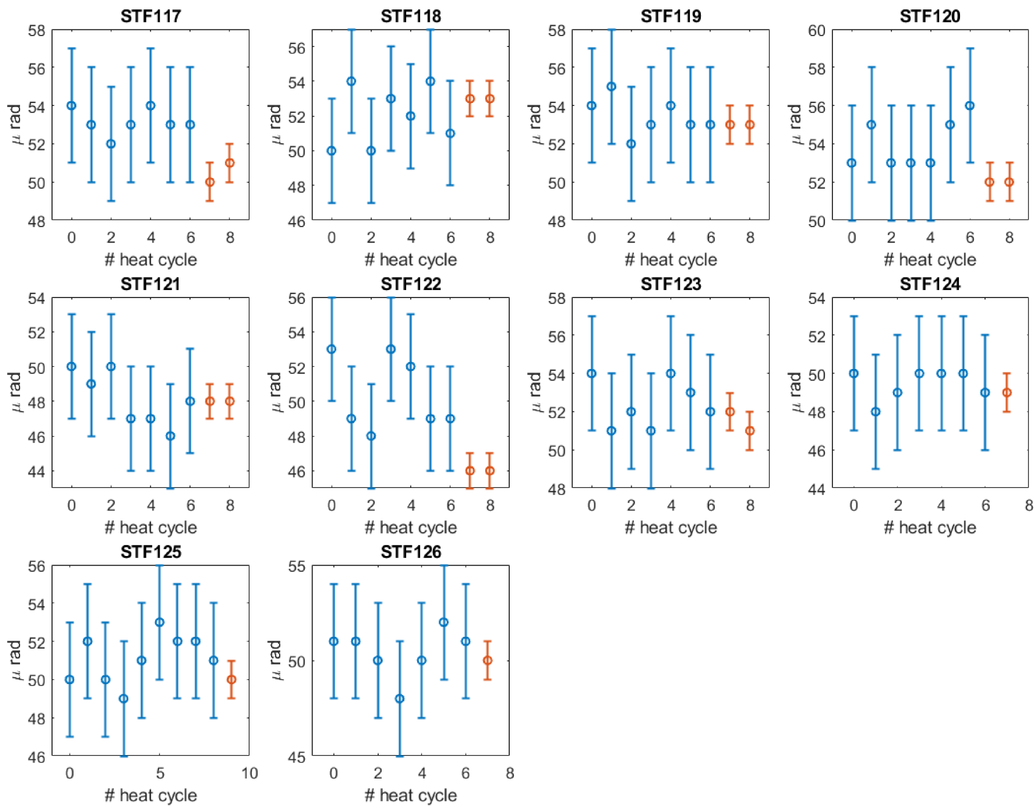

Figure 4.20: deflection angles of the samples produced in function of the heating cycles. Each cycle indicate one standard bake-out process for LHC beam pipe. The blue points indicate XRD measurements performed in Ferrara, while orange points indicate the steering angle observed with planar channeling of 180 GeV π^+ at H8 beam line.

tallography orientations selected for the samples were $< 110 > \times < 110 > \times < 100 >$, in order to exploit the more efficient (110) planes for channeling and suppress torsion contribute from crystal anisotropy. The damage on the cut surfaces was removed at ESRF Crystal & Crystal Analyser Laboratories via lapping and polishing, reducing the size to $2 \times 4 \times 55\ mm^3$. The strips were mounted on holders in the clean rooms of SSL in Ferrara, where the curvature was measured via x-rays diffraction. Only assembly with deflection within $52.5 \pm 3.5\ \mu rad$ were accepted for experimentation with particle beam. All the samples achieved suitable bending for LHC collimation. Heating cycles were performed at LNL: samples were installed in a quartz vacuum tube and pressure was decreased up to $10^{-7}\ mbar$. An oven mounted on rails slid over the tube and heated it up following the bake-out cycle for LHC. To optimize temperature homogeneity during the cycles, the samples were placed in the vacuum tube in order to end up in the central zone of the oven. After each heating cycle, the sample curvature was verified again in Ferrara with x-rays diffraction. The stability was deemed consistent with the measurement resolution. Thus, the samples were selected for direct measurements of planar channeling efficiency and steering at H8 extracted SPS beam line together the UA9 collaboration. The measurement obtained were consistent with the characterization performed in Ferrara. Samples tested on test beam of August 2018 underwent again another bake-out process. The operation were officially performed by personnels of CERN Technology Department's Vacuum Surfaces and Coating Group.

On the following test beam in September 2018, the same samples were tested again at H8 beam line. Analysis of the experimental data confirms stability of the samples, showing no significant change of performance before and after heating cycle. Only samples STF124, STF125 and STF126 underwent torsion adjustment during assembly. STF125 in particular passes all requirement for LHC installation.

Sample	Deflection Angle	Efficiency within θ_c	Torsion	Δ Deflession After CERN Heating
STF117	50 ± 1 μrad	$66 \pm 2\%$	-5 ± 1 $\mu rad/mm$	$-1 \pm 1 \mu rad$
STF118	53 ± 1 μrad	$64 \pm 2\$$	-6 ± 1 $\mu rad/mm$	$0 \pm 1 \mu rad$
STF119	53 ± 1 μrad	$66 \pm 2\%$	5 ± 1 $\mu rad/mm$	$0 \pm 1 \mu rad$
STF120	52 ± 1 μrad	$xx \pm 2\%$	15 ± 1 $\mu rad/mm$	$0 \pm 1 \mu rad$
STF121	48 ± 1 μrad	$67 \pm 2\%$	5 ± 1 $\mu rad/mm$	$0 \pm 1 \mu rad$
STF122	46 ± 1 μrad	$66 \pm 2\%$	-14 ± 1 $\mu rad/mm$	$0 \pm 1 \mu rad$
STF123	52 ± 1 μrad	$62 \pm 2\%$	-13 ± 1 $\mu rad/mm$	$1 \pm 1 \mu rad$
STF124	49 ± 1 μrad	$67 \pm 2\%$	0 ± 1 $\mu rad/mm$	not measured
STF125	50 ± 1 μrad	$65 \pm 2\%$	3 ± 1 $\mu rad/mm$	not measured
STF126	50 ± 1 μrad	$66 \pm 2\%$	3 ± 1 $\mu rad/mm$	not measured

Table 4.8: results of channeling experiments and heating cycles performed at CERN on static holders.

Chapter 5

Future Applications of Bent Crystal for High-Energy Physics Experiments

Beside beam collimation of LHC, other promising experiments can be developed exploiting bent crystals. In this work, two applications in LHC are investigated in particular: beam extraction into external beamline and spin precession of charmed baryons. The two projects were both financed by European Research Council and focused on very different physics fields: the first on cross section calculation and back-region QED dynamics studies, while the second on electromagnetic dipole measure and baryon spectroscopy. Nevertheless, bent crystals were crucial for either experiments. Indeed, this fact strongly emphasizes the versatility of the technologies and its potential to enable novel approaches in high energy physics. The crystal deflectors described in this chapter differs from the ones previously introduced for LHC collimation and thus require dedicated R&D. In the first place, the appropriate thickness along the beam for the applications is 5-10 cm and steering of 1-17 mrad. Such lengths and angles were very common in first channeling experiments, however the solutions adopted lacked crystal and curvature optimization needed for operation in LHC. Hence the whole mechanical holder concept must be revisited, if not discarded completely to favour self-standing techniques approach. Furthermore, spin precession would strongly benefit from exploitation of other materials beside silicon. Indeed, semiconductor industry is nowadays able to offer Germanium crystal of quality comparable to silicon (although at higher price). Germanium displays stronger potential than Silicon, but also requires special care in handling process and not all fabrication processes possible on Silicon are available.

5.1 Crystal assisted beam extraction

Beam extraction from a particle accelerator is performed via electromagnetic optics. It is possible to modify the dynamics of the beam in order to extract only a part of the beam. Bent crystals are an alternative solution for the issue. The application has been investigated worldwide in several facilities.

First experiments were performed in Russia, large deflection angles were selected in order to obtain clear and unequivocal signal to prove crystal assisted steering phenomenon. The very first attempt to extract a circulating beam was performed at Dubna Synchrophasotron in the 80's [13]. An 11 mm long crystal was employed, intercepting part of the 8.4 GeV proton beam and thus operating in parasitic mode. The deflection angle achieved diverted a at an angle of 35 mrad with an efficiency of $\approx 10^{-4}$. After this first success, an extensive experimental campaign was carried out at U-70 (IHEP, Protvino, Moscow) using higher energy beams. Protons with 50 and 70 GeV momentum [14, 15] were extracted, efficiency was improved and reached about 1%. These low extraction efficiencies were ascribed to a not optimized crystal features (such as length, radius of curvature etc.)[16] or to an non ideal experimental set-up [13]. Indeed, such a large deflection angles had the main drawback to decrees channeling efficiency. Moreover, technologies employed for samples bending could not achieve the homogeneity essential to suppress dechanneling of the particles travelling in the crystal.

Although the obtained results showed low efficiency, they demonstrated for the first time the channeling phenomenon. In the late 90s further development of beam manipulation via channeling was carried out at CERN with proton beams of energies of 14, 120 and 270 GeV [17–19] and at Tevatron proton beam of energy 900 GeV [20, 21]. The experiments successfully increased the efficiency of the steering process by one order of magnitude, reaching respectively ≈10% and ≈25%. However, slow extraction approaches resulted far superior at the time (≈98%). Such low values were attributed to the presence of an imperfect layer on the crystal surface [18, 22, 23], unwanted parasitic effects in the deformation of the crystal [17, 23], and to an inappropriate choice of the length of the crystal [22, 24–26]. Regarding this last point, simulations demonstrated [22, 23] that the length of the crystals used at SPS and Tevatron (30 and 40 mm respectively) was optimized for operations in single-pass mode, not in multi-pass. Taking into account this effect, crystal about 5 times shorter would have maximized extraction efficiencies reaching values about 3 times higher. Recent simulations predict the possibility to reach an efficiency of 99% for 270 GeV proton extraction from the SPS [27].

Simulation models proved to be invaluable tools in the design following crystalline deflectors and drove the design and manufacturing of a subsequent generation of crystals [28] and bending schemes [29, 30]. This progress resulted in a considerable increase of extraction efficiency, which reached the value of 85% [29] in single pass mode.

At the same time, semiconductor research during the last 20 years accomplished great progress in crystal manufacturing and characterization. This allowed to manufacture crystals free from lattice damage, surface roughness lower than 0.1 nm. Driven by those results, an intense experimental campaign [32] investigating the possibility to collimate or extract the proton beam circulating in the LHC was started in the late 1990 at H8 and H4 extracted lines of the SPS. New coherent interaction effects of ultra-relativistic proton beams with crystals were observed, among which were the phenomena of volume reflection [34, 81], beam steering by means of crystal axes [35–37], multiple volume reflection [38–41] and mirroring [42]. For the first time, efficient beam steering was also recorded for both positively [43–45] and negatively charged particle beams [46, 47]. Current performances of crystal assisted beam steering indeed are now competitive with other beam extraction techniques, and the compact size of the setup allows to operate only on a selected faction of the beam.

Extraction of the LHC beam - the CRYSBEAM project

Crysbeam project proposed the employment of a crystal to extract the multi TeV proton beam of LHC beam into an external beamline. The employment of a crystal would allow to operate in parasitic mode, only intercepting the halo of the beam. The deflected protons could then be exploited in fixed target experiments. In particular, a gaseous target could simulate earth atmosphere in order to reproduce the beginning of cosmic rays' showers. The crystal necessary for efficient extraction design was developed starting from LHC crystal collimators requirement of high efficiency and low beam impedance. While the crystal collimation scheme requires an angular kick of a few tens of μrad by keeping the halo particles within the beam pipe radius, beam extraction out of the beam pipe would require a deflection angle of $\phi \approx$1 mrad. This approximate value of steering angle was found to be appropriate in a conceptual scheme of extraction in the LHC [139]. In fact, the aim of collimation is to deflect the beam towards an absorber located in the beam pipe downstream of the crystal. On the other hand, a large angle is required for beam deflection to achieve an adequate separation of the extracted beam from the primary beam. In order to attain such larger deflection, the only available options are either the increase crystal thickness along the beam (L)or the reduction of its curvature R, since the final deflection is defined as $\phi = L/R$. As previously stated in chapter 2, at high energy channeling efficiency is strongly dependent on the curvature. The radius of curvature should indeed be left as large as $R > 6R_c$ [45], thus this parameter must not be modified significantly from the value selected for beam collimation. Differently, channeling efficiency for a beam of positive particles at 7 TeV/c is weakly affected by the crystal length. Hence a hundred millimetres long crystal would in principle achieve a high channeling efficiency, of the order of 80-90%. Thus, the optimal configuration for extracting the LHC beam would be a crystal featuring $L \approx 100$ mm and $R \approx 100$ m.

5.1.1 Long anticlastic

The crystals currently used at LHC for collimation tests are made of silicon. In order to deflect charged particle beams, both anticlastic [29, 30, 50] and quasi-mosaic [140, 141] deformation have been exploited. Unfortunately, the quasi-mosaic effect does not allow to operate with a ≈100 mm long crystal. Indeed, the quasi-mosaic effect consists in the bending of a family of lattice planes which are perpendicular to the surface of the primary curvature. Thus, in the case of a plate crystal, its thickness would be of the order of ≈100 mm. Such samples would be to rigid to efficiently bent, without an heavy and bulky setup. On the other hand, the anticlastic deformation can be exploited to realize crystals whose length along the beam direction can be even hundreds of mm. Up to now, the crystal for beam deflection manufactured in Ferrara feature a strip-like shape, i.e. the crystal length (L) is much smaller than its height (h).The crystal prototypes for LHC collimation exploiting the anticlastic deformation 4 mm long (L) and 55 mm high (h), resulting in an aspect ratio $L/h \approxeq 0.1$. The primary bending being imposed by clamping at their edges to the holder, where a momentum was forced on the crystal.

Unfortunately, the geometry developed for the crystal collimation cannot be rescaled for beam extraction because a crystal with length along the beam of ≈ 100 mm and the same aspect ratio would result in a 1 m high crystal. Even without considering the need for an appropriate bending device, it would be too large and bulky for an installation in a beam pipe.

In this paper, we propose to keep h at about 40 mm and to increase L to about 100 mm, i.e. a crystal with an aspect ratio of 2.5. For such new crystals, the usage of the described bending scheme would strongly suppress the anticlastic deformation [142, 143]. Thus, we manufactured a new bending device that is a redesign of the bending device previously developed. In particular, this new holder allows us to apply two identical and adjustable moments at two crystal edges of a plate crystal and to enhance its anticlastic deformation, instead of suppressing it; more details on this bending device will be reported in a dedicated paper.

Crystal manufacturing and bending

Two different samples were produced and characterized at the Sensor and Semiconductor Laboratory of the University in Ferrara (SSL), namely sample 1 and sample 2. The samples are made of high quality silicon, with a density of dislocation <1/cm^2, as certified by the manufacturer.

Sample 1 was produced with $L/h < 1$. It was mounted on a holder similar to the one used for the strip-like samples. On the other hand, sample 2 was manufactured to feature $L/h > 1$. This sample is the first one with these characteristics that is bent by means of a holder for such a purpose. All the sample parameters are listed in Tab.5.1.

	Sample 1	Sample 2
Channeling plane	(110)	(111)
Channeling Axis	<100>	<110>
Height (h) - x [mm]	55.0±0.1	39.0±0.1
Length (L) - y [mm]	23.8±0.1	56.8±0.1
Width (w) - z [mm]	0.52±0.02	1.00±0.02
Density of dislocations [$1/cm^2$]	< 1	< 1
Interferometric measurement results		
Bending angle ϕ (μrad)	1877±94	716±36
Anticlastic R (m)	12.1±0.6	79.9±4.0
XRD measurement results		
Bending angle ϕ (μrad)	1840±24	714±24
Anticlastic R (m)	12.9±0.6	79.6±4.2

Table 5.1: summarizing tables for samples geometric and crystalline characteristics and curvature measure with both interferometer and diffractometer.

Sample 1 and sample 2 were manufactured to be 520±20μm and 1000±20μm wide, respectively, through a merging of the techniques described in [28] and in [128]. Since miscut reduction techniques are applied on the whole wafer, no further investigation is required during the development of samples for extraction. Hence, correction of miscut was skipped during the development of these extraction prototypes, being the procedure both long and expensive. Indeed, the samples will not be installed in LHC, and small variation of miscut does not significantly modify elastic properties of the assembly. The first step of the fabrication was the coating of the wafers with a 100 nm thick film of silicon nitride (Si_3N_4) via Low-Pressure Chemical Vapor Deposition (LPCVD). Then, the samples were shaped using an automatic diamond blade dicing saw (Disco DAD 3220). This device can perform a high precision straight cut, with an error of 1 μm for a linear translation and of 10^{-2} degrees for rotation. Since the cutting process by the dicing saw damaged the material for a thickness of ≈10 μm along the line of the cut [28, 144], superficial strains and deformations may appear in the sample [145]. Indeed, the dicing process used to shape the crystals causes a damaged superficial layer that is characterized by a large amount of dislocations ($\approx 10^6/cm^2$). Such defects are highly detrimental for the channeling phenomenon, as they can generate a deformation in the crystal that can extend to relatively large distances from the point where the dislocation is generated. Moreover, since the beam would be perpendicular to the damaged surfaces and would pass through them, the particle trajectories would be affected by multiple Coulomb scattering, which eventually leads to a lowering of the channeling efficiency. In order to maximize channeling efficiency of a 7 TeV energy beam, it is estimated that the maximum number of dislocations should not be larger than $1/cm^2$ [146]. Thus, an etching process to remove the part of the crystal rich of defects was performed. The used etching process has been verified to achieve the required dislocation density in [28]. In particular, Rutherford backscattering in channeling condition was used for the purpose, which is a technique to precisely investigate the crystalline quality of the first layers.

In particular, an isotropic etching was performed using a solution composed of 3 parts of HF (50%), 5 parts of HNO_3 (70%) and 3 parts CH_3COOH (99%). This chemical solution is characterized by an etching rate of ≈2μm/min. A ≈100-120 μm thick layer was removed from the cut surfaces. The Si_3N_4 layer was used to protect the rest of the samples during this process. Afterwards, it was removed by a chemical etch based of buffed HF in order to avoid hindrance on interferometric characterization of the surface.

The crystallographic orientation of the main surface of sample 1, i.e. the channeling planes, was chosen to be (110). Sample 2 was designed to have a larger aspect ratio with respect to sample 1. For this sample, (111) plane was selected as the main face.

Sample characterization

Two different characterizations were performed to measure the deformation of the manufactured samples. The first characterization was a morphological analysis of the sample surface. It was performed using an interferometric microscope (Veeco NT-1100). As this instrument allowed to achieve a complete control over the deformation applied on the crystal samples. As the field of view of the instrument is much smaller than the size of the samples, an automated procedure of stitching was performed. This allowed to merge successive measures into a single one by exploiting a 32% overlap.

The morphological characterization of the samples was done before and after the bending process. By comparing the two measurements, it was possible to obtain the displacement induced by the holder, i.e. the curvature of the sample.

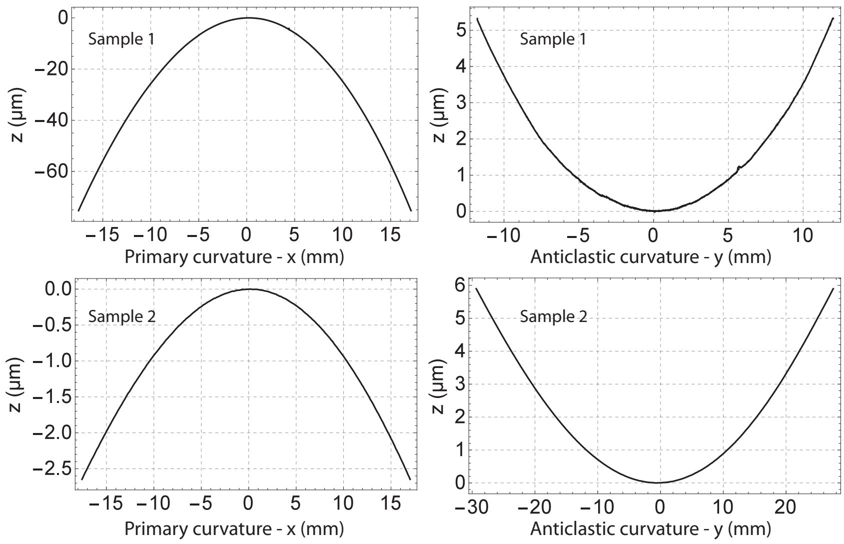

Figure 5.1: Interferometric measurement of the plate crystals. Left column: deformation along the direction perpendicular to particle beam propagation, i.e. the primary curvature—z vs x position. Right column: deformation along the direction of particle beam propagation, i.e. the anticlastic curvature—z vs y position.[147]

The results of the interferometric measurements are shown in Fig.5.1. In particular, the deformation at $y = 0$ is shown in the left column and corresponds to the primary curvature as measured along a line in the centre of the sample and the origin of the reference system is taken at the centre of the sample. The deformation at $x = 0$ is shown in the right column and corresponds to the anticlastic curvature as measured along a line in the centre of the sample, perpendicular to the previous line. As expected, the samples show a saddle-like shape, i.e. the concavity of the anticlastic curvature is flipped wrt the primary curvature.

A quantitative estimation of the curvature was produced from the profiles by calculation of the numerical derivate dz/dy. These derivatives were used for evaluating the average R and ϕ, which are listed in Tab.5.1. The errors are due to the uncertainty of the stitching process of the interferometric microscope.

In order to directly characterize the deformation of the crystalline planes along beam propagation direction, the samples were analysed via a high-resolution X-ray diffractometer (HRXRD) PANalytical - X'Pert^3 MRD (XL). The analysis was carried out with a monochromatic beam of 8.047 keV (Cu $K\alpha_1$). The angular position θ of the diffraction peaks was measured with a 3.5 μrad precision for various adjacent positions along the direction where the anticlastic curvature occurs. The angular shifts of the peaks correspond to the variation of the lattice planes orientation along the sample width, i.e. the angular deflection ϕ that a particle channeled inside the bent crystal would undergo. For these measurements, only the anticlastic deformation was analysed.

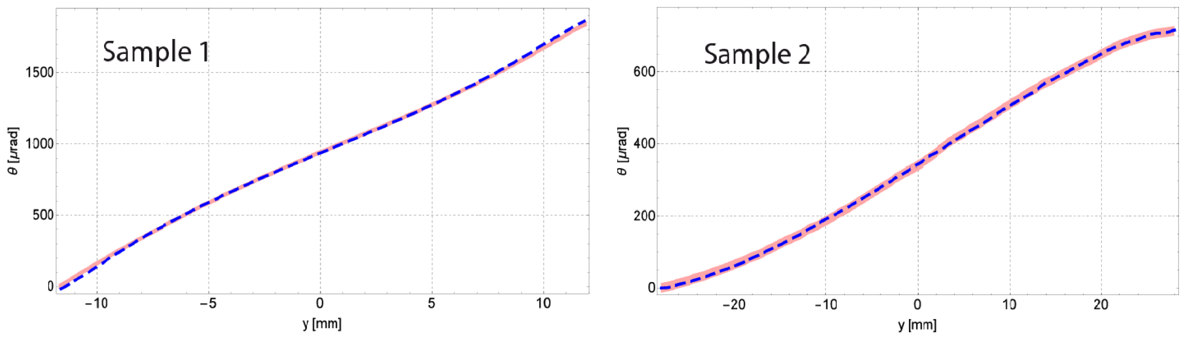

Figure 5.2: X-ray measurement of the anticlastic deformation for the plate crystals. The red stripes represent the peak values θ with the instrument uncertainty. The dashed lines represent the numerical derivative of the corresponding interferometric measurements.[147]

Results of the X-ray characterizations are shown in Fig. 5.2. The measurement results with the corresponding errors are listed in Tab.5.1.

It is worth noting that the two characterizations are compatible within the errors. To underline the compatibility, the numerical derivatives of the two interferometric measurements have been displayed as dashed lines in Fig.5.2. As can be noticed, the dashed lines are in good agreement with the X-ray measurements, thus confirming the characterization results.

Simulations

In order to predict the deflection efficiency of the channeling process in bent crystals, Monte Carlo simulations were carried out using the Geant4 toolkit [148, 149]. The Geant4 channeling package [150] with the addition of the DYNECHARM++ [151] and ECHARM [152] codes was used. DYNECHARM++ makes use of the continuum potential approximation proposed by Lindhard [1] and allows the tracking of a relativistic charged particle inside a crystalline medium via the numerical integration of the classical equations of motion. The code has been validated through experiments performed at SPS with 400

GeV/c protons, as in [42, 45, 153]. The computations of the electrical characteristics of the crystals are carried out via ECHARM. The Geant4 application was developed on top of the 10.3 version of the toolkit, which includes the description of crystalline structures [154]. All physical phenomena occurring for a channeled particle are strongly affected by the number of nuclei and electrons encountered, which depends on the particle trajectory [1]. Therefore, the probability of a physics process to occur in the simulation has been weighted as a function of the density of material experienced by a channeled particle. Such dependence of the probability of interaction allows the correct evaluation of the deflection efficiency, which strongly depends on the particle charge sign [47]. The comparison of the simulation produced with Geant4 and experimental data can be found in the literature for planar [155] and axial [35] channeling, proving to be in good agreement with the respective experimental data and also with the analytical calculations.

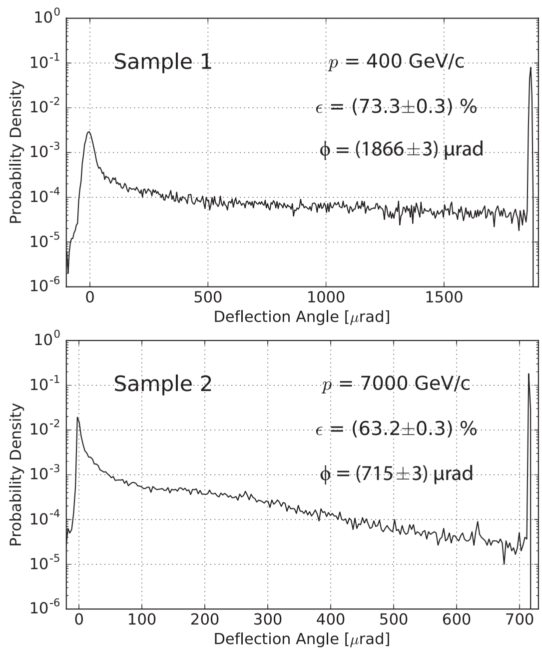

Figure 5.3: Probability distribution of the deflection efficiency as a function of the deflection angle after the interaction with the crystals. The proton momentum (p), the channeling deflection efficiency (ϵ), and the mean deflection angle (ϕ) are indicated on the figure.[147]

The simulation of the interaction in single-pass mode of a collimated beam impinging on the crystals was carried out. In the simulation, a perfectly collimated beam, i.e. with zero divergence, impinged parallel to the main channeling planes. Sample 2 was designed to operate inside the LHC, therefore a 7 TeV/c proton beam was simulated. On the other hand, sample 1 was designed to operate at the SPS energies, thus a 400 GeV/c beam was simulated for this crystal. Fig. 5.3 shows the angular distribution of the particles that exit the crystal after having interacted with it. In the simulation, the crystals were simulated without defects and a negligible experimental uncertainty on the deflection angle is assumed. Sample 1 showed a deflection efficiency under channeling equal to $73.3 \pm 0.3\%$, while sample 2 showed a deflection efficiency equal to $63.2 \pm 0.3\%$. The sample deformation was simulated by using the data from the XRD measurements (from Fig.5.2), considering thus the variation of the curvature radius along the crystal length. The same simulations were worked out also considering a uniform bending curvature (not shown in the figure). For this case, the channeling efficiencies pass from 73.3% and 63.2% to 73.4% and 66.0%, respectively. Such small differences mean that the curvature of the samples was very homogeneous, and the curvature variations weakly affected the channeling efficiency.

Fabrication and characterization of the two Si crystals was carried out successfully, and simulation confirms potentially good steering features, optimized design for extraction of the SPS or LHC beam. A large bending angle was achieved both for the samples 1 and 2, which means that the anticlastic behaviour persists also for large bending and for $L/h > 1$. The Geant4 simulation predicts that a 7 TeV/c proton beam would be deflected by the sample 1 by the channeling effect with a 73.4% efficiency and that a 400 GeV/c proton beam would be deflected by the sample 2 with a 66.0% efficiency. While sample 1 can be used for beam extraction at LHC, sample 2 could be used for efficient extraction at lower energies (like from the SPS [27]) given the smaller radius of curvature. The possibility of obtaining compact crystal deflectors with innovative crystal design has been accomplished and this developed technology could be suitable for a crystal-based extraction in the LHC or in future hadron colliders, such as FCC.

5.1.2 Self-standing curvature

A completely different approach for fabrication of bent crystal for beam extraction can be exploited, discarding both the employment of a metal holder to impose curvature and the use of secondary bending. Indeed, an approach based on self-standing curvature techniques provides several compelling features. These kinds of techniques usually carry out processes on the sample surface to generate a uniform stress which causes the desired deformation. In this case, sandblasting techniques was chosen to produce the samples[156]. The technique purposely induce damage on the superficial layer of the crystal, where an amorphous layer is generated. This create a stress between the machined surface and the rest of the crystal, which induce curvature on the sample. Since channeling requires perfect crystal lattice, the process is performed only on the lateral regions of the sample surface. This leaves the central part of the sample untouched and free of defects (see fig. 5.4).

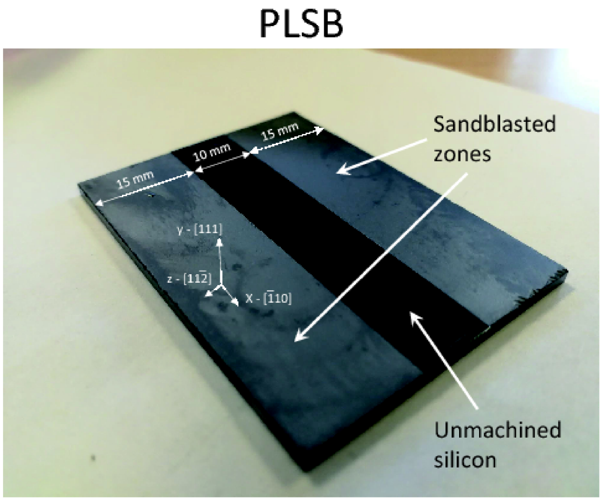

Figure 5.4: Photo of the manufactured samples PLSB. The largest surface of the samples is (111). Sandblasted zones and un-machined silicon zones are highlighted.

The deformation arising from the pattern induce an uniform cylindrical curvature, suitable for channeling experiments. Being the drawback of the lattice damage solved, the sandblasting technique as the great potential of providing a bent crystal composed by a single item. A self-standing curvature can be an advantage for bent crystals to be used for charged particle steering because the cumbersome of an external holder could be a severe limitation for a goniometer in the LHC beampipe. Moreover, the presence of an external holder within the LHC beampipe could affect the accelerator impedance.

The characterization of the samples was worked out through high-energy X-ray diffraction at the beamline ID11 at the European Synchrotron Radiation Facility (ESRF) in Grenoble (France), using a high-energy X-ray beam tuned to 140 keV. The sample curvature turned out to be highly homogeneous, which is essential for high channeling efficiency. Diffraction efficiency observed was in very good agreement with the theoretical expectations, meaning that the crystalline quality was preserved after the manufacturing process. Finally, a rigorous characterization of the crystalline quality in the centre on the sample was verified via topography station at a bend magnet source of the Karlsruhe Institute of Technology (KIT) synchrotron [157], highlighting that the sandblasting process did not

Sample Name	PLSB
Material	Si
Length along the beam	55 mm
Traversed length	40 mm
Thickness	2 mm
Diffracting Planes	(111)
Bending method	Sandblasting
Sandblasted width	15 mm + 15 mm
Unprocessed width	10 mm

Table 5.2: Diffracting planes correspond to main surface 40×55 mm^2. The sandblasting was carried out in the two outer zones of the main surface, leaving intact the central 10 mm

Sandblaster	SAMAC
Compressed air consumption	560 lt/s at 6 bar
Blasting medium	natron glass
Blasting size	1-50 μm
Blasting density	2.3±0.3 g/cm^3
Blasting hardness	6 Mohs
Nozzle-to-sample distance	$\sim$ 10 cm
Process duration	300 s

Table 5.3: table on the right summarize the sample feature, while table on the left indicates the sandblasting process parameters

caused a degradation of the quality of the crystal bulk. Once tested on H8 beamline, the sample showed steering features of a perfect crystal and deflection angle correspondent to the previous characterizations.

Sample fabrication

The Si sample, named PLSB, was manufactured and bent at the laboratories of the National Institute of Nuclear Physics (INFN) of Ferrara. The crystal was made of commercially available pure crystalline Si. First, the sample was shaped to form 55×2×40 mm^3 plate, using the high-precision dicing saw (DISCO^{TM} DAD3220). The largest surface of the samples was (111) oriented, since this crystallographic orientation is characterized by high channeling and diffraction efficiency and well suited for x-rays analysis. Moreover, the high isotropy of the crystallographic orientation would help highlight imprecision during the production process. A sketch of the samples is shown in Fig. 5.4.

PLSB has been bent through the sandblasting method [158]: a mechanical process consisting in driving a stream of abrasive material against a sample through a pressurized fluid, usually compressed air. This technique permits to bend from thin to thick crystals, up to a few mm. The obtained curvature is adjustable and depends on the thickness of the crystal and on the grain of the abrasive material. The parameters of the samples are listed in Table 5.1.2, while the parameters of the sandblasting method are listed in Table 5.3.

For beam-extraction applications, the crystalline quality of the samples should be very high, since lattice defects would affect by multiple Coulomb scattering the particle trajectories, lowering the channeling efficiency [146]. Thus, the sample has been manufactured to have the maximum lattice quality in its central part, where the particle beam should interact with the samples. Indeed, the sandblasted process was applied on lateral portion of the (111) surface of the sample as shown in Fig.5.4. Thus, for both the samples, there is a central part that is constituted only of un-machined Si, and then a channeled particle beam would not cross the crystals near the machined zones, as can be seen in Fig.5.5. In particular, the two machined zones are 15 mm long while the central polished part of the samples extends for all the crystal length (x direction) and it is 10 mm wide.

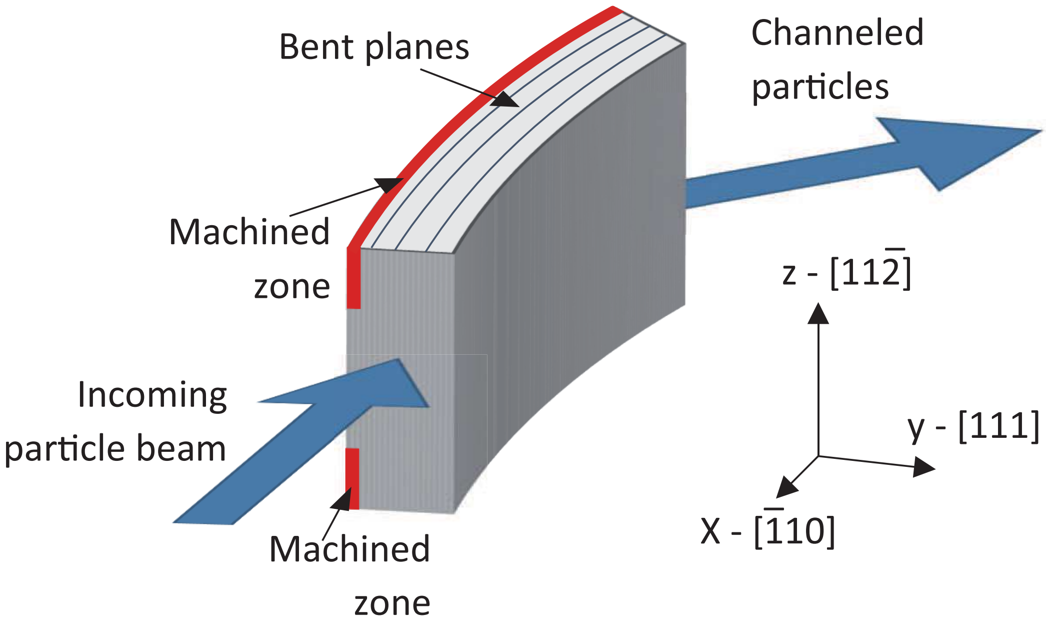

Figure 5.5: Scheme of the manufactured samples. The blue arrows represent the charged-particle beam, while the red zones correspond to the machined parts of material. The curvature of the crystallographic planes is shown.

Both the samples resulted to be bent to the opposite side with respect to the machined surface, i.e. the osculating circle lies on the polished side of the crystal [158]. Thus, the channeled particles, following the crystal curvature, are deflected in the opposite direction from the machined surface.

High-energy X-ray diffraction

The curvature of the sample was tested through high-energy X-ray diffraction at the beamline ID11 of ESRF. A highly monochromatic and quasi-parallel beam was tuned to 140 keV energy. Monochromaticity was of the order of $\Delta E/E = 10^{-3}$. The beam was $50{\times}50$ μm^2 wide. The beam diffracted on the (111) planes traversing the sample length, i.e. in Laue geometry, and entered the crystals in the centre of one of their (110) surfaces. Thus, for the sample PLSB, the beam entered the centre of one of the $40{\times}2$ mm^2 surfaces and traversed 55 mm of Si, Therefore, the characterizations were worked out with the high-energy X-ray beam that followed the same path that a channeled beam would do, as shown in Fig.5.5.

The characterization of the sample was carried out by performing rocking curves (RCs), i.e., by recording the transmitted and the diffracted beam intensity while the crystal was being rotated around the position where Bragg condition was satisfied. In particular, the Bragg angles were 14.12 mrad for both the (111) planes. The sample was set far enough from the detectors to allow sufficient separation of diffracted and transmitted beams.

Diffraction and transmission RCs were recorded simultaneously by two identical photodiodes, resulting in two complementary curves as a function of the beam glancing angle. The experiment parameters are listed in Table 5.1.2 and Table 5.4, while the experimental results are shown in Fig. 5.6. Beam divergence, beam flux, acquisition time, and beam size were taken into account to normalize the photon counts. In particular, the photon counts have been normalized to 1 taking into account the flux that hit the detector when the sample was not aligned for diffraction. Thus, the absorption is not included in the figure both for the transmitted and for the diffracted beam. Given the high flux of the ID11 beamline, the measurements took only a few minutes.

The full width at half maximum (FWHM) of the RC turns out to be a direct measurement of the angular distribution of diffracting planes Ω, i.e. the bending angle of the crystal. The RCs also exhibit diffraction efficiency of the sample under analysis. The diffraction efficiency is a good estimator of the crystalline quality of the samples. Indeed, if the measured diffraction efficiency is equal to the theoretical value, it means that the crystalline quality was preserved, namely the bending process did not damage the samples. This is mandatory to obtain high-efficiency channeling.

The theoretical value for the diffraction efficiency (η) is given by the following formula as a result of the dynamical theory of diffraction [159]:

$$\eta = [1 - e^{\frac{-\pi^2 T_0 d_{hkl}}{\Omega \Lambda_0^2}}], \tag{5.1}$$

where T_0 is the crystal thickness traversed by radiation, d_{hkl} the d-spacing of planes (hkl), Λ_0 the extinction length as defined in [160] for the Laue symmetric case, and Ω represents the bending angle of the curved diffracting planes. The values for d_{hkl} and Λ_0 are listed in Table 5.4.

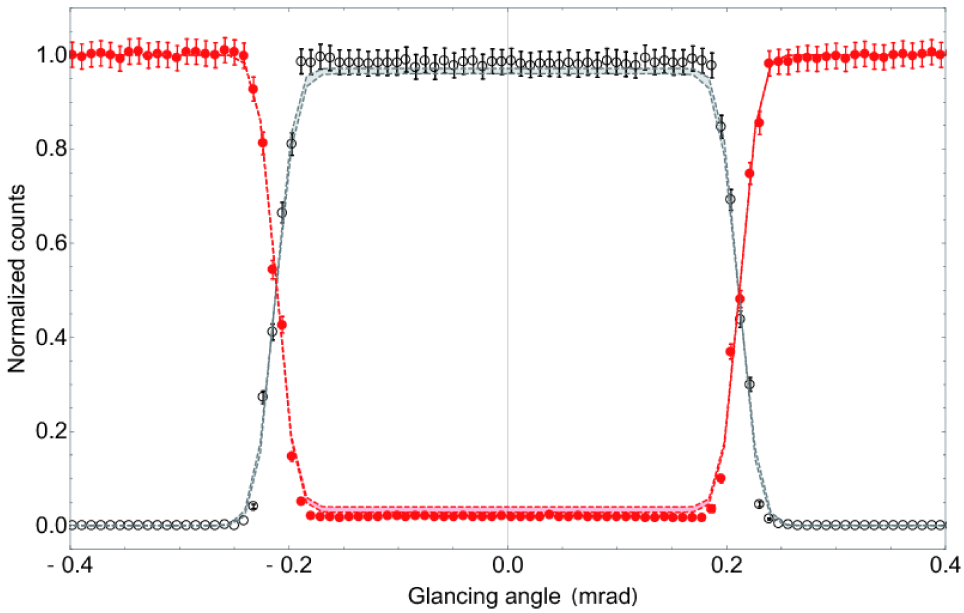

Figure 5.6: Experimental RC for a 140 keV X-ray beam. Angles are relative to the nominal angle for diffraction. The nominal angle at which the diffraction occurred was set at 0 mrad. Solid red dots correspond to the intensity of the transmitted beam, whereas black rings correspond to the intensity of the diffracted beam, as a function of the glancing angle of the incoming high-energy X rays. Dashed lines represent the corresponding theoretical values with the uncertainties.

The angular spread Ω depends on the radius of curvature R of the diffracting planes. For the measured samples, T_0 that enters into Eq.5.1 is the crystal side, i.e. 55 mm for the sample PLSB. Since the obtained values for Ω are 0.424 mrad for PLSB, it follows $R = T_0/\Omega \approx 132$ m. All the results are listed in Table 5.4. The outcomes of the X-ray measures were obtained by fitting the intensity of the diffracted (and transmitted) beam acquired at each position.

Beam Energy [KeV]	140
Energy Spread [ΔE/E]	$\approx 10^{-3}$
Beam Size [μm$\times\mu$m]	50×50
Sample	PLSB
D-spacing for (111) planes [Å]	3.1355
Extinction length Λ [m]	$3.43 * 10^{-4}$
Angular spread [mrad]	0.424
Curvature radius [m]	130
Diff. efficiency - theoretical	0.97±0.01
Diff. efficiency - experimental	0.98±0.01

Table 5.4: X-ray beam parameters and experimental results on x-ray characterization of the sample

Fig.5.6 shows also the theoretical expectation for the measured RCs, which are plotted with dashed lines. In particular, calculations were carried out by taking into account a perfectly homogeneous curvature. As can be noticed, the experimental data are in very good agreement with the expectations, meaning that the crystal curvature was homogeneous and the crystalline quality was preserved. In particular, analytical calculation was worked out taking into account a tolerance on the crystal curvature of ±1%. The tolerance is visible in the figure as a grey or red band within two dashed lines.

X-ray white-beam topography

Since the sandblasting process could in principle cause a damage in the crystal bulk, further characterization of the lattice quality was carried out. X-ray white-beam topography (XWBT) was applied to PLSB, using the topography station at a bend magnet source of the KIT synchrotron [157]. The method allows imaging of the spatial distribution of strain localizations within crystalline bulk materials with a few micrometer spatial resolution, thus enabling the detection and identification of crystal defects like dislocations, inclusions, etc.

In general, XWBT employs a parallel and polychromatic X-ray beam, which impinges the sample and generates a Laue pattern, with each spot resulting from diffraction by an individual set of net planes *hkl* within the illuminated crystal volume. Since any local strain within the investigated sample volume influences the local diffraction conditions, imaging contrast is created in the intensity distribution of the diffracted beam cross-sections: for each reflection *hkl* characteristic diffraction properties of the crystal are projected along the corresponding diffracted wave vector into the corresponding topography [161]. Digital high-resolution X-ray imaging detectors allow many of these topography to be recorded, even with high frame rates, enabling e.g. time-resolved studies [162, 163].

Exploiting a wide incident X-ray beam, motorized sample translation, and fast digital image acquisition, XWBT allows two-dimensional (2D) large area screening of laterally extended samples (e.g. covering complete industrial wafers) [164]. During data processing, the recorded image tiles are merged, yielding a high-resolution 2D overview map of the defect distribution.

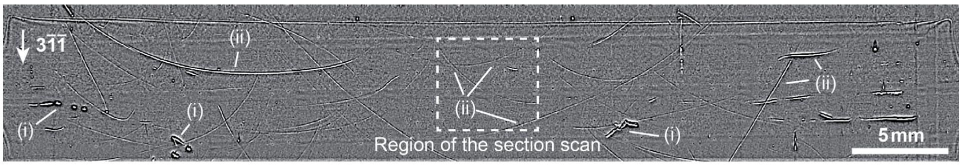

Figure 5.7: Non-machined central stripe of PLSB, imaged by XWBT large area screening (contrast digitally enhanced), with two types of features marked exemplarily. Type (i) is interpreted as localized impression damage at the surface and, supported by the 3D information in Fig.5.8, type (ii) can be related to scratches.

A particular variant of XWBT, commonly referred to as section topography, takes advantage of a slender incident X-ray beam, narrowed in one direction to only few tens of μm. As a result, the projection of the thin illuminated volume slice in the diffracted beam direction provides depth information [164]. By suitable step-wise sample translation, a sequence of such cross-section images can be recorded, gradually sampling the three-dimensional (3D) sample volume and enabling the reconstruction of a 3D image by virtual stacking [165].

Two large area screenings of the complete sample PLSB were performed using the $0\bar{2}2$ and $3\bar{1}\bar{1}$ reflections (see Table 5.5), complemented by a 3D section scan of one selected region of interest (see Table 5.6). All topographic images were digitally recorded by an indirect detector system consisting of a 200 μm thick LuAG:Ce scintillator crystal coupled by magnifying visible light optics (Nikkor 180/2.8 ED objective) to a pco.4000 Charged Coupled Device (CCD) camera (4008×2672 pixels), resulting in an effective pixel size of 2.5 μm [162].

One of the obtained large area overviews (the one using the $3\bar{1}\bar{1}$ reflection) of the non-machined central stripe of PLSB is shown in Fig.5.7. After digital background correction and contrast enhancement, homogeneous gray color indicates perfect crystal regions, while strain localizations are visible as black and white contrast. Two classes of features are distinguishable: Type (i) is confined to small areas, occasionally even appearing point-

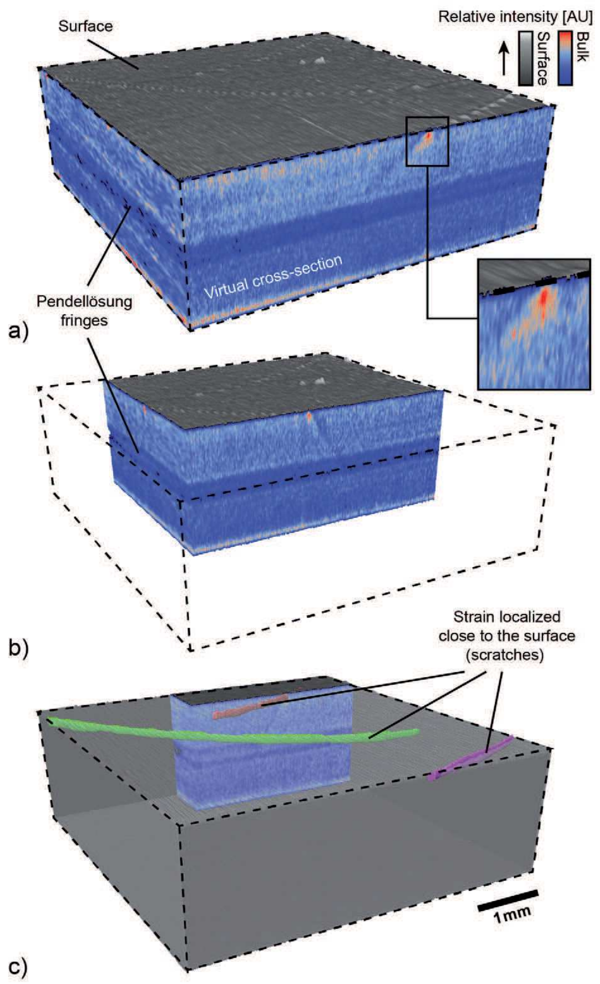

Figure 5.8: Visualization of the 3D topographic contrast distribution in the region marked in Fig.5.7, recorded by XWBT section scanning. As shown in the different cross-sections through the complete sample thickness in a)-c), the origin of type (ii) contrast features appears located close to the surface, which suggests that these feature correspond to scratches.

like. By comparison with studies of controlled mechanical surface indentations [166] this feature class is attributed to localized impression damage, e.g. by sufficiently hard particles pressed onto the surface during sample processing or handling. Type (ii) appears as sharp lines, extended up to several millimeters and predominantly resembling smooth arcs. Since dislocations in silicon are well known to have a tendency towards straight-line segments [167], and because the typical features of dynamical diffraction contrast of dislocations (intermediary image fringes, one-sided blurred dynamical line edges [160]) are not visible here, the appearance of type (ii) features can be attributed to scratches at the surface.

Reflection	$0\overline{2}2$	$3\overline{1}\overline{1}$
Bragg angle (Degree)	10°	7.025°
Energy (keV)	18.59	30.95
Beam size, w×h (mm^2)	6×4	6×4
Exposure time (s)	2	5
Number of tiles	150	132

Table 5.5: Parameters of the XWBT large area screenings

Reflection	$3\overline{1}\overline{1}$
Bragg angle [°]	7.025°
Energy [keV]	30.95
Beam size, w×h [mm^2]	8×0.03
Step size [μm]	80
Exposure time [s]	30
Number of steps	150

Table 5.6: Parameters of the XWBT section scan

This reasoning is strongly supported by the 3D distribution of topographic contrast recorded by section topography scans: the illustration in Fig.5.8 shows that the contrast of all type (ii) features in the investigated region originates exclusively from crystal regions close to the surface. Moreover, the strong manifestation of Pendellösung fringes visible in the centre of the cross-sections indicates very high perfection of the crystal lattice in the bulk [160].

5.1.3 Test beam at H8

The sample channeling features were directly studied at H8 beamline of CERN. The experimental layout of the particle tracking system is the same used for the study of LHC collimation, as well as the beam parameters. The investigation was carried out on June 2017, during UA9 beam time. Steering of pion beam was clearly observed, with channeling efficiency reaching up to 37±0.1% for particles aligned within 5 μrad. The main hindrance to beam steering was given by the length of the crystal. Indeed, for 180 GeV π^+ scattering with electrons in the channel is the main source of dechanneling within the crystal. Indeed, dechanneling length is of the same order of magnitude at the energy used. While for 7 TeV protons of LHC the length of the crystal would be less than a tenth of it, thus allowing a more persistent channeling condition.

The deformation was obtained via the sandblasting turned out to be homogeneous throughout the samples. In particular, the sandblasting method should permit to obtain the maximum homogeneity of the curvature. High-energy X-ray characterization was worked out through RCs. In particular, the FWHM of the RCs is the measure of the radius of curvature of the samples. Moreover, the measured RCs attested that the sample curvature were homogeneous, since The RCs showed a flat-top profile. Indeed, the diffraction

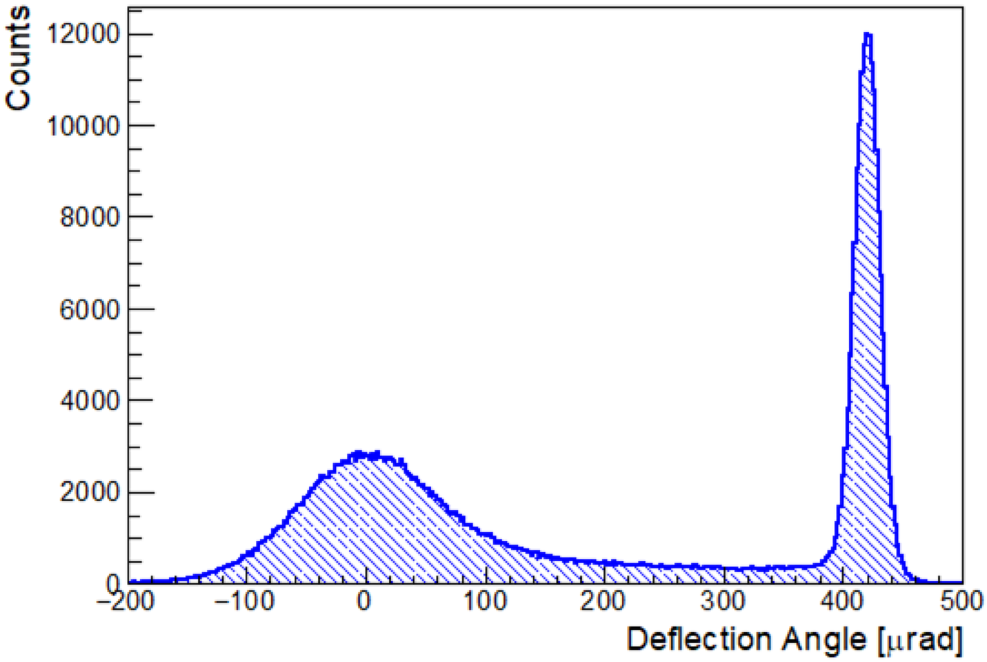

Figure 5.9: plot of the particle deflection after the crystal. The peak of particles deflected by 419 μrad indicates the channeled pions which travelled all the length of the crystal, resulting in a deflection equal to its bending

efficiency η depends on the local curvature radius R of the samples. Since the theoretical expectations are in good agreement with the recorded RCs, it can be deduced that the crystalline quality of the samples was preserved, thus no defects were introduced during the manufacturing process. Channeling with charged particles is mandatory to attest that the crystallographic quality was preserved enough to permit high-efficiency channeling and thus efficient beam extraction. The test performed at H8 confirmed the preservation of a perfect lattice along the beam path, thanks to the patterning of the machined surfaced performed in order to avoid the central area of the sample.

The recorded values for the radius of curvature were 130 m. These are good values for channeling experiments, in particular for steering of the 7-TeV beam of LHC [147]. In principle, the fine adjustment of the curvature of the samples can be obtained by varying the parameters of the manufacturing techniques [158]. Indeed, an appropriate choice of the bending radius and the absence of crystalline defects are the key ingredients for the fabrication of a crystal capable of efficient deflection of high-energy charged particle beams.

Following this test, the thermal stability of the crystal has been tested. The heating

Angular cut on incoming angle	Deflection Angle	Efficiency ($\pm 3\ \sigma$)
5 μrad	419$\pm$2 μrad	37.1$\pm$0.2%
7.5 μrad	419$\pm$2 μrad	35.4$\pm$0.2%
10 μrad	419$\pm$2 μrad	33.1$\pm$0.2%
15 μrad	419$\pm$2 μrad	28.2$\pm$0.2%

Table 5.7: Tables indicating the channeling deflection and efficiency measured selecting from the acquired data only the portion of beam within the indicated angular divergence

cycles performed to simulate the LHC beampipe bake-out process. The sample curvature was measured via x-rays diffraction with the high-resolution diffractometer in Ferrara laboratories after each cycle. Within the instrumental resolution, no difference has been observed after repetition of 3 cycles.

The stability of the machined layer phases was also empirically verified, as routine measurements in the following years showed no difference in bending condition. As for practical operation, the crystal should last at least a year to allow switching with new one during the annual maintenance.

The technique is promising, the size of the fabricated samples can be easily rescaled to adjust the desired length of the crystal deflector, as the curvature is dependent only on the sample thickness (2 mm for PLSB) and is not influenced by width and length. Hence a sample 100 mm long, as desired for the Crysbeam project, would be of feasible production.

5.2 Crystal Assisted EDM and MDM studies

The electric and magnetic dipole moments are static properties of fundamental particles. EDM is an extremely sensitive tool to investigate new physics[168]. Indeed, QED calculations strongly suppress contributes from standard model making effects from new physics are particularly evident. Enhancement of EDM would be inevitably linked to undiscovered CP violation mechanism, thus enabling the development of new models. MDM in baryons derives from their internal quark structure. Investigation on MDM thus allows important anchor points to support QCD quark model. Experimental studies on these quantity exploits the influence over the particle spin precession in an external electromagnetic field. For particles like proton, neutron, muon and electron, such measurements provide among the most stringent tests of the SM [169–175]. However, there are currently no direct measurements of such properties for charm and beauty baryons, and also for τ leptons, due to the difficulties imposed by their short lifetimes. Indeed, current state of art magnetic dipole are not powerful enough to manipulate spin state before the decay of the particle. On the other hand, the internal fields of crystal lattice largely overcome artificial ones. A bent crystal can induce spin precession similarly to a magnetic dipole to channeled particles. In few centimetres is possible to obtain precession equivalent to hundreds of Tesla dipole, allowing measurable spin precession even in fast decaying particles.

SELDOM proposes employment of bent crystal for the investigation of strange and charmed baryons at LHC. In particular, it is proposed to exploit LHCb detectors in parasitic mode. This can be accomplished by splitting the beam halo $\approx$ 100 m upstream the detector, in order to operate without obstructing the primary beam. The strange and charmed baryons are produced by the particles deflected from the first crystal colliding into a tungsten target placed right before the LHCb detector. Attached to the target, a bent crystal collects the produced particles and induces spin precession. The particles are produced with polarized spin, the final state of the spin can be reconstructed analysing the decay.

This configuration requires a careful design of the two bent crystal. The first acts similarly to a LHC crystal collimator, only imposing a larger angular kick of 150 μrad in 12 mm. The second one is much different, both in length and in radius of curvature. Indeed, in order to be detected by LHCb detector, particles must be deflected by at least 14 mrad. While in early channeling experiments even larger deflection were achieved, the efficiency of the deflection was extremely low (0.01-1%). This was attributed to several factors, one being the low quality of the bending. Indeed, variation of radius of curvature along the trajectory of the channeled particle can lead to enhanced dechanneling. It is

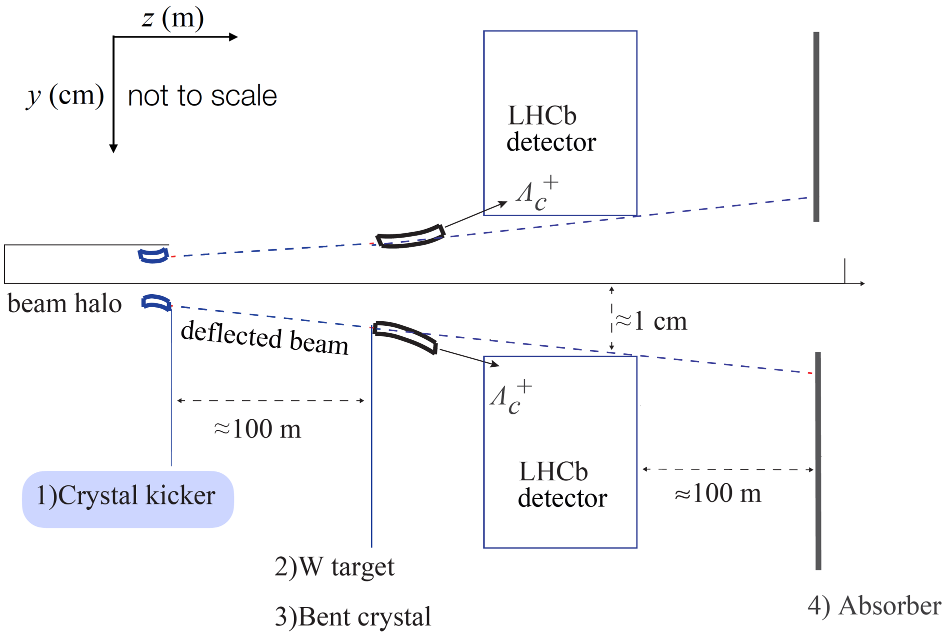

Figure 5.10: SELDOM proposed setup for experiment at LHCb [176]

critical to provide bent crystal perfectly shaped, in order to maximize steering efficiency and consequently the experiment statistic. Two prototypes were tested on H8 beam line at CERN, in order to verifying the feasibility of such samples.

5.2.1 Crystal for precession

Crystals have been produced through a revisiting of a protocol [28, 50] already used to manufacture crystals used for the steering of circulating particle beams at the LHC [51]. The prime materials were a 5 mm thick (111) oriented Silicon wafer and a 1 mm thick (110) oriented Germanium wafer. Germanium is a semiconductor with the same lattice type of Silicon and diamond, but it has stronger continuous potential thanks to its heavier nuclei. This feature is critical for SELDOM as it leads to larger angular acceptance of channeling phenomena and smaller critical radius of curvature. A bent Germanium crystal can thus be a more powerful and efficient beam manipulator than a corresponding Silicon one. One of the drawback of Germanium is its smaller availability with respect to Silicon, especially when high standard of lattice quality is required. Crystalline defects are indeed an issue, as they can be detrimental to the steering efficiency [16, 177]. Therefore, wafers with a dislocation density lower than 1/cm^2 over the entire region interacting with the particle beam were selected from a stock of wafers. The density of dislocations was characterized through the etch pit density [178, 179] and the x-ray topography techniques. For both samples lattice quality was reached.

The wafers physical surface is parallel to the lattice plane within some uncertainty. A miscut angle is then characterizing this imperfect parallelism and to ease the crystal alignment to the particle beam the crystal miscut should be minimized. The wafers miscut angle has been measured via high-resolution X-ray diffraction and then lowered to less than $170\mu rad$ along any direction through chemo-mechanical polishing. Mechanical dicing was then applied to the wafers to obtain a 80×50×5 mm^3 Silicon crystal and a 55×35×1 mm^3 Germanium crystal. The geometry of the samples and the small radius of curvature made previously employed bending configuration unusable. Indeed, anticlastic curvature would be strongly suppressed (for previous extraction prototypes, much larger radius of curvature was applied) while self-standing techniques such as sandblasting achieve much smaller curvatures. This first approach employed mechanical banding imposed from a metal holder, not to generate secondary elastic reaction but to directly induce the desired bending radius. Mounting surfaces and metal clamps are shaped in order to follow a nominal bending radius, the crystal once fixed is thus expected to adapt to the holder shape (see Figure 5.11). Assemblies describing crystal holder were tested through finite element modelling (Ansys R18), and the shape of the surface in contact with the crystal were properly designed to maximize uniformity of the deformation of the crystal. The metal components were manufactured through milling and electro discharge machining of a block of stainless steel 316LN. This material was chosen for its compatibility with the environment of LHC, where we aim those devices to operate. For Silicon a 5.0 m radius profile was machined, corresponding to an expected deflection angle of the beam of 16 mrad, For Germanium the profile was 3.8 m leading to a total 14.5 mrad (see Figure 5.11). The uniformity of the crystal deformation plays a key-role to obtain the expected steering efficiency: to enhance uniformity of crystal curvature, the nominal shape of the surfaces of the holder in contact with the crystal have been optimized through finite element models to free-form surfaces and surfaces in contact with the crystal machined with ultra-precise techniques. Mounting was performed in clean room environment to avoid dust particles to hinder optimal contact between sample and holder. The holding clamps were tightened with dynamometry torque to 80 cN×m.

After bending, crystal deformational state was characterized by means of a high-resolution technique using X-ray diffraction of an 8.04 keV X-ray beam (Panalytical X'Pert^3 MRD XL). Rocking Curves were obtained along the whole sample length (80 mm for Si,

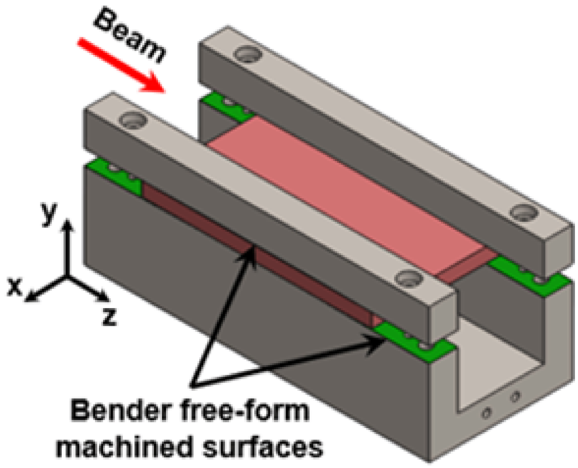

Figure 5.11: Sketch of an assembly made of crystal (red part) and associated holder (grey parts). Surfaces in contact with the crystal (green color) have been machined to a free-form surface. As the crystal is clamped in the holder, it warps around the x-axis. A particle beam, initially propagating along the z-axis is channeled between bent atomic planes and deflected.

55 mm for Ge) at distance of 1 mm. X-ray characterizations showed a bending angle of 16.1±0.8 mrad for the Silicon crystal, and of 14.5±0.8 mrad for the Germanium one.

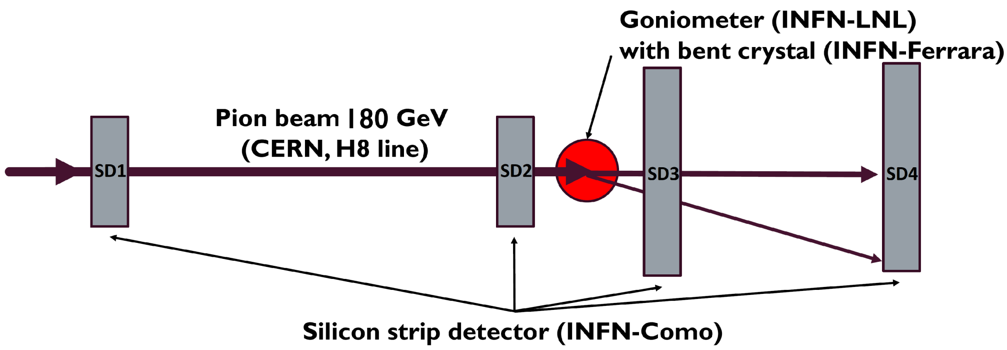

Figure 5.12: Sketch of the experimental setup at the CERN H8 line. A 180 GeV pion beam is directed to the crystal. The trajectory of each particle of the beam is reconstructed before and after the interaction with the crystal by a tracking telescope (grey boxes). The crystal (red rectangle) is mounted on a high-resolution goniometer (blue circle). As the crystal is oriented in order to channel the incoming beam between its atomic planes, beam steering occurs and a fraction of the beam is deflected (green arrow). Distances between elements of the setup are expressed in mm.

At the external beam line H8 of the SPS (CERN) each crystal/holder assembly was mounted on a MICOS high-precision goniometer, composed by different stages. Two linear and two rotational movements with the possibility to align the crystal in either horizontal (x) or vertical (y) directions, were used.

All the stages are equipped with two-phase microstep motors and mechanical limit switches are integrated in the two linear stages [59]. The linear stages and the two goniometers are equipped with a feedback mechanism, i.e., are read continuously by the electronic equipment and are constantly corrected to obtain the desired position through a feedback mechanism. The horizontal-rotational stage, which provides rotation around the Y-axis, has an angular range of 360°. The other rotational stage is more properly a cradle and varies the angle around the X axis with a limited angular range of about 9×10^3 μrad. Both the two goniometers have an accuracy of 1 μrad. By means of the DAQ system, the motor positions are stored in the data files.

Deflection was measured by tracking the particle trajectory before and after the crystal through a telescope system of 4 double-sided silicon microstrip detectors (SDi in Fig. 5.12). The SDi were developed by INFN of Como. Each of them consists in a box (12×12 cm^2 and 4 cm thick) formed by a double-sided silicon strip detector (1.92×1.92 cm^2, 300 μm thick) and its frontend electronics. Each SDi is composed by two sides, p-side and n-side; the first one has a p^+ implantation strip every 25 μm, while the other one (perpendicular to the p-side) has a n^+ implantation strip with a pitch of 50 μm. The incoming and the outgoing angles of particles with respect to the crystal orientation have been determined by using information acquired from the detectors SD1-2 and SD3-4, respectively. The deflection angle was thereby obtained as $\Delta\theta = \theta_{out} - \theta_{in}$.

The usage of double sided microstrip detectors has several advantages:

- good intrinsic spatial resolution both in the horizontal and in the vertical direction (δx $\approx 6.4\mu rad$ for p-side and δy $\approx 10.5\mu rad$ for n-side)
- limited amount of material ($\approx 300\mu$m each module) along the beam to reduce the contribution of multiple scattering and background radiation, thus limiting the errors in the spatial and energy resolutions
- simplicity and versatility in their installation due to their compactness

Once the tracking system was installed, the crystal entry face was aligned to a 180 GeV hadron beam in order to channel the particle beam between bent atomic planes of the crystal. The beam divergence (26 μrad) resulted to be wider than the critical angle for channeling at this energy ($\sim$10 μrad) and also the dimension along the y direction

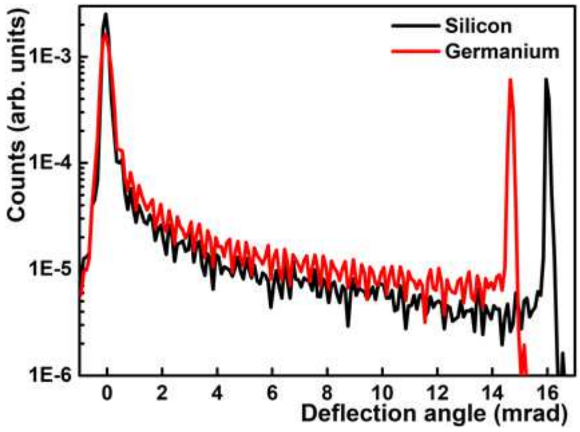

Figure 5.13: Angular distribution of the beam after interaction with the Silicon crystal (black curve) and Germanium crystal (red curve). The maxima located on the right side of the plot corresponds to particles which were deflected being channeled over the entire crystal length. By selecting only particles impinging on the crystal within the critical angle for channeling, we record steering efficiencies of 8.9% for the Silicon crystal, and 10.8% for the Germanium one.

($\sim$ 8 mm) was larger than the geometrical size of the crystal. Therefore, to select particles geometrically intercepted by the crystal and impinging on bent atomic planes with angles comparable to the critical angle for channeling, a tracking telescope based on two micro-strips detectors placed before the crystal and two after were used to reconstruct particle trajectories before and after the interaction with the crystal. Through Monte Carlo simulations carried with Geant4 and analytical estimates, we evaluated that the telescope reconstructs particle trajectories with uncertainty of $\sim$7 μrad before interaction with the crystal and of $\sim$50 μrad after the interaction.

Figure 5.13 shows the angular distribution of the beam after the interaction with the crystal as it is aligned in order to excite channeling of the beam. Only particles impinging on the crystal within the critical angle for channeling are selected.

The peak of the distribution on the left is populated by particles which were not channeled between atomic planes at the crystal entry face [77] and by particles which were initially channeled but with an impact parameter with respect to atomic planes smaller than the thermal vibration amplitude of the atoms of the crystal. For such particles events of single scattering with inner shell electrons of atoms or with atomic nuclei results in a drastic change of their trajectory, leading them out of channeling regime soon after being channeled [43]. The peaks of deflected particles are centred at angles of 15988$\pm$5 μrad and 14670$\pm$2 μrad for the case of Silicon and Germanium crystals respectively. For the

	Germanium	Silicon
Transverse thickness [mm]	1	5
Thickness along the beam [mm]	55	88
Deflection angle for X rays [mrad]	14.5±0.8	16.1±0.8
Deflection angle for channeling [mrad]	14.670±2	15.988±0.8
Measured steering efficiency	10.78±0.05%	8.9±0.1%
Simulated steering efficiency	12.3±0.1%	9.9±0.1%

Table 5.8: Geometrical parameters of Silicon and Germanium crystals used in the experiment and recorded channeling efficiencies compared to expected from Monte Carlo simulations.

case of the Silicon crystal, the beam contains a fraction of 8.9±0.1% of the total particles, while for Germanium the peak subtends a fraction of 10.78±0.05%. Between the peak of successfully steered particles and the peak of particles that never underwent channeling, the particle population is characterized by dechanneling phenomena. This effect is characteristic of particles being initially channeled, but with impact parameter wider than the thermal vibration amplitude of the atoms of the lattice. As result of multiple scattering with valence electrons, whose magnitude is considerably smaller than magnitude of scattering on inner shell electrons or atomic nuclei, such particles left channeling state in the crystal bulk. Their trajectories did not follow the entire length of the crystal, and thus obtain a deflection lower than the one reached by particles travelling the entire sample. It is worth noting that the region between the two peaks does not show any intermediate peak. That is a clear indication of a crystal with of uniform curvature: non-uniformities of the deformation of the crystal would lead to the de-channeling of the particles localized at the regions of stronger local curvature.

The particles composing the beam are indeed of lower energy A selection of the particles impinging on the crystal within the critical angle for channeling allows to define the steering efficiency of the crystal, Table 5.8 summarize the most important features of the tested crystals and the recorded performances in terms of steering efficiency.

Monte Carlo simulation were carried out to simulate a perfect crystal with same curvature of the two tested sample. The results obtained are in fairly good agreement with the experimental data.

5.2.2 Simulations

Monte Carlo simulation was performed in order to calculate the expected channeling efficiency for a perfectly bent crystal.

To get information related to channeling efficiencies at higher energies with respect to the one available for this experiment, the same simulation approach [180, 181] was used to estimate channeling efficiency as a function of particle beam energy (Figure 5.14).

The simulation recreated a beam with uniform angular distribution of width equal to two times the critical angle for channeling impinging the lattice planes. The strange and charmed baryons produced in the final experiment will have angular divergence ≈100 times larger than the critical angle, thus such approximation should describe well the real situation. Particles impinging the crystal at larger angle should have negligible effect on the final channeling efficiency result, as shouldn't be trapped into the potential. Once particles exit the crystal, the channeling efficiency is calculated by confronting the number of particles still in channeling at the end of the crystal with the total beam population. It is worth noting that the Germanium crystal has a thickness which is about 69% of the thickness of the Silicon crystal, while the bending angles are similar. This results in a smaller bending radius for the Germanium crystal, despite this efficiency of Germanium crystal is slightly higher in the range of energies of interest for the experiment. Reducing the length of the bent crystal is a key factor for increasing statistic of the experiment, since particles inevitably decay

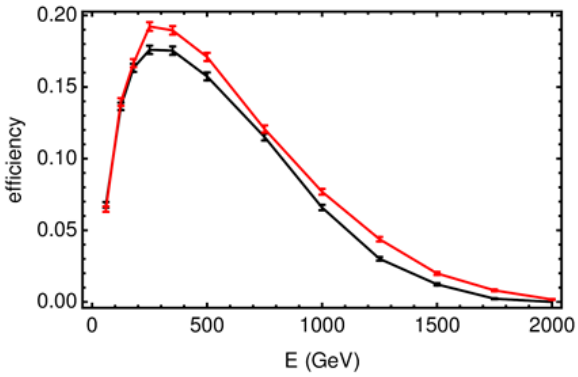

Figure 5.14: Dependence of channeling efficiency on beam energy. In the simulations we assumed a beam with a uniform angular distribution of width equal to two times the critical angle for channeling. Red curve for the Germanium crystal, black for Silicon. In both cases we considered a crystal with the same geometry of the crystals described in the text.

Chapter 6

Coherent Effects in Axially Aligned Heavy Elements

Since their discovery, scintillator materials have played an important role in nuclear and particle physics, as well as in medical and industrial imaging. In particular, inorganic scintillator crystals are widely exploited for the realization of homogeneous electromagnetic (e.m.) calorimeters for high-energy physics (HEP) and astrophysics [182, 183], to measure the energy of $e^{\pm}$ and of γ-rays. The process of energy measurement via e.m. calorimeters is related to the e.m. shower development with generation of secondary particles, consisting in a long chain of events of γ emission by $e^{\pm}$ and $e^{+}e^{-}$ pair production (PP) by γ. Scintillation light produced by the passage of particles is proportional to energy deposited inside the crystal and is collected by photo-detectors. In order to measure the initial particle energy, the whole shower should be contained in the detector. Since for primary particles of multi-GeV or TeV energies the shower results to be ten or more radiation lengths (X_0) long, high-Z scintillator crystals (e.g., BGO ($Bi_4Ge_3O_{12}$), CsI, and PWO ($PbWO_4$)) with X_0 of about 1 cm have been introduced to realize compact calorimeters. Despite these materials are crystalline, the lattice influence on the e.m. shower is usually completely ignored both in detector design and simulations. On the other hand, it is well known since 1950s that the crystal lattice may strongly modify both γ emission by $e^{\pm}$ and PP by γ, thus accelerating the e.m. shower development.

Indeed, for small angle between charged particle trajectory and crystal axes/planes direction, successive collisions of the particles with the atoms in the same plane/row are correlated and it is possible to replace the screened Coulomb potential of each atom with an average continuous potential of the whole plane/string [1], corresponding to a strong electric field $E \sim 10^{10} - 10^{12}$ V/cm [58, 184]. The continuous potential approximation remains valid within incidence angle $\psi < V_0/m$ [58].

At even higher energy, the average electric field felt by a particle in its rest frame is enhanced by a factor γ because of the Lorentz contraction, thus becoming comparable to the Schwinger critical field of QED, $E_0 = m^2c^3/e\hbar = 1.32 \cdot 10^{16} V/cm$, which is rarely reached in nature only in extreme environments such as pulsar atmosphere, neutron star, supernovae and black holes. In laboratory Schwinger limit is reached even more rarely, such as in light-by-light scattering in lead-lead ions collisions at LHC [185]. This *strong field* regime is characterized by quantum synchrotron radiation with intense hard photon emission by $e^{\pm}$, as well as by intense PP by high-energy photons [184]. The *strong field* limit is attainable in crystals if the $e^{\pm}/\gamma$ beam energy reaches tens/hundreds of GeV, when the parameter $\chi = \gamma E/E_0$ is ~ 1.

The huge enhancement of radiation and PP processes caused by the *strong crystalline field* was predicted by the authors of [58, 184, 186, 187] and observed at CERN and IHEP since middle 80s with the usage of single crystals of diamond, Si, Ge, W, and Ir [188–192]. The main consequence of these effects was the acceleration of the e.m. shower development, which resulted in a strong reduction of the shower length and thereby of the radiation length, X_0, in comparison with amorphous materials (or equivalently randomly-oriented crystals).

Since high-Z crystal scintillators are widely exploited in e.m. calorimeters for HEP, it became rather important to investigate the *strong field* influence on the e.m. shower development in these materials. The only previous study in this direction was carried out about 20 years ago with oriented garnet and lead tungstate crystals at intermediate electron energy (26 GeV, corresponding to $\chi \simeq 1$), which resulted in a limited increase in energy loss of about 10% of the beam energy as compared to random orientation [193]. The authors claimed the importance to further investigate such processes at higher energies (about hundreds-GeV or TeV), where the strong field effects would become more important and at which current and future HEP experiments would work. The need of a full Monte Carlo code to simulate the e.m. shower development in oriented crystals was also highlighted.

The research carried out in this thesis is focused on lead tungstate (PWO). PWO is widely employed as inorganic scintillator thanks to its extremely fast scintillation time (6 ns). Furthermore, PWO is one of the most efficient in containing e.m. showers thanks to its small radiation length (0.89 cm) and molière radius (1.959 cm). Such features partly derive from its dense structure and heavy elements (W, Pb) composing it. In particular, crystallographic characterization and investigation of axial effect with ultrarelativistic particles were carried out on a single crystal PWO strip 2×4×55 mm^3, with corresponding orientations [100]×[001]×[010].

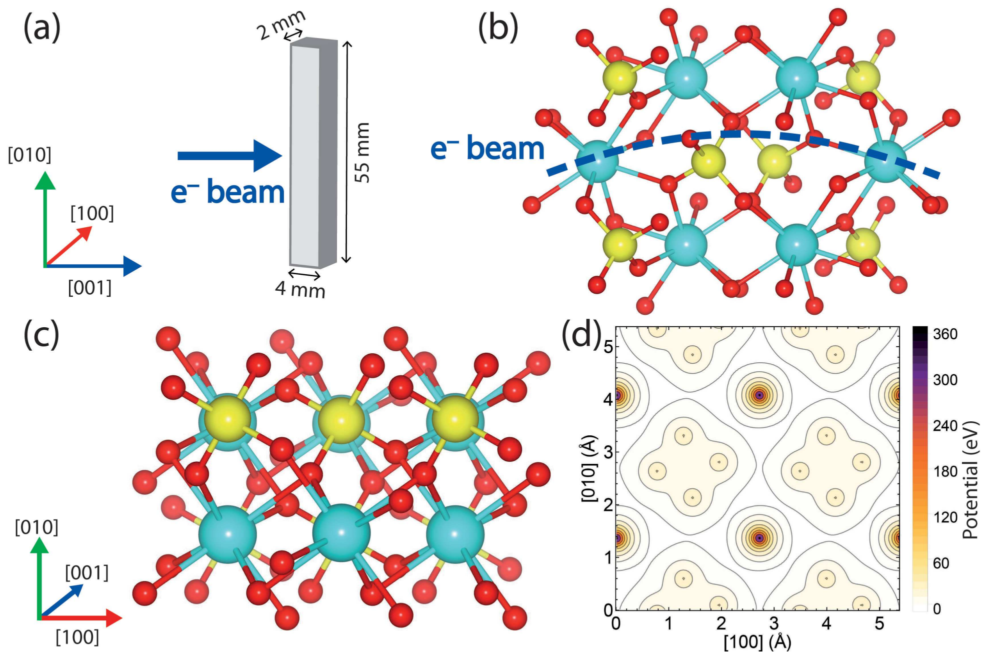

Figure 6.1: PWO crystal and its electric potential. (a) Orientation of the crystal with respect to the electron beam. PWO crystal lattice from the side (b) and along the trajectory (c). (d) Average continuous axial potential felt by electrons moving along the [001] axis. Room-temperature thermal vibrations have been taken into account.[194]

A PWO crystal has a scheelite-type structure characterized by a tetragonal lattice with constants a =b= 5.456 $\mathring{A}$ and c=12.020$\mathring{A}$. Thus, the sample used has main face corresponding to the (100) planes.

The electron and positron beams were aligned with the [001] crystal axis, which was parallel to the $L = 4\,\text{mm} = 0.45X_0$ crystal side, as shown in Fig.6.1(a). Fig.6.1 also displays the PWO crystal lattice from [100] (b) and [001] (c) axis view, while the continuous axial potential felt by the particle moving along the [001] axes is represented in Fig.6.1(d). The high-energy beam of the CERN SPS H4 beamline was used to explore the deep strong field regime, characterized by a factor $\chi \simeq 4$, corresponding to a maximal axial field strength of $E \approx 2.3 \times 10^{11} V/cm$ and a Lorentz factor $\gamma \approx 2.35 \times 10^5$. The crystal thickness was chosen to highlight the transition from the "thin target" limit ($L < X_0$) for the case of random crystal-to-beam alignment, to the opposite condition of "thick target", corresponding to the crystal disposed in axial orientation, in which X_0 is reduced to an effective value, $X_{0_{eff}}$, in such a way that $L > X_{0_{eff}}$.

6.1 X-rays characterization

The axial effect depends on the presence and alignment with a crystalline structure. Almost ideally perfect crystals have been achieved only for a handful of material. Semiconductor industry has reached a standard of almost perfect Silicon and Germanium, and intense research is being focused on new material such as Silicon Carbide and Gallium Arsenide. Diamond can be growth with high level of purity and lattice quality, although in much smaller size than ingots. The other single crystals produced present a structure composed by a multitude of little crystal (crystallites) aligned within an angular range, called mosaicity. Defects in the periodic lattice structure, such as dislocations, are several orders of magnitude more frequent wrt Silicon. In order to obtain a realistic characterization of the effective crystalline structure of the sample, X-ray diffraction studies were performed. The mosaicity of the sample was measured at ID11 beamline of ESRF synchrotron (Grenoble). At the facility it was possible to access to high energy X-rays (140 keV) and high intensity beam. Since PWO strongly absorb x-rays, these features are critical to penetrate across the whole sample thickness and directly investigate the lattice bulk. The beam was collimated to micrometric size ($50\times 50\ \mu\mathrm{m}^2$) for spatial resolution.

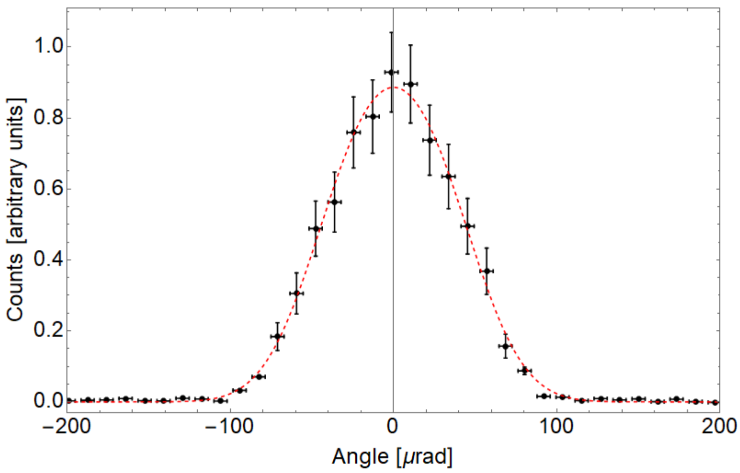

Figure 6.2: One of the RC measured at the central part of the PWO strip. The FWHM of the curve indicates the mosaicity of the crystal

The sample was measured across the 2 mm thickness in order to measure the crystal bulk mosaicity. Several rocking curves of *(200)* were acquired in different locations. The angular resolution of the experimental setup was 3 μrad, thanks to the small angular divergence of the x-rays beam and the high monochromaticity ($\Delta E/E \approx\ 10^{-3}$). The mosaicity observed over the sample was lower than 100 *mu*rad (fig 6.2). Being the mosaicity lower than the angular range of the strong field, the whole sample can be axially aligned.

Further characterizations were carried out at Ferrara Sensor and Semiconductor Laboratory. An estimation of the dislocation density was carried out exploiting the anomalous absorption phenomena (Borrmann effect [195]). Indeed, the high-resolution diffractometer should operates at energy range too low to characterize the internal structure of the sample, being 8.04 KeV photons absorbed in few microns by lead tungstate. However, dynamical theory expects diffracting x-rays to propagate through the lattice as a set of standing waves. The waves nodes can either fall on crystal planes or beside them. The first wave mode absorption is naturally enhanced, but for the latter mode the effective absorption is strongly suppressed. X-rays are thus able to propagate "anomalous" length inside the sample. The phenomenon is only possible if the x-rays are continuously interacting with a perfect crystal lattice within a characteristic length called *extinction distance* Λ, thus maximum allowed dislocation density δ_d is limited to $\approx 1/\Lambda^3$.

Anomalous absorption was observed during diffraction of (200) planes across a 0.5 mm thickness lead tungstate. A diffracted peak was detected in Laue configuration, while transmitted beam was completely blocked when misaligned from diffraction. The sample was purchased from the same producer showed similar mosaicity when measured at ESRF, thus the quality of the crystal was accepted as similar to the 2 mm thick specimen. Direct investigation was not possible as even with anomalous absorption the sample was too thick.

Λ is inversely proportional to X-rays wavelength, hence measures at different energy would provide different constrains to the sample lattice quality. The high energy measurements performed at ESRF with 140 KeV X-rays did not show any anomalous absorption. Thus it is possible to define a minimum and maximum dislocation density as $1/\Lambda^3_{140KeV} < \delta_d < 1/\Lambda^3_{8.04KeV}$, This means that within a volume of $(\Lambda_{8.04})^3$ the lattice appears with no defects, while defects are present in a volume of $(\Lambda_{140})^3$. Thus, the range of dislocation density should be $[(\Lambda_{140})^{-3} : (\Lambda_{8.04})^{-3}] = [10^6/\text{cm}^2 : 8 \times 10^9/\text{cm}^2]$.

6.2 Experiment at CERN

The sample was mounted on high-resolution goniometer to be aligned with the beam. The instrument was the same employed in chapter 5.2. A similar tracking system was used as well, with one less silicon plane (SD) downstream the crystal. Indeed, in the previous experiment focus was the particle deflection, so two SD planes were dedicated to directly track the deflection angle. In this case, deflection angle is extracted by knowing the distance

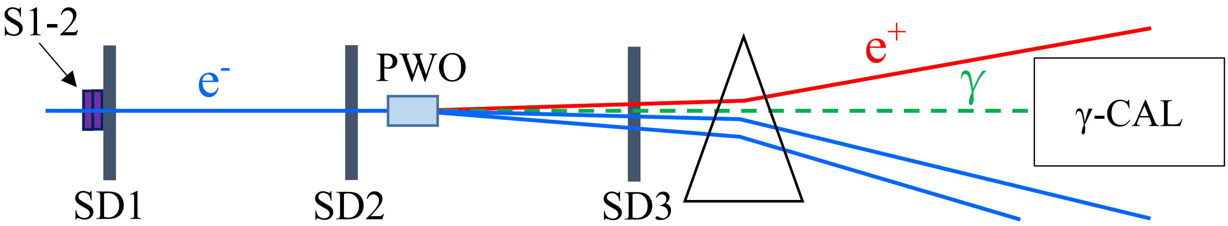

Figure 6.3: Experimental setup. S1-2 are the plastic scintillators used for the trigger; SD1, SD2, and SD3 are the Silicon Detectors forming the tracker. The triangle represents the bending magnet that separates both the primary electrons and secondary charged particles produced by emitted photons inside the PWO sample. γ-CAL is the e.m. calorimeter used to collect the emitted photons.[194]

of the crystal from the only downstream SD and extracting the distance. Being the PWO strip much shorter along the beam than the prototypes for spin precession (1:13.75-20) and the distance from SD3 ($\approx$ 1:1000). Hence its size can be approximated to a point in the reconstruction of trajectories with error of order of 0.1%. This allowed to reduce material on the beam and thus possible radiation background. The tracking system allowed to achieve angular resolution of $\approx$ 10 μrad on the beam trajectory.

The setup described in [196] was upgraded with a new γ-calorimeter based on a 3×3 matrix of CMS-type ECAL crystals, covering a total of $25X_0$ to measure all the produced γ-rays downstream the crystal. Also the γ-CAL, in turn, was made of lead tungstate.

The beam divergence was 80×90 μrad^2 in horizontal and vertical directions, respectively. After the silicon telescope, a bending magnet (the triangle in Fig.6.3) separated the charged beam (composed by the primary particles and pairs generated in the crystal)from the emitted γ-rays, which are collected at the downstream e.m. calorimeter.

Axial alignment requires both horizontal and vertical angular scan. In the first horizontal angular scan, (100) planes were individuated among other skew planes. Then, the crystal was aligned with the [001] axes by scanning the vertical rotational movement. After the measurement in axial alignment, the radiation energy loss spectrum was measured also far from main crystallographic orientations. The configuration was chosen to measure the sample behaviour in condition of almost complete suppression of orientational coherent effect from the lattice structure.

Figure 6.4-a displays the experimental radiated energy distribution of the 120 GeV/c electrons $(1/N)\Delta N(E)/\Delta E$, where $\Delta N(E)$ is the number of events acquired in the range $[E - \Delta E/2, E + \Delta E/2]$, ΔE being the bin size of the distribution and N the total number of entries. The x-axis values represent the sum of the energies of all the photons collected

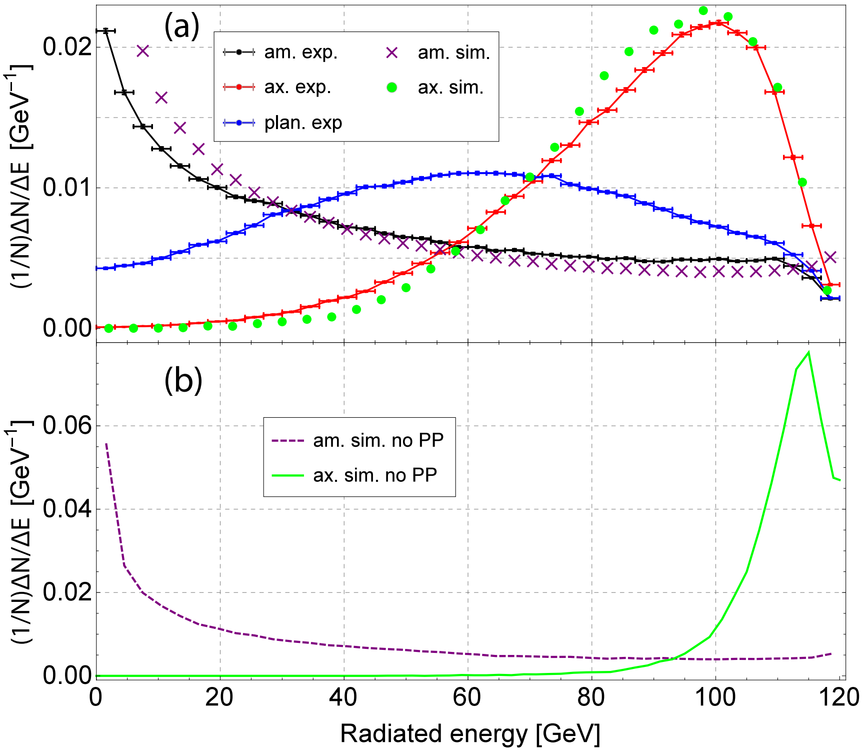

Figure 6.4: a. Distributions of the radiated energy by 120 GeV electrons in the 4 mm-long PWO target, $(1/N)\Delta N(E)/\Delta E$, measured collecting all the survived photons with the γ-CAL placed downstream the crystal, in three different crystal-to-beam configuration: random (am. exp.), axial (ax. exp.), and planar (pl. exp.) alignment. The Monte Carlo simulations regarding the axial and amorphous case (ax. sim. and am. sim.) including in the code both the PP by the emitted γ and γ emission by the produced $e^{\pm}$ are also shown. b. Simulated total radiative energy loss obtained by switching off the PP by the emitted γ for the randomly (am. sim. no PP) and axially (ax. sim. no PP) aligned cases.[194]

at the downstream γ-CAL; in other words, all the produced γs by each primary e^- in the PWO crystal and not absorbed/converted inside it. Indeed, the crystal was thick enough to allow pairs production from emitted photons and, since it is not possible to distinguish the primary from the secondary electrons, all of them were swiped away by the magnetic field upstream the γ-CAL (see Fig. 6.3). Details of the measurement procedure can be found in Ref. [197, 198]. As expected, the distributions for both the axial and planar cases are harder if compared with the random case and peaked at 60 and 100 GeV, respectively. On the other hand, the radiated energy distribution related to the amorphous case has the typical shape of nearly single-photon Bethe-Heitler spectrum, with a sharp $1/E$-like decrease in the soft photon region, on the left.

The enhancement of γ quanta emission resulted in a decrease of the effective radiation length in the axially oriented PWO crystal, with an acceleration of the e.m. shower development.

Further proof of this is the relevant growth of production of secondary charged particles, as measured with the SD3 silicon detector placed downstream the crystal just before the bending magnet. During the analysis, we selected only single hits registered by both SD1 and SD2 detectors, i.e., only incoming single tracks onto the crystal. It resulted that the number of produced particles detected by the Si detector SD3 was enlarged by a factor of three when the sample was axially aligned, with only 30% left of single tracks if compared with the 70% in case of random orientation. This was indeed a first qualitative demonstration of the transition from nearly pure bremsstrahlung to pronounced shower development, with an increase of generation of secondary particles, caused by the strong decrease of $X_{0_{eff}}$.

Since part of the radiated energy by the primary electrons was converted in pairs and not collected at the calorimeter, a proper estimation of the $X_{0_{eff}}$ reduction factor can be done only through Monte Carlo simulation. We recently developed a method of direct integration of the Baier Katkov (BK) formula [196, 199] and tested it vs. experimental results with Si crystals [196, 198, 200]. The BK quasi-classical method is used to compute the e.m. radiation emission by ultrarelativistic particles in an external field taking into account quantum recoil and is commonly used to treat the strong field effects in crystals [201]. For the case of this letter, we included the contribution of PP through the BK method to describe the shower development. The results of the simulation for the radiated energy distributions for 120 GeV e^- under axial (ax. sim.) and random (am. sim.) alignment are shown in Fig.6.4-a, being in quite good agreement with the experimental results. Indeed, with the aim of reproducing the experimental configuration, the simulation plots include only the total energy of the photons survived after the crystal.

The agreement between the experiment and simulations proved the feasibility of the method that can be used to infer the total radiative energy loss by the primary electron. This was done modifying the code by switching off the PP by the emitted γ-rays. The simulation result is shown in Fig.6.4-b. Here, in case of axis-to-beam alignment the distribution shows a peak around 115 GeV, with an average energy loss E_{loss} = 109.7 GeV per e^-. This latter value is consistent with $X_{0_{eff}} \simeq 1.6\ mm$, determined by the equation $E_{loss} = E_{beam}(1 - e^{-L/X_{0_{eff}}})$ with E_{beam} = 120 GeV, which results in a ratio $X_0/X_{0_{eff}} \simeq 5$. Such estimation is an approximation since the primary beam energy, and consequently the χ parameter, decrease during the shower development, with a consequent increase of $X_{0_{eff}}$ [202]. Nevertheless, through simulation it is possible to extrapolate the correct value at different particle energy, being indeed $X_{0_{eff}} \simeq 1.35\ mm$ for the primary 120 GeV e^-.

The same investigation was repeated using a positron beam in order to observe the effect for positive particles being the the two beam otherwise similar in all other features such as size, angular divergence and energy. Indeed, both electrons and positrons are produced by gamma photon conversion in the same target: switching current sign of upstream e.m. optics allows to deliver to the experimental area either type of particles.

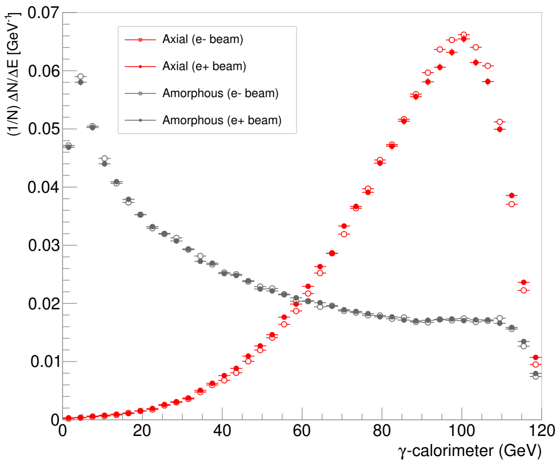

Figure 6.5: Energy distribution of the γ-photons emitted by the interaction of 120 GeV e- and e+ beams with a PWO crystal of 4 mm. The radiated energy detected by the γ-calorimeter in axial (in *red*) and amorphous (in *grey*) beam-to-crystal alignments. Filled circles correspond to the energy distribution emitted by e+ particles-to-crystal interactions; not filled circles correspond to the energy distribution emitted by e- particles-to-crystal interactions. Events producing photons with energy lower than 1 GeV were discarded.

As expected, the distribution of photons created by primary e+ is in agreement with the distribution generated by primary e-, for both beam-to-crystal alignments. In either cases the distributions were peaked at ≈ 100 GeV.

Indeed, photon emission mechanism is the same for both kind of particles. Although in case of non-divergent beam and ideally perfect crystal differences were expected, as channeling effect would affect differently positrons and electrons trajectory inside the medium. In the experiment the beam divergence and lattice defects presence were verified, thus channeling was strongly suppressed and no clear effect was observed in the experimental data.

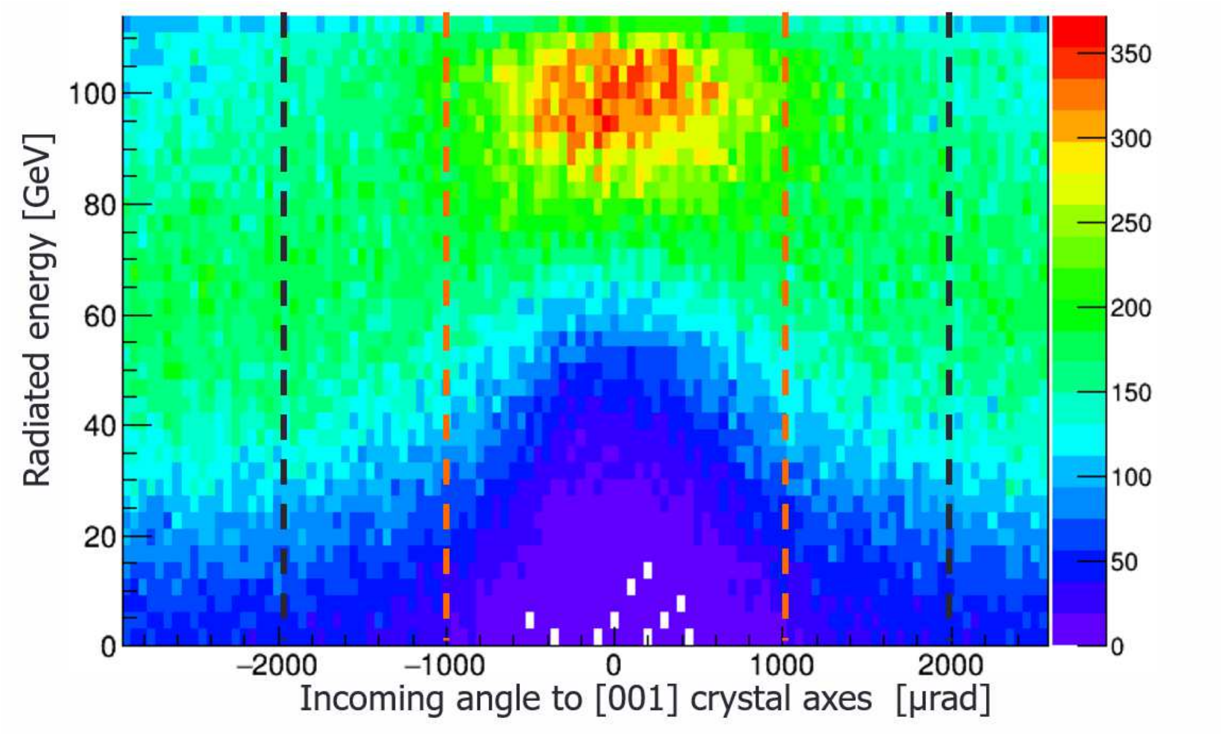

Figure 6.6: Experimental radiated energy distribution by 120 GeV/c e^- inside the crystal vs. [001] axes-to-beam orientation, as measured by the downstream calorimeter collected by rotating the crystal with the goniometer along the (100) planes. The region within ± 1 $mrad$ is between two red-dashed vertical lines, while the region within $\psi = \pm 2$ $mrad$ mrad is between two black-dashed vertical lines.[194]

For applications in both HEP and astrophysics, the angular acceptance of e.m. shower enhancement is a key parameter. Fig.6.6 shows the experimental radiated energy distribution vs. [001] axes-to-beam orientation, collected by rotating the crystal along the (100) planes with the goniometer. The relevant increase in the energy loss due to the interaction with the crystal axes is maintained for about $\pm$ 1 $mrad$ (vertical red-dashed lines), which corresponds to the theoretical angular region for strong synchrotron-like radiation and PP, i.e $\psi \simeq \pm V_0/m = \pm 1$ $mrad$. As expected, such angular acceptance is one order of magnitude larger than the critical angle for channeling $\theta_c \approx 100$ μrad. At larger incidence angle, the distribution approaches to the planar level peaked at 60 GeV when $\psi \simeq$ 2-3 $mrad > V_0/m$. From theory and previous experiments with W crystals [203], at still larger incidence angle with respect to either axial or planar directions, CB/CPP regime holds true [204] and a measurable contribution to radiation/PP increase should manifest up to $\psi \sim 17 \times 10^3$(about one degree).

6.3 Possible Applications

The measured X_0 reduction manifests in an acceleration of the e.m. shower development, the strength of which depends on the particle energy and its direction with respect to the main crystal axes, being maximal at the beginning of the shower when the primary particle possesses the highest energy [202]. The existing e.m. calorimeters made of high-Z scintillators, such as ECAL for CMS and Fermi LAT, have a crystalline structure [182, 183]. Thus, in principle, orientational effects could have been registered also for these experiments, even if the crystalline structure of the scintillators was not considered when they were mounted. However, this possibility is very unlikely because the majority of the events occurs at $\psi \gg V_0/m$, thereby making the influence of the crystal structure quite marginal. Nevertheless, the unavoidable existence of rare events with $e^{\pm}$ and γ incidence at $\psi \leq V_0/m$ with one of the main crystal axes would demand further investigation.

On the other hand, the acceleration of e.m. shower development in oriented scintillator crystals can be exploited for future fixed-target experiments to build compact forward e.m. calorimeters/pre-showers, with a considerable reduction of the detector thickness for beam incidence in the range $\psi \sim mrad$. Furthermore, these effects can be applied to diminish the thickness of a photon converter, taking advantage of the reduced ratio between X_0 and nuclear interaction length, thus increasing the transparency to hadrons as done in the past by the NA48 experiment at CERN [76], as well as in the construction of a downstream calorimeter to detect photons in the existing beam without being blinded by hadronic interactions [205]. A similar principle can be transferred to light dark matter search to decrease the dump length, which is a crucial parameter [206]. Indeed, if a dark photon is created during the e.m. shower initiated by a primary $e^{\pm}$, it can be detected only if survives after the remaining dump length. The shorter is such length, the higher is the sensitivity to dark photons.

Furthermore, with the birth of multimessenger astrophysics, one may think of pointing a telescope towards a source, thus measuring the spectrum of a point-like γ-source in the TeV energy region [58, 207]. If a satellite is equipped with a calorimeter module made of oriented crystals, the shower of γ-rays with energy larger than 100 GeV can be completely contained in a quite compact volume, reducing the necessary weight—and therefore the cost—compared to those currently used. In the absence of pointing, a calorimeter made of oriented scintillators would continue to operate in a standard way. Thinking of an apparatus similar to FERMI LAT [183], the reduction of X_0 in oriented crystals could be useful to reduce both the calorimeter volume and the thickness of the photo-converters in the tracking system, thus reducing the dispersive effect of the multiple scattering that worsens the detector resolution. The advantage of using high-Z scintillators instead of metallic crystals, such as W or Ir as NA48 did, is the better crystallographic quality and the possibility to be grown in virtually any size [193]. Indeed, the mosaic spread of the PWO sample used in the experiment is ≈ 0.1 *mrad* as measured with X-ray diffraction, while it is usually more than 1 mrad for commercially available metallic crystals. Moreover, the transparency of the crystals gives the additional possibility to measure directly the characteristics of the cascade by collecting the scintillation light, as in the CERN NA64 experiment *active beam dump* [208].

Chapter 7

Conclusions

A new design for silicon bent collimator of LHC was proposed, in order to substitute the older version with a thermal stable one. The work focused on both optimization of the crystalline material and holder structure. The silicon wafer crystal miscut was characterized and successfully reduced by up to two order of magnitude in order to achieve standard for LHC operation. To our knowledge, a record of parallelism between optical surface and lattice planes was reached during this work. A careful selection of the best crystallographic orientation was selected for the strip samples, in order to suppress torsion induced by crystal anisotropy. A deep and careful control lattice quality was carried out on the machined surfaces of the sample, employing several techniques (x-rays diffraction, micro-Raman, RBS and TEM) up to the most superficial atomic plane. An etching procedure for the titanium holders was devised in order to reduce surface stresses and impurities from the production process. A specific assembly routine was devised for the sample: using precise dynamometric torques in clean room ISO-4 environment to maximize reproducibility. A total of 27 samples were tested, and 10 samples were selected for testing at CERN facilities. The thermal stability after LHC bake-out process and bending condition characterized in Ferrara were officially confirmed. The current competence acquired allows to fabricate crystal collimator suitable for an actual installation in LHC.

The challenge of increasing deflection angle and sizes of crystal for extraction and spin precession studies was undertaken, significantly changing the sample shapes and bending methods. Investigation of the maximum length of anticlastic curvature, previously used for strip shaped samples, was carried out and record size and deflection were achieved while maintaining fairly homogeneous curvature. A completely novel approach was tested when self-standing sandblasting method was employed. In order to adapt the technique to halo extraction, a patterning of the machining was designed. The obtained curvature was tested at ESRF with hard x-ray micro-beam, a constant curvature was confirmed. A deep characterization with x-rays tomography at KIT synchrotron confirmed the conservation of perfect lattice quality after the bending process. The sample showed efficient channeling when tested at H8 extracted beam line of SPS, CERN. After the final control of thermal stability, the technologies proved to be suitable for application in LHC beampipe for halo steering. Prototype crystals for spin precession of strange and charmed baryons where devised within the SELDOM project collaboration. This new set of samples required a further increase of both size and curvature. In particular, radius of curvature was significantly decreased from $\approx 10^2$ m to 5 m. A novel holder type was developed to directly impose the curvature used for beam steering, discarding the secondary curvature approach exploited previously in Ferrara research group. Furthermore, manipulation of Germanium crystal was investigated as well to increase steering power and efficiency. Two samples made of Silicon and Germanium were produced and successfully tested with 180 pion beams at CERN. This result achieved a milestone of the project, currently in progress until 31st of March 2023.

Finally, a different orientational coherent phenomena was investigated with heavy inorganic scintillator. By exploiting the strong fields arising from axial continuous potential of lead tungstate (PWO), effects of nonlinear QED were observed during interaction of the crystal axis with 120 GeV $e^{\pm}$ at CERN. The defects of the crystal structure of the samples were previously estimated at ESRF synchrotron and at Ferrara laboratories. The results of the measurements contributed to the creation of dedicated experiments ELIOT (Electromagnetic Processes in Oriented Crystals) and OSCaR (*Oriented Scintillator Crystals*) at the INFN section of Ferrara.

Bibliography

[1] J. Lindhard. Influence of crystal lattice on motion of energetic charged particles. *Danske Vid. Selsk. Mat. Fys. Medd.*, 34:14, 1965.

[2] A.F. Elishev et al. Steering of charged particle trajectories by a bent crystal. *Phys Lett B*, 88(34):387 – 391, 1979. doi: 10.1016/0370-2693(79)90492-1.

[3] VG Baryshevsky. Spin rotation of ultrarelativistic particles passing through a crystal. *Sov. Tech. Phys. Lett*, 5:73, 1979.

[4] J. Stark. *Phys. Zs.*, 13:973, 1912.

[5] B. Ferretti. Sulla bremsstrahlung nei cristalli. *Nuovo Cim.*, 7:118, 1950.

[6] M. L. Ter-Mikaelian. *High-energy Electromagnetic Processes in Condensed Media*. Wiley, New York, 1972.

[7] H. Uberall. High-energy interference effect of bremsstrahlung and pair production. *Phys. Rev.*, 103:1055, 1956.

[8] H. Bethe and W. Heitler. On the stopping of fast particles and on the creation of passive electrons. *Proc. Roy. Soc.*, 146:83–112, 1934. doi: 10.1098/rspa.1934.0140.

[9] GIORDANO DIAMBRINI Palazzi. High-energy bremsstrahlung and electron pair production in thin crystals. *Rev. Mod. Phys.*, 40:611–631, 1968.

[10] Mark T. Robinson and O. S. Oen. The channeling of energetic atoms in crystal lattices. *Applied Physics Letters*, 2:30–32, 1963.

[11] G. R. Piercy, F. Brown, J. A. Davies, and M. McCargo. Experimental evidence for the increase of heavy ion ranges by channeling in crystalline structure. *Phys. Rev. Lett.*, 10:399–400, 1963. doi: 10.1103/PhysRevLett.10.399.

[12] E. N. Tsyganov. Some aspects of the mechanism of a charge particle penetration through a monocrystal. Technical report, Fermilab, 1976. Preprint TM-682.

[13] V. V. Avdeichikov, V. N. Buldakovskii, A. V. Bychkov, A. S. Vodop'yanov, I. Voitkovska, v. M. Golovatyuk, v. P. Grigor'yev, z. Guzik, v. P. Zabolotyn, N. I.

Zimin, I. B. Issinskii, R. B. Kadyrov, B. K. Kuryatnikov, L. G. Makarov, E. A. Matyushevskii, V. A. Monchinskii, T. s. Nigmanov, S. A. Novikov, V. G. Perfeev, V. D. Ryabtsov, A. B. Sadovskii, v. G. Timofeev, I. A. Tyapkin, N. A. Filatova, E. N. Tsyganov, M. D. Shafranov, D. I. Sherstyanov, , and D. Yavorska. Accelerated beam extraction by means of a bent single crystal at the JINR synchrophasotron. 1986.

[14] A.A. Asseev, M.D. Bavizhev, E.A. Ludmirsky, V.A. Maisheev, and Yu.S. Fedotov. Extraction of the 70 GeV proton beam from the IHEP accelerator towards beam line 2(14) with a bent single crystal. *Nucl. Instr. Meth. Phys. Res. A*, 309(1):1 – 4, 1991. ISSN 0168-9002. doi: 10.1016/0168-9002(91)90084-4.

[15] A.A. Asseev, E.A. Myae, S.V. Sokolov, and Yu.S. Fedotov. On increasing the bent crystal extraction efficiency by using a thin internal target. *Nucl. Instr. Meth. Phys. Res. A*, 324(1):31 – 33, 1993. ISSN 0168-9002. doi: 10.1016/0168-9002(93)90963-I.

[16] V.M. Biryukov, Yu. A. Chesnokov, and V. I. Kotov. *Crystal Channeling and Its Application at High-Energy Accelerators*. Springer, Berlin, 1997.

[17] H. Akbari et al. First results on proton extraction from the cern-sps with a bent crystal. *Physics Letters B*, 313:491 – 497, 1993.

[18] K. Elsener et al. Proton extraction from the cern sps using bent silicon crystals. *Nucl. Instrum. Methods Phys. Res., Sect. B*, 119:215 – 230, 1996. ISSN 0168-583X. doi: 10.1016/0168-583X(96)00239-X.

[19] G. Arduini, K. Elsener, G. Fidecaro, M. Gyr, W. Herr, J. Klem, U. Mikkelsen, and E. Weisse. Energy dependence of crystal assisted extraction at the CERN SPS. volume 1, pages 168–170, 1998. doi: 10.1109/PAC.1997.749580.

[20] R.A. Carrigan, Chen Dong, P. Colestock, D. Herrup, G. Goderre, G. Jackson, C.T. Murphy, R. Stefanski, S. Baker, N. Mokhov, B. Parker, H.-J. Shih, R Soundranayagam, T. Toohig, S. Peggs, C.R. Sun, A. Boden, D. Cline, W. Gabella, S. Ramachandran, J. Rhoades, J. Rosenzweig, M. Arenton, S. Conetti, B. Cox, C. Dukes, V. Golovatyuk, A. McManus, K. Nelson, B. Norem, B. Newberger, J.A. Ellison, A. Erwin, R. Rossmanith, A. Kovalenko, A. Taratin, N. Malakhov, E. Tsyganov, M. Bavizhev, V. Biryukov, M. Maslov, A. Khanzadeev, T. Prokofieva, V. Samsonov, and G. Solodov. Extraction from TeV-range accelerators using bent crystal channeling. *Nucl. Instr. Meth. Phys. Res. B*, 90(1):128 – 132, 1994. ISSN 0168-583X. doi: 10.1016/0168-583X(94)95527-1.

[21] R. A. Carrigan *et al.* Beam extraction studies at 900 gev using a channeling crystal. *Phys. Rev. ST Accel. Beams*, 5:043501, 2002. doi: 10.1103/PhysRevSTAB.5.043501.

[22] V. Biryukov. Simulation of beam steering phenomena in bent crystals. *Nucl. Instr. Meth. Phys. Res. B*, 153(1-4):461–466, 1999. doi: 10.1016/S0168-583X(99)00064-6.

[23] A.M. Taratin. Computer simulation of accelerator beam extraction with a bent crystal. *Nucl. Instr. Meth. Phys. Res. B*, 95(2):243–248, 1995. doi: 10.1016/0168-583X(94)00465-X.

[24] A.M. Taratin, S.A. Vorobiev, M.D. Bavizhev, and I.A. Yazynin. Computer simulation of multitum beam extraction from accelerators by bent crystals. *Nucl. Instr. Meth. Phys. Res. B*, 58(1):103–108, 1991. doi: 10.1016/0168-583X(91)95683-5.

[25] V. Biryukov. Optimization of crystal extraction experiment. *Nucl. Instr. Meth. Phys. Res. B*, 117(4):463 – 466, 1996. ISSN 0168-583X. doi: 10.1016/0168-583X(96)00214-5.

[26] Oliver S. Bruning, P. Collier, P. Lebrun, S. Myers, R. Ostojic, J. Poole, and P. Proudlock. Lhc design report vol.1: The lhc main ring. Technical Report CERN-2004-003-V-1, 2004.

[27] W. Scandale, A.D. Kovalenko, and A.M. Taratin. Possibility of high efficient beam extraction from the CERN SPS with a bent crystal. simulation results. *Nucl. Instr. Meth. Phys. Res. A*, 848:166–169, 2017. doi: 10.1016/j.nima.2016.12.023.

[28] S. Baricordi, V. Guidi, A. Mazzolari, G. Martinelli, A. Carnera, D. De Salvador, A. Sambo, G. Della Mea, R. Milan, A. Vomiero, and W. Scandale. Optimal crystal surface for efficient channeling in the new generation of hadron machines. *Appl. Phys. Lett.*, 91(6):061908, 2007. doi: 10.1063/1.2768200.

[29] A. G. Afonin *et al.* High-efficiency beam extraction and collimation using channeling in very short bent crystals. *Phys. Rev. Lett.*, 87:094802, Aug 2001. doi: 10.1103/PhysRevLett.87.094802.

[30] V. Guidi, L. Lanzoni, and A. Mazzolari. Study of anticlastic deformation in a silicon crystal for channeling experiments. *Journal of Applied Physics*, 107(11):113534–1–113534–7, 2010. doi: 10.1063/1.3372722.

[31] *SEMI M59: terminology for silicon technology.* Semiconductor Equipment & Materials Institute.

[32] W. et al. Scandale. Apparatus to study crystal channeling and volume reflection phenomena at the SPS H8 beamline. *Rev. Sci. Instr.*, 79(2):023303, 2008. doi: 10.1063/1.2832638.

[33] A. Mazzolari, E. Bagli, L. Bandiera, V. Guidi, H. Backe, W. Lauth, V. Tikhomirov, A. Berra, D. Lietti, M. Prest, E. Vallazza, and D. De Salvador. Steering of a Sub-GeV electron beam through planar channeling enhanced by rechanneling. *Phys. Rev. Lett.*, 112:135503, 2014. doi: 10.1103/PhysRevLett.112.135503.

[34] W. et al. Scandale. Observation of channeling and volume reflection in bent crystals for high-energy negative particles. *Phys. Lett. B*, 681(3):233 – 236, 2009. ISSN 0370-2693. doi: 10.1016/j.physletb.2009.10.024.

[35] W. et al. Scandale. High-efficiency deflection of high energy protons due to channeling along the (110) axis of a bent silicon crystal. *Phys. Lett. B*, 760:826–831, 2016. doi: 10.1016/j.physletb.2016.07.072.

[36] W. Scandale *et al.* High-efficiency deflection of high-energy negative particles through axial channeling in a bent crystal. *Phys. Lett. B*, 680(4):301 – 304, 2009. doi: 10.1016/j.physletb.2009.09.009.

[37] L. Bandiera, A. Mazzolari, E. Bagli, G. Germogli, V. Guidi, A. Sytov, I.V. Kirillin, N.F. Shul'ga, A. Berra, D. Lietti, M. Prest, D. De Salvador, and E. Vallazza. Relaxation of axially confined 400 GeV/c protons to planar channeling in a bent crystal. *Eur. Phys. J. C*, 76(2):1–6, 2016. doi: 10.1140/epjc/s10052-016-3899-x.

[38] W. Scandale, A. Vomiero, E. Bagli, S. Baricordi, P. Dalpiaz, M. Fiorini, V. Guidi, A. Mazzolari, D. Vincenzi, R. Milan, G. Della Mea, E. Vallazza, A.G. Afonin, Y.A. Chesnokov, V.A. Maisheev, I.A. Yazynin, A.D. Kovalenko, A.M. Taratin, A.S. Denisov, Y.A. Gavrikov, Y.M. Ivanov, L.P. Lapina, L.G. Malyarenko, V.V. Skorobogatov, V.M. Suvorov, S.A. Vavilov, D. Bolognini, S. Hasan, A. Mattera, M. Prest, and V.V. Tikhomirov. Observation of multiple volume reflection by different planes in one bent silicon crystal for high-energy negative particles. *EPL*, 93(5), 2011. doi: 10.1209/0295-5075/93/56002.

[39] Victor Tikhomirov. Multiple volume reflection from different planes inside one bent crystal. *Physics Letters B*, 655:217 – 222, 2007. doi: 10.1016/j.physletb.2007.09.049.

[40] W. Scandale et al. First observation of multiple volume reflection by different planes in one bent silicon crystal for high-energy protons. *Physics Letters B*, 682(3):274 – 277, 2009. doi: 10.1016/j.physletb.2009.11.026.

[41] W. Scandale *et al.* Multiple volume reflections of high-energy protons in a sequence of bent silicon crystals assisted by volume capture. *Phys. Lett. B*, 688:284 – 288, 2010. doi: 10.1016/j.physletb.2010.04.044.

[42] W. Scandale et al. Mirroring of 400 GeV/c protons by an ultra-thin straight crystal. *Phys. Lett. B*, 734(Supplement C):1 – 6, 2014. ISSN 0370-2693. doi: 10.1016/j.physletb.2014.04.062.

[43] W. et al. Scandale. Observation of nuclear dechanneling length reduction for high energy protons in a short bent crystal. *Phys. Lett. B*, 743:440–443, 2015. doi: 10.1016/j.physletb.2015.02.072.

[44] W. Scandale *et al.* Observation of nuclear dechanneling for high-energy protons in crystals. *Phys. Lett. B*, 680(2):129 – 132, 2009. doi: 10.1016/j.physletb.2009.08.046.

[45] Enrico Bagli et al. Steering efficiency of a ultrarelativistic proton beam in a thin bent crystal. *Eur. Phys. J. C*, 74(1):2740, 2014. doi: 10.1140/epjc/s10052-014-2740-7.

[46] E. Bagli, V. Guidi, A. Mazzolari, L. Bandiera, G. Germogli, A.I. Sytov, D. De Salvador, A. Berra, M. Prest, and E. Vallazza. Experimental evidence of independence of nuclear de-channeling length on the particle charge sign. *Eur. Phys. J. C*, 77(2), 2017. doi: 10.1140/epjc/s10052-017-4642-y.

[47] W. Scandale*et al.* Measurement of the dechanneling length for high-energy negative pions. *Physics Letters B*, 719:70 – 73, 2013. doi: 10.1016/j.physletb.2012.12.061.

[48] W. Scandale, G. Arduini, R. Assmann, C. Bracco, S. Gilardoni, V. Ippolito, E. Laface, R. Losito, A. Masi, E. Metral, V. Previtali, S. Redaelli, M. Silari, L. Tlustos, E. Bagli, S. Baricordi, P. Dalpiaz, V. Guidi, A. Mazzolari, D. Vincenzi, Gianantonio Della Mea, A. Lombardi, D. De Salvador, E. Vallazza, D. Bolognini, S. Hasan, D. Lietti, V. Mascagna, A. Mattera, M. Prest, G. Cavoto, L. Ludovici, D. Mirarchi, R. Santacesaria, P. Valente, F. Murtas, A.G. Afonin, Yu.A. Chesnokov, V.A. Maisheev, I.A. Yazynin, A.D. Kovalenko, A.M. Taratin, A.S. Denisov, Yu.A. Gavrikov, Yu.M. Ivanov, L.P. Lapina, L.G. Malyarenko, V.V. Skorobogatov, V.M. Suvorov, S.A. Vavilov, N. Mokhov, D. Still, G. Robert-Demolaize, T. Markiewicz, and M. Oriunno. First results on the SPS beam collimation with bent crystals. *Phys. Lett. B*, 692(2):78 – 82, 2010. ISSN 0370-2693. doi: 10.1016/j.physletb.2010.07.023.

[49] W. Scandale, G. Arduini, M. Butcher, F. Cerutti, S. Gilardoni, L. Lari, A. Lechner, R. Losito, A. Masi, A. Mereghetti, E. Metral, D. Mirarchi, S. Montesano, S. Redaelli, P. Schoofs, G. Smirnov, E. Bagli, L. Bandiera, S. Baricordi, P. Dalpiaz, V. Guidi, A. Mazzolari, D. Vincenzi, G. Claps, S. Dabagov, D. Hampai, F. Murtas, G. Cavoto, M. Garattini, F. Iacoangeli, L. Ludovici, R. Santacesaria, P. Valente, F. Galluccio, A.G. Afonin, M.K. Bulgakov, Yu.A. Chesnokov, V.A. Maisheev, I.A. Yazynin, A.D. Kovalenko, A.M. Taratin, V.V. Uzhinskiy, Yu.A. Gavrikov, Yu.M. Ivanov, L.P. Lapina, W. Ferguson, J. Fulcher, G. Hall, M. Pesaresi, M. Raymond, and V. Previtali. Optimization of the crystal assisted collimation of the SPS beam. *Phys. Lett. B*, 726 (1-3):182–186, 2013. ISSN 0370-2693. doi: 10.1016/j.physletb.2013.08.028.

[50] G. Germogli, A. Mazzolari, V. Guidi, and M. Romagnoni. Bent silicon strip crystals for high-energy charged particle beam collimation. *Nucl. Instr. Meth. Phys. Res. B*, 402(Supplement C):308 – 312, 2017. doi: 10.1016/j.nimb.2017.03.053.

[51] W. Scandale, G. Arduini, M. Butcher, F. Cerutti, M. Garattini, S. Gilardoni, A. Lechner, R. Losito, A. Masi, D. Mirarchi, S. Montesano, S. Redaelli, R. Rossi, P. Schoofs, G. Smirnov, G. Valentino, D. Breton, L. Burmistrov, V. Chaumat, S. Dubos, J. Maalmi, V. Puill, A. Stocchi, E. Bagli, L. Bandiera, G. Germogli, V. Guidi,

A. Mazzolari, S. Dabagov, F. Murtas, F. Addesa, G. Cavoto, F. Iacoangeli, L. Ludovici, R. Santacesaria, P. Valente, F. Galluccio, A.G. Afonin, Yu.A. Chesnokov, A.A. Durum, V.A. Maisheev, Yu.E. Sandomirskiy, A.A. Yanovich, A.D. Kovalenko, A.M. Taratin, A.S. Denisov, Yu.A. Gavrikov, Yu.M. Ivanov, L.P. Lapina, L.G. Malyarenko, V.V. Skorobogatov, T. James, G. Hall, M. Pesaresi, and M. Raymond. Observation of channeling for 6500 gev/c protons in the crystal assisted collimation setup for lhc. *Phys. Lett. B*, 758:129 – 133, 2016. ISSN 0370-2693. doi: j.physletb.2016.05.004.

[52] Kiko et al. Feasibility studies for single transverse-spin asymmetry measurements at a fixed-target experiment using the lhc proton and lead beams (after@lhc). *Few-Body Systems*, 58(4):139, May 2017. doi: 10.1007/s00601-017-1299-x.

[53] E. Bagli, L. Bandiera, G. Cavoto, V. Guidi, L. Henry, D. Marangotto, F. Martinez Vidal, A. Mazzolari, A. Merli, N. Neri, and J. Ruiz Vidal. Electromagnetic dipole moments of charged baryons with bent crystals at the lhc. *The European Physical Journal C*, 77(12):828, Dec 2017. doi: 10.1140/epjc/s10052-017-5400-x. URL https://doi.org/10.1140/epjc/s10052-017-5400-x.

[54] D Chen, IF Albuquerque, VV Baublis, NF Bondar, RA Carrigan Jr, PS Cooper, Dai Lisheng, AS Denisov, AV Dobrovolsky, T Dubbs, et al. First observation of magnetic moment precession of channeled particles in bent crystals. *Physical review letters*, 69 (23):3286, 1992.

[55] S. Hasan. Bent silicon crystals for the lhc collimation: studies with an ultrarelativistic proton beam. Master's thesis, University of Insubria, 2007.

[56] PA t Doyle and PS Turner. Relativistic hartree–fock x-ray and electron scattering factors. *Acta Crystallographica Section A: Crystal Physics, Diffraction, Theoretical and General Crystallography*, 24(3):390–397, 1968.

[57] G. Moliére. *Z. Naturforsch. A*, 2:133, 1947.

[58] V.N. Baier, V.M. Katkov, and V.M. Strakhovenko. *Electromagnetic Processes at High Energies in Oriented Single Crystals*. World Scientific, Singapore, 1998.

[59] S. Hasan. *Experimental Tecniques for deflection and radiation studies with bent crystals*. PhD thesis, University of Insubria, 2011.

[60] William R Leo. *Techniques for nuclear and particle physics experiments: a how-to approach*. Springer, 1994.

[61] J. Beringer *et al.* Review of particle physics. *Phys. Rev. D*, 86:010001, 2012.

[62] William T. Scott. The theory of small-angle multiple scattering of fast charged particles. *Rev. Mod. Phys.*, 35:231–313, Apr 1963.

[63] V. V. Beloshitsky, M. A. Kumakhov, and V. A. Muralev. Multiple scattering of channeled ions in crystals. *Radiation Effects*, 13(1-2):9–22, 1972.

[64] R.A. Jr Carrigan and J. Ellison. *Relativistic Channeling.* Plenum Press, 1987.

[65] H. Backe, P. Kunz, W. Lauth, and A. Rueda. Planar channeling experiments with electrons at the 855 mev mainz microtron {MAMI}. *Nuclear Instruments and Methods in Physics Research Section B: Beam Interactions with Materials and Atoms*, 266:3835 – 3851, 2008.

[66] Mark T. Robinson and Ordean S. Oen. Computer studies of the slowing down of energetic atoms in crystals. *Phys. Rev.*, 132:2385–2398, Dec 1963.

[67] Esbensen H. and Golovchenko J.A. *Nucl. Phys. A*, 298:382, 1978.

[68] H Esbensen, O Fich, JA Golovchenko, S Madsen, H Nielsen, HE Schiøtt, E èrhøj, C Vraast-Thomsen, G Charpak, S Majewski, et al. Random and channeled energy loss in thin germanium and silicon crystals for positive and negative 2-15-gev/c pions, kaons, and protons. *Physical Review B*, 18(3):1039, 1978.

[69] K.A. Olive et al. Review of Particle Physics. *Chin.Phys.*, C38:090001, 2014.

[70] M.A. Kumakhov. On the theory of electromagnetic radiation of charged particles in a crystal. *Physics Letters A*, 57(1):17 – 18, 1976. doi: 10.1016/0375-9601(76)90438-2.

[71] A. Baurichter *et al.* Channeling of high-energy particles in bent crystals - e2 experiments at the cern sps. *Nuclear Instruments and Methods in Physics Research Section B: Beam Interactions with Materials and Atoms*, 164-165(0):27 – 43, 2000. ISSN 0168-583X. doi: 10.1016/S0168-583X(99)01062-9.

[72] G.H. Wang, P.J. Cong, W.M. Gibson, C.R. Sun, I.J. Kim, S. Salman, M. Pisharody, S.I. Baker, R.A. Carrigan, J.S. Forster, and I.V. Mitchell. Ion channeling study of radiation induced defects in a bent silicon crystal. *Nuclear Instruments and Methods in Physics Research*, 218(1):669 – 672, 1983. ISSN 0167-5087. doi: https://doi.org/10.1016/0167-5087(83)91062-1.

[73] S. I. Baker. Radiation damage effects in channeling applications. pages 391–397, 1987. doi: 10.1007/978-1-4757-6394-$2_2$8.

[74] Yu.A. Chesnokov et al. *Int. J. Mod. Phys. A.*, 2:1733, 1993.

[75] S.I Baker, R.A Carrigan, V.R Cupps, J.S Forster, W.M Gibson, and C.R Sun. Effects on channeling of radiation damage due to 28 gev protons. *Nuclear Instruments and Methods in Physics Research Section B: Beam Interactions with Materials and Atoms*, 90(1):119 – 123, 1994. ISSN 0168-583X. doi: https://doi.org/10.1016/0168-583X(94)95525-5. URL `http://www.sciencedirect.com/science/article/pii/0168583X94955255`.

[76] C Biino, C Clément, Niels T Doble, K Elsener, L Gatignon, P Grafström, U Mikkelsen, K Kirsebom, S P Møller, Erik Uggerhøj, and T Worm. The influence of radiation damage on the deflection of high-energy beams in bent silicon crystals. (CERN-SL-96-030-EA):3 p, Jul 1996. URL `http://cds.cern.ch/record/308375`.

[77] A.M. Taratin and S.A. Vorobiev. Volume reflection of high-energy charged particles in quasi-channeling states in bent crystals. *Phys. Lett. A*, 119:425 – 428, 1987.

[78] et al. W. Scandale. Experimental study of the radiation emitted by 180 gev/c electrons and positrons volume-reflected in a bent crystal. *Phys. Rev. A*, 79:012903, Jan 2009. doi: 10.1103/PhysRevA.79.012903.

[79] A.M. Taratin. Particle channeling in bent crystal. *Physics of Particles and Nuclei*, 29(5): 437 – 462, 1998.

[80] Yu. M. Ivanov *et al.* Volume reflection of a proton beam in a bent crystal. *Phys. Rev. Lett.*, 97:144801, Oct 2006.

[81] Scandale et al. High-efficiency volume reflection of an ultrarelativistic proton beam with a bent silicon crystal. *Phys. Rev. Lett.*, 98:154801, 2007. doi: 10.1103/PhysRevLett.98.154801.

[82] W. Scandale *et al.* Observation of channeling and volume reflection in bent crystals for high-energy negative particles. *Phys. Lett. B*, 681(3):233 – 236, 2009.

[83] W. Scandale *et al.* Volume reflection dependence of 400 gev/c protons on the bent crystal curvature. *Phys. Rev. Lett.*, 101:234801, Dec 2008.

[84] W. Scandale *et al.* Observation of multiple volume reflection of ultrarelativistic protons by a sequence of several bent silicon crystals. *Phys. Rev. Lett.*, 102:084801, 2009.

[85] V.A. Andreev *et al. Pis'ma v Zh. Eksp. Teor. Fiz.*, 36:340, 1982.

[86] Yu.A. Chesnokov, N.A. Galyaev, V.I. Kotov, S.V. Tsarik, and V.N. Zapolsky. 70 gev proton volume capture into channeling mode with a bent si single crystal. *Nuclear Instruments and Methods in Physics Research Section B: Beam Interactions with Materials and Atoms*, 69:247 – 252, 1992.

[87] L. H. Thomas. The motion of a spinning electron. *Nature*, 117:514, 1926. doi: 10.1038/117514a0.

[88] L. H. Thomas. The kinematics of an electron with an axis. *Phil. Mag.*, 3:1–21, 1927.

[89] V. Bargmann, Louis Michel, and V. L. Telegdi. Precession of the polarization of particles moving in a homogeneous electromagnetic field. *Phys. Rev. Lett.*, 2:435–436, May 1959. doi: 10.1103/PhysRevLett.2.435.

[90] C. Patrignani. *Chin. Phys.*, C40(10):100001, 2016.

[91] Filippo Sala. A bound on the charm chromo-EDM and its implications. *JHEP*, 03:061, 2014. doi: 10.1007/JHEP03(2014)061.

[92] Shu-Min Zhao, Tai-Fu Feng, Zhong-Jun Yang, Hai-Bin Zhang, Xing-Xing Dong, and Tao Guo. The one loop contributions to c(t) electric dipole moment in the CP violating BLMSSM. *Eur. Phys. J.*, C77(2):102, 2017. doi: 10.1140/epjc/s10052-017-4627-x.

[93] A. G. Grozin, I. B. Khriplovich, and A. S. Rudenko. Upper limits on electric dipole moments of tau-lepton, heavy quarks, and W-boson. *Nucl. Phys.*, B821:285–290, 2009. doi: 10.1016/j.nuclphysb.2009.06.026.

[94] R. Escribano and E. Masso. Constraints on fermion magnetic and electric moments from LEP-1. *Nucl. Phys.*, B429:19–32, 1994. doi: 10.1016/S0550-3213(94)80039-1.

[95] A. E. Blinov and A. S. Rudenko. Upper Limits on Electric and Weak Dipole Moments of tau-Lepton and Heavy Quarks from e+ e- Annihilation. *Nucl. Phys. Proc. Suppl.*, 189: 257–259, 2009. doi: 10.1016/j.nuclphysbps.2009.03.043.

[96] A. Cordero-Cid, J. M. Hernandez, G. Tavares-Velasco, and J. J. Toscano. Bounding the top and bottom electric dipole moments from neutron experimental data. *J. Phys.*, G35: 025004, 2008. doi: 10.1088/0954-3899/35/2/025004.

[97] Ick Joh Kim. Magnetic moment measurement of baryons with heavy flavored quarks by planar channeling through bent crystal. *Nucl. Phys.*, B229:251–268, 1983. doi: 10.1016/0550-3213(83)90363-2.

[98] V. V. Baublis et al. Measuring the magnetic moments of short-lived particles using channeling in bent crystals. *Nucl. Instrum. Meth.*, B90:112–118, 1994. doi: 10.1016/0168-583X(94)95524-7.

[99] V. M. Samsonov. On the possibility of measuring charm baryon magnetic moments with channeling. *Nucl. Instrum. Meth.*, B119:271–279, 1996. doi: 10.1016/0168-583X(96)00348-5.

[100] V. G. Baryshevsky. The possibility to measure the magnetic moments of short-lived particles (charm and beauty baryons) at LHC and FCC energies using the phenomenon of spin rotation in crystals. *Phys. Lett.*, B757:426–429, 2016. doi: 10.1016/j.physletb.2016.04.025.

[101] L Burmistrov, G Calderini, Yu Ivanov, L Massacrier, P Robbe, W Scandale, and A Stocchi. Measurement of Short Living Baryon Magnetic Moment using Bent Crystals at SPS and LHC. Technical Report CERN-SPSC-2016-030. SPSC-EOI-012, CERN, Geneva, Jun 2016.

[102] A. S. Fomin, A. Yu. Korchin, A. Stocchi, O. A. Bezshyyko, L. Burmistrov, S. P. Fomin, I. V. Kirillin, L. Massacrier, A. Natochii, P. Robbe, W. Scandale, and N. F. Shul'ga. Feasibility of measuring the magnetic dipole moments of the charm baryons at the lhc using bent

crystals. *Journal of High Energy Physics*, 2017(8):120, Aug 2017. ISSN 1029-8479. doi: 10.1007/JHEP08(2017)120. URL `https://doi.org/10.1007/JHEP08(2017)120`.

[103] Botella, F. J., Garcia Martin, L. M., Marangotto, D., Martinez Vidal, F., Merli, A., Neri, N., Oyanguren, A., and Ruiz Vidal, J. On the search for the electric dipole moment of strange and charm baryons at LHC. *Eur. Phys. J. C*, 77(3):181, 2017. doi: 10.1140/epjc/s10052-017-4679-y.

[104] V. L. Lyuboshits. The Spin Rotation at Deflection of Relativistic Charged Particle in Electric Field. *Sov. J. Nucl. Phys.*, 31:509, 1980.

[105] J. D. Jackson. *Classical Electrodynamics*. Wiley & Sons, 1975.

[106] L. D. Landau and E. M. Lifshitz. *The Classical Theory of Fields. Vol. 2 (4th ed.)*. Butterworth-Heinemann, 1975.

[107] A.I. Akhiezer and N.F. Shulga. *High-energy electrodynamics in matter*. Gordon & Breach, New York, 1996.

[108] Lev Davidovich Landau and II Pomeranchuk. The limits of applicability of the theory of bremsstrahlung by electrons and of the creation of pairs at large energies. In *Dokl. Akad. Nauk SSSR*, volume 92, page 535, 1953.

[109] UI Uggerhøj. *Ultrarelativistic particles in matter*. PhD thesis, Doctoral Dissertation. Department of Physics and Astronomy, University of Aarhus, Denmark, http://www. phys. au. dk/˜ ulrik/Doct_dis_UIU. pdf, 2011.

[110] VN Baier and VM Katkov. Quantum effects in magnetic bremsstrahlung. *Physics Letters A*, 25(7):492–493, 1967.

[111] VN Baier and VM Katkov. Processes involved in the motion of high energy particles in a magnetic field. *Sov. Phys. JETP*, 26:854, 1968.

[112] V. Tikhomirov L. Bandiera, V. Haurylavets. Compact electromagnetic calorimeters based on oriented scintillator crystals. *Nucl. Instr. Meth. A*, 936, 2019. doi: 10.1016/j.nima.2018.07.085.

[113] D. Mirarchi et. al. Special losses. *Proc. of the 9th Evian Workshop*, February 2019.

[114] V.V. Tikhomirov and A.I. Sytov. The miscut angle influence on the future LHC crystal based collimation system. *Prob.Atomic Sci.Technol.*, 57:88–92, 2012.

[115] Daniele Mirarchi. *Vol. 31 - Crystal Collimation for LHC. Crystal collimation for LHC*. PhD thesis, Aug 2015. URL `http://cds.cern.ch/record/2036210`. Presented 18 Jun 2015.

[116] G. Germogli. *Fabrication and characterization of silicon bent crystals for channeling experiments*. Phd thesis, University of Ferrara, 2016.

[117] I. Stensgaard, L.C. Feldman, and P.J. Silverman. Calculation of the backscattering-channeling surface peak. *Surface Science*, 77(3):513 – 522, 1978. ISSN 0039-6028. doi: https://doi.org/10.1016/0039-6028(78)90137-1.

[118] Robert L. Kauffman, L. C. Feldman, P. J. Silverman, and R. A. Zuhr. Significance of the channeling surface peak in thin-film analysis. *Applied Physics Letters*, 32(2):93–94, 1978. doi: 10.1063/1.89948.

[119] E. N. Tsyganov. Estimates of cooling and bending processes for charged particle penetration through a mono crystal. Technical report, Fermilab, 1976. Preprint TM-684.

[120] M. D. Bavijev, Yu. A. Tchesnokov, R. A. Rzaev, A. R. Dzyba, E. I. Rozum, and S. A. Vorobeev. Bent crystal application to formation and diagnostics of proton beam. *Radiation Effects*, 107(2-4):157–165, 1989. doi: 10.1080/00337578908228560.

[121] X. Altuna *et al.* High efficiency multi-pass proton beam extraction with a bent crystal at the sps. *Phys. Lett. B*, 357(4):671 – 677, 1995. ISSN 0370-2693. doi: 10.1016/0370-2693(95)00981-P. URL `http://www.sciencedirect.com/science/article/pii/037026939500981P`.

[122] A.G Afonin et al. High-efficiency multipass extraction of 70-gev protons from an accelerator with a short bent crystal. *Physics Letters B*, 435(1):240 – 244, 1998. doi: https://doi.org/10.1016/S0370-2693(98)00940-X.

[123] O.I. Sumbaev. Experimental investigation of the elastic quasi-mosaic effect. *Soviet Phys. JETP*, 27:1042–1044, 1957.

[124] A.G. Afonin et al. The schemes of proton extraction from ihep accelerator using bent crystals. *Nuclear Instruments and Methods in Physics Research Section B: Beam Interactions with Materials and Atoms*, 234(1):14 – 22, 2005. doi: https://doi.org/10.1016/j.nimb.2004.12.128.

[125] D. G. Bellow, G. Ford, and J. S. Kennedy. Anticlastic behavior of flat plates. *Experimental Mechanics*, 5(4):227–232, Jul 1965. ISSN 1741-2765. doi: 10.1007/BF02321057. URL `https://doi.org/10.1007/BF02321057`.

[126] Vincenzo Guidi, L Lanzoni, and Andrea Mazzolari. Study of anticlastic deformation in a silicon crystal for channeling experiments. *Journal of Applied Physics*, 107(11):113534, 2010. doi: 10.1063/1.3372722.

[127] Camattari R. et al. Anicryde: calculation of elastic properties in silicon and germanium crystals. *Journal of Applied Crystallography*, 48(3):943–949, Jun 2015. doi: 10.1107/S1600576715005087.

[128] S. Baricordi, V. Guidi, A. Mazzolari, D. Vincenzi, and M. Ferroni. Shaping of silicon crystals for channelling experiments through anisotropic chemical etching. *J. Phys. D: Appl. Phys.*, 41(24):245501, 2008.

[129] B. Schwartz and H. Robbins. Chemical etching of silicon iv. etching technology. *J. Electrochem. Soc*, 123(12):1903–1909, 1976. doi: 10.1149/1.2132721.

[130] Roberto Rossi, Gianluca Cavoto, Daniele Mirarchi, Stefano Redaelli, and Walter Scandale. Measurements of coherent interactions of 400gev protons in silicon bent crystals. *Nuclear Instruments and Methods in Physics Research Section B: Beam Interactions with Materials and Atoms*, 355:369 – 373, 2015. doi: 10.1016/j.nimb.2015.03.001.

[131] W et al. Scandale. Study of inelastic nuclear interactions of 400 gev/c protons in bent silicon crystals for beam steering purposes. *The European Physical Journal C*, 78(6):505, Jun 2018. doi: 10.1140/epjc/s10052-018-5985-8.

[132] Roberto Rossi. *Experimental Assessment of Crystal Collimation at the Large Hadron Collider*. PhD thesis, Oct 2017. URL `http://cds.cern.ch/record/2644175`. Presented 26 Jan 2018.

[133] Valeriia Zhovkovska. Characterisation of the bent silicon crystals and study of the inelastic nuclear interactions of 180 gev/c pions in bent crystals at the ua9 experiment . ch - channeling. Sep 2018. URL `http://cds.cern.ch/record/2639682`.

[134] M Pesaresi et al. Design and performance of a high rate, high angular resolution beam telescope used for crystal channeling studies. *Journal of Instrumentation*, 6(04):P04006–P04006, apr 2011. doi: 10.1088/1748-0221/6/04/p04006.

[135] D. De Salvador et al. Innovative remotely-controlled bending device for thin silicon and germanium crystals. *Journal of Instrumentation*, 13(04):C04006–C04006, apr 2018. doi: 10.1088/1748-0221/13/04/c04006.

[136] Vincent Baglin. The lhc vacuum system: Commissioning up to nominal luminosity. *Vacuum*, 138:112 – 119, 2017. doi: 10.1016/j.vacuum.2016.12.046.

[137] A R Machado and J Wallbank. Machining of titanium and its alloys—a review. *Proceedings of the Institution of Mechanical Engineers, Part B: Journal of Engineering Manufacture*, 204(1):53–60, 1990. doi: 10.1243/PIME_PROC_1990_204_047_02.

[138] M. Manjaiah et al. A review on machining of titanium based alloys using edm and wedm. *Rev. Adv. Mater. Sci.*, 36:89–111, 2014.

[139] W. Scandale. Experimental insertions for the LHC. Technical Report CERN-1990-010-V-3, CERN, Geneva, 1990.

[140] Yu. Ivanov, A. Petrunin, and V. Skorobogatov. Observation of the elastic quasi-mosaicity effect in bent silicon single crystals. *JETP Letters*, 81:99–101, 2005.

[141] R. Camattari, V. Guidi, V. Bellucci, and A. Mazzolari. The 'quasi-mosaic' effect in crystals and its applications in modern physics. *J. Appl. Cryst.*, 48:977–989, 2015. doi: 10.1107/S1600576715009875.

[142] V.I. Kushnir, J.P. Quintana, and P. Georgopoulos. On the sagittal focusing of synchrotron radiation with a double crystal monochromator. *Nucl. Instr. Meth. Phys. Res. A*, 328(3): 588 – 591, 1993. ISSN 0168-9002. doi: https://doi.org/10.1016/0168-9002(93)90679-C.

[143] S.K. Kaldor and I.C. Noyan. Flexural loading of rectangular si beams and plates. *Mater. Sci. Eng. A*, 399(1):64 – 71, 2005. ISSN 0921-5093. doi: https://doi.org/10.1016/j.msea.2005.02.065.

[144] Y. Gogotsi, C. Baek, and F. Kirscht. Raman microspectroscopy study of processing-induced phase transformations and residual stress in silicon. *Semicond. Sci. Technol.*, 14:936–944, 1999. doi: 10.1088/0268-1242/14/10/310.

[145] R. Camattari, V. Guidi, L. Lanzoni, and I. Neri. Experimental analysis and modeling of self-standing curved crystals for focusing of x-rays. *Meccanica*, 48:1875–1882, 2013. ISSN 0025-6455. doi: 10.1007/s11012-013-9734-7.

[146] E. Bagli and V. Guidi. Simulation of orientational effects in crystals with structural defects. *Nucl. Instr. Meth. Phys. Res. B*, 355:365–368, 2015. doi: 10.1016/j.nimb.2015.03.072.

[147] A. Mazzolari, M. Romagnoni, R. Camattari, E. Bagli, L. Bandiera, G. Germogli, V. Guidi, and G. Cavoto. Bent crystals for efficient beam steering of multi tev-particle beams. *The European Physical Journal C*, 78(9):720, Sep 2018. ISSN 1434-6052. doi: 10.1140/epjc/s10052-018-6196-z.

[148] S. Agostinelli *et al.* Geant4 simulation toolkit. *Nuclear Instruments and Methods in Physics Research Section A: Accelerators, Spectrometers, Detectors and Associated Equipment*, 506 (3):250 – 303, 2003. doi: http://dx.doi.org/10.1016/S0168-9002(03)01368-8.

[149] J. Allison et al. Recent developments in Geant4. *Nucl. Instr. Meth. Phys. Res. A*, 835: 186–225, 2016. ISSN 0168-9002. doi: 10.1016/j.nima.2016.06.125.

[150] E. Bagli, M. Asai, D. Brandt, A. Dotti, V. Guidi, and D. H. Wright. A model for the interaction of high-energy particles in straight and bent crystals implemented in geant4. *Eur. Phys. J. C*, 74(8):2996, 2014. doi: 10.1140/epjc/s10052-014-2996-y. URL `http://dx.doi.org/10.1140/epjc/s10052-014-2996-y`.

[151] E. Bagli and V. Guidi. Dynecharm++: a toolkit to simulate coherent interactions of high-energy charged particles in complex structures. *Nuclear Instruments and Methods in Physics Research Section B: Beam Interactions with Materials and Atoms*, 309:124 – 129, 2013.

[152] E. Bagli, V. Guidi, and V. A. Maisheev. Calculation of the potential for interaction of particles with complex atomic structures. *Phys. Rev. E*, 81, Feb 2010. doi: 10.1103/PhysRevE.81.026708.

[153] E. Bagli et al. Coherent effects of high-energy particles in a graded $si_{1-x}ge_x$ crystal. *Phys. Rev. Lett.*, 110:175502, 2013. doi: 10.1103/PhysRevLett.110.175502.

[154] E. Bagli, M. Asai, A. Dotti, L. Pandola, and M. Verderi. Allowing for crystalline structure effects in Geant4. *Nucl. Instr. Meth. Phys. Res. B*, 402:304 – 307, 2017. ISSN 0168-583X. doi: https://doi.org/10.1016/j.nimb.2017.03.092.

[155] E. Bagli, L. Bandiera, V. Bellucci, A. Berra, R. Camattari, D. De Salvador, G. Germogli, V. Guidi, L. Lanzoni, D. Lietti, A. Mazzolari, M. Prest, V.V. Tikhomirov, and E. Vallazza. Experimental evidence of planar channeling in a periodically bent crystal. *Eur. Phys. J. C*, 74(10):3114–1–3114–7, 2014. ISSN 1434-6044. doi: 10.1140/epjc/s10052-014-3114-x.

[156] Riccardo Camattari, Gianfranco Paternò, Marco Romagnoni, Valerio Bellucci, Andrea Mazzolari, and Vincenzo Guidi. Homogeneous self-standing curved monocrystals, obtained using sandblasting, to be used as manipulators of hard X-rays and charged particle beams. *Journal of Applied Crystallography*, 50(1):145–151, Feb 2017. doi: 10.1107/S1600576716018768.

[157] A.N. Danilewsky, A. Rack, J. Wittge, T. Weitkamp, R. Simon, H. Riesemeier, and T. Baumbach. White beam synchrotron topography using a high resolution digital x-ray imaging detector. *Nucl. Instrum. Methods Phys. Res. B*, 266(9):2035 – 2040, 2008. doi: 10.1016/j.nimb.2008.02.065.

[158] R. Camattari, G. Paternò, M. Romagnoni, V. Bellucci, A. Mazzolari, and V. Guidi. Homogeneous self-standing curved monocrystals, obtained through sandblasting, to be used as manipulators of hard x-ray and charged particle beams. *J. Appl. Cryst.*, 50:145–151, 2017. doi: 10.1107/S1600576716018768.

[159] Cécile Malgrange. X-ray propagation in distorted crystals: From dynamical to kinematical theory. *Cryst. Res. and Tech.*, 37:654–662, 2002.

[160] A. Authier. *Dynamical theory of X-ray diffraction*. Oxford University Press, 2001.

[161] T. Tuomi, K. Naukkarinen, and P. Rabe. Use of synchrotron radiation in x-ray diffraction topography. *Phys. Status Solidi A*, 25(1):93–106, 1974. doi: 10.1002/pssa.2210250106.

[162] A. N. Danilewsky, J. Wittge, A. Hess, A. Cröll, A. Rack, D. Allen, P. McNally, T. dos Santos Rolo, P. Vagovič, T. Baumbach, J. Garagorri, M. R. Elizalde, and B. K. Tanner. Real-time x-ray diffraction imaging for semiconductor wafer metrology and high temperature in situ experiments. *Phys. Status Solidi A*, 208(11):2499–2504, 2011. doi: 10.1002/pssa.201184264.

[163] Alexander Rack, Mario Scheel, and Andreas N. Danilewsky. Real-time direct and diffraction X-ray imaging of irregular silicon wafer breakage. *IUCrJ*, 3(2):108–114, 2016. doi: 10.1107/S205225251502271X.

[164] B.K. Tanner, J. Wittge, P. Vagovič, T. Baumbach, D. Allen, P.J. McNally, R. Bytheway, D. Jacques, M.C. Fossati, D.K. Bowen, et al. X-ray diffraction imaging for predictive metrology of crack propagation in 450-mm diameter silicon wafers. *Powder Diffr.*, 28(2): 95–99, 2013. doi: 10.1017/S0885715613000122.

[165] V.V. Kvardakov, K.M. Podurets, S.A. Schetinkin, J. Baruchel, J. Härtwig, and M. Schlenker. Study of the three-dimensional distribution of defects in crystals by synchrotron radiation diffraction tomography. *Nucl. Instrum. Methods Phys. Res. A*, 575(1): 140 – 143, 2007. doi: 10.1016/j.nima.2007.01.044.

[166] D. Allen, J. Wittge, A. Zlotos, E. Gorostegui-Colinas, J. Garagorri, P.J. McNally, A.N. Danilewsky, and M.R. Elizalde. Observation of nano-indent induced strain fields and dislocation generation in silicon wafers using micro-raman spectroscopy and white beam x-ray topography. *Nucl. Instrum. Methods Phys. Res. B*, 268(3):383 – 387, 2010. doi: 10.1016/j.nimb.2009.10.174.

[167] D. Hänschke, A. Danilewsky, E. Helfen, L. andHamann, and T. Baumbach. Correlated three-dimensional imaging of dislocations: Insights into the onset of thermal slip in semiconductor wafers. *Phys. Rev. Lett.*, 119:215504, 2017. doi: 10.1103/PhysRevLett.119.215504.

[168] T. E. Chupp, P. Fierlinger, M. J. Ramsey-Musolf, and J. T. Singh. Electric dipole moments of atoms, molecules, nuclei, and particles. *Rev. Mod. Phys.*, 91:015001, Jan 2019. doi: 10.1103/RevModPhys.91.015001.

[169] Georg Schneider, Andreas Mooser, Matthew Bohman, Natalie Schön, James Harrington, Takashi Higuchi, Hiroki Nagahama, Stefan Sellner, Christian Smorra, Klaus Blaum, Yasuyuki Matsuda, Wolfgang Quint, Jochen Walz, and Stefan Ulmer. Double-trap measurement of the proton magnetic moment at 0.3 parts per billion precision. *Science*, 358(6366): 1081–1084, 2017. ISSN 0036-8075. doi: 10.1126/science.aan0207.

[170] B. K. Sahoo. Improved limits on the hadronic and semihadronic *cp* violating parameters and role of a dark force carrier in the electric dipole moment of ^{199}Hg. *Phys. Rev. D*, 95: 013002, Jan 2017. doi: 10.1103/PhysRevD.95.013002.

[171] J. M. et al. Pendlebury. Revised experimental upper limit on the electric dipole moment of the neutron. *Phys. Rev. D*, 92:092003, Nov 2015. doi: 10.1103/PhysRevD.92.092003.

[172] G. et al. Bennett. Final report of the e821 muon anomalous magnetic moment measurement at bnl. *Phys. Rev. D*, 73:072003, Apr 2006. doi: 10.1103/PhysRevD.73.072003.

[173] G. W. et al. Bennett. Improved limit on the muon electric dipole moment. *Phys. Rev. D*, 80:052008, Sep 2009. doi: 10.1103/PhysRevD.80.052008.

[174] D. Hanneke, S. Fogwell, and G. Gabrielse. New measurement of the electron magnetic moment and the fine structure constant. *Phys. Rev. Lett.*, 100:120801, Mar 2008. doi: 10.1103/PhysRevLett.100.120801.

[175] J. et al. Baron. Order of magnitude smaller limit on the electric dipole moment of the electron. *Science*, 343(6168):269–272, 2014. ISSN 0036-8075. doi: 10.1126/science.1248213.

[176] N. Neri. Mdm/edm experiments with bent crystals at lhc. CERN, Physics Beyond Collider, January 2019.

[177] E. Bagli, V. Guidi, A. Mazzolari, L. Bandiera, G. Germogli, A. I. Sytov, D. De Salvador, A. Argiolas, M. Bazzan, A. Carnera, A. Berra, D. Bolognini, D. Lietti, M. Prest, and E. Vallazza. Orientational coherent effects of high-energy particles in a linbo$_3$ crystal. *Phys. Rev. Lett.*, 115:015503, 2015. doi: 10.1103/PhysRevLett.115.015503.

[178] E. Sirtl and A. Adler. Chromic-hydrofluoric acid as a specific system for the development of etch pits on silicon. *Zeitschrift für metallkunde*, 52:529–534, 1961.

[179] F.S.d. Aragona. Dislocation etch for (100) planes in silicon. *J. Electrochem. Soc.*, 119: 948–951, 1972.

[180] A.I. Sytov and V.V. Tikhomirov. CRYSTAL simulation code and modeling of coherent effects in a bent crystal at the LHC. *Nucl. Instrum. Methods Phys. Res. B*, 355:383 – 386, 2015. doi: 10.1016/j.nimb.2015.02.042.

[181] A. I. Sytov, V. V. Tikhomirov, and L. Bandiera. Simulation code for modeling of coherent effects of radiation generation in oriented crystals. *Phys. Rev. Accel. Beams*, 22:064601, 2019. doi: 10.1103/PhysRevAccelBeams.22.064601.

[182] S. Chatrchyan et al. The cms experiment at the cern lhc. *Journal of Instrumentation*, 3 (08):S08004, 2008. doi: 10.1088/1748-0221/3/08/S08004.

[183] WB Atwood, Aous A Abdo, M Ackermann, W Althouse, B Anderson, M Axelsson, L Baldini, J Ballet, DL Band, Guido Barbiellini, et al. The large area telescope on the fermi gamma-ray space telescope mission. *The Astrophysical Journal*, 697(2):1071, 2009.

[184] V.G. Baryshevskii and V.V. Tikhomirov. Synchrotron-type radiation processes in crystals and polarization phenomena accompanying them. *Sov. Phys. Usp.*, 32:1013–1032, 1989. doi: 10.1070/pu1989v032n11abeh002778.

[185] M. Aaboud et al. Evidence for light-by-light scattering in heavy-ion collisions with the atlas detector at the lhc. *Nature Phys*, 13:852–858, 2017. doi: 10.1038/nphys4208.

[186] J. C. Kimball and N. Cue. Quantum electrodynamics and channeling in crystals. *Phys. Rep.*, 125:69–101, 1985.

[187] A. H. Sørensen and E. Uggerhøj. Channelling and channelling radiation. *Nature*, 325: 311–415, 1987.

[188] A. Belkacem et al. Measurement of the total energy radiated by 150-gev electrons in a ge crystal. *Phys. Rev. Lett.*, 54:2667–2670, 1985. doi: 10.1103/PhysRevLett.54.2667.

[189] A. Belkacem et al. New channeling effects in the radiative emission of 150 gev electrons in a thin germanium crystal. *Phys. Lett. B*, 177:211–216, 1986. doi: 10.1016/0370-2693(86)91059-2.

[190] R. Medenwaldt et al. Detailed investigations of shower formation in ge- and w-crystals traversed by 40–287 gev/c electrons. *Phys. Lett. B*, 227:483–488, 1989. doi: 10.1016/0370-2693(89)90967-2.

[191] VA Baskov, VA Khablo, VV Kim, VI Sergienko, BI Luchkov, and V Yu Tugaenko. Electromagnetic showers in aligned crystals. *Nuclear Instruments and Methods in Physics Research Section B: Beam Interactions with Materials and Atoms*, 122(2):194–198, 1997.

[192] A. Baurichter et al. Enhanced electromagnetic showers initiated by 20–180 gev gamma rays on aligned thick germanium crystals. *Nucl. Instrum. Methods Phys. Res. Sect. B*, 152: 472–478, 1999. doi: 10.1016/S0168-583X(99)00226-8.

[193] V.A. Baskov et al. Electromagnetic cascades in oriented crystals of garnet and tungstate. *Phys. Lett. B*, 456:86–89, 1999. doi: 10.1016/S0370-2693(99)00444-X.

[194] L. Bandiera, V. V. Tikhomirov, M. Romagnoni, N. Argiolas, E. Bagli, G. Ballerini, A. Berra, C. Brizzolari, R. Camattari, D. De Salvador, V. Haurylavets, V. Mascagna, A. Mazzolari, M. Prest, M. Soldani, A. Sytov, and E. Vallazza. Strong reduction of the effective radiation length in an axially oriented scintillator crystal. *Phys. Rev. Lett.*, 121, Jul 2018. doi: 10.1103/PhysRevLett.121.021603.

[195] Borrmann G. and Hartwig W. Die absorption der röntgenstrahlen im dreistrahlfall der interferenz. *Zeitschrift für Kristallographie - Crystalline Materials*, 121:401–409, 1965. doi: 10.1524/zkri.1965.121.16.401.

[196] L. Bandiera et al. Broad and intense radiation accompanying multiple volume reflection of ultrarelativistic electrons in a bent crystal. *Phys. Rev. Lett.*, 111:255502, 2013. doi: 10.1103/PhysRevLett.111.255502.

[197] D. Lietti et al. Radiation emission phenomena in bent silicon crystals: Theoretical and experimental studies with 120 gev/c positrons. *Nucl. Instrum. Methods Phys. Res., Sect. B*, 283:84 – 92, 2012.

[198] L. Bandiera et al. On the radiation accompanying volume reflection. *Nucl. Instr. Meth. B*, 309:135 – 140, 2013.

[199] V. Guidi, L. Bandiera and V. Tikhomirov. Radiation generated by single and multiple volume reflection of ultrarelativistic electrons and positrons in bent crystals. *Phys. Rev. A*, 86:042903, 2012.

[200] L. Bandiera et al. Investigation of the electromagnetic radiation emitted by sub-gev electrons in a bent crystal. *Phys. Rev. Lett.*, 115:025504, 2015.

[201] X. Artru. A simulation code for channeling radiation by ultrarelativistic electrons or positrons. *Nucl. Instr. Meth. B*, 48:278 – 282, 1990. doi: 10.1016/0168-583X(90)90122-B.

[202] V.G. Baryshevsky et al. On the influence of crystal structure on the electromagnetic shower development in the lead tungstate crystals. *Nucl. Instr. and Meth. in Phys. Res. Sect. B*, 402:35–39, 2017. doi: 10.1016/j.nimb.2017.02.066.

[203] R. Moore et al. Measurement of pair-production by high energy photons in an aligned tungsten crystal. *Nucl. Instr. and Meth. in Phys. Res. Sect. B*, 119:149–155, 1996.

[204] M. Ter-Mikaelian. The interference emission of high-energy electrons. *Zh. Eksp. Teor. Fiz.*, 25:296, 1953.

[205] M. Moulson. Prospects for an experiment to measure $BR(K_L^0 \to \pi^0 \nu \bar{\nu})$ at the cern sps. *Journal of Physics: Conference Series*, 800:012037, 2017. doi: 10.1088/1742-6596/800/1/012037.

[206] E. Nardi et al. Resonant production of dark photons in positron beam dump experiments. *arXiv*, 2018. URL `https://arxiv.org/pdf/1802.04756`.

[207] K. Elsener et al. Ultrashort electromagnetic showers in single crystals: Applications in high-energy γ-ray astronomy ? *Cosmic Gamma Rays, Neutrinos, and Related Astrophysics. NATO ASI Series (Series C: Mathematical and Physical Sciences)*, 270, 1989. doi: 10.1007/978-94-009-0921-$2_3$1.

[208] E. Depero et al. High purity 100 gev electron identification with synchrotron radiation. *Nucl. Instr. and Meth. in Phys. Res. Sect. A*, 866:196–201, 2017. doi: 10.1016/j.nima.2017.05.028.

Acknowledgments

I thank my Tutor Professor Vincenzo Guidi, the University of Ferrara and INFN for the opportunity to achieve this doctorate. I thank Dr. Mazzolari, Dr. Bandiera and Dr. Camattari for their support during my research work, as well as all the colleagues I worked with and published together.

Ringrazio la mia famiglia per essermi sempre stata accanto, e Eleonora che ha sempre creduto in me.